

GEOMETRICAL EFFECT ON SINGLE-SITE
RUTHENIUM AND TUNGSTEN OXIDE CATALYSTS

PRATYA PROMCHANA



A THESIS SUBMITTED IN PARTIAL FULFILLMENT OF THE REQUIREMENT FOR
THE DEGREE OF DOCTOR OF PHILOSOPHY IN APPLIED CHEMISTRY
DEPARTMENT OF CHEMISTRY SCHOOL OF SCIENCE
KING MONGKUT'S INSTITUTE OF TECHNOLOGY LADKRABANG

2023

KMITL-2023-SC-D-012-011

This material is reserved for educational use only, not allowed for commercial use.

Forbidden to modify the content, and cite the document when use.



COPYRIGHT 2023

SCHOOL OF SCIENCE

KING MONGKUT'S INSTITUTE OF TECHNOLOGY LADKRABANG

This material is reserved for educational use only, not allowed for commercial use.

Forbidden to modify the content, and cite the document when use.

Thesis Title Geometrical effect on single-site Ruthenium and tungsten oxide catalysts
Student Name Pratyā Promchana
Student ID 59605005
Degree Department Doctor of Philosophy (Applied Chemistry)
Year 2023
Thesis Advisor Prof. Dr. Tawan Sooknoi
Thesis Co-advisor Assoc. Prof. Dr. Kittisak Choojun

Abstract

Geometrical effect on single-site ruthenium catalysts, 1,6-Hexanediol (1,6-HD) oxidation to ϵ -caprolactone (ϵ -CL) was investigated using (*p*-cymene)RuCl₂(L) complexes with phosphine (L_{P1-P5}) and pyridine (L_{N1-N5}) ligands as catalysts. Despite similar Ru electron density, the activity of (*p*-cymene)RuCl₂(L_P) increases with the decrease in phosphine steric hindrance rather than the electronic properties. The reaction rate correlates with the pocket-size dimension (θ_c), defined by the (centroid of the *p*-cymene ring)-Ru-(centroid of 2Cl) angle of the (*p*-cymene)RuCl₂(L) complexes. This observation supports an associative interchange mechanism previously proposed by computational studies. The readily accessible θ_c ($\geq 145^\circ$) of these L_N complexes results in a similar rate, regardless of different L_N ligands. For both complexes, the ϵ -CL selectivity depends only on 1,6-HD conversion. Even though bases significantly enhance the activity, they readily affect the complex stability. The methyl isobutyl carbinol (MIBC) produced during the reaction could competitively react with the Ru catalysts, leading to catalyst deactivation, especially when MIBC : 1,6-HD ≥ 2 times. For the geometrical effect on single-site tungsten oxide catalysts, acetylene in ethylene-rich feed can be removed *via* acetylene/ethylene cross-metathesis over WO₃-supported catalysts at 450 °C, yielding 1,3-butadiene with cyclohexene as a minor product. The catalyst must be treated with ethylene at 600 °C to generate a genuinely active site of tungsten (IV) alkylidene species (W=CH₂). The H₂ treatment decreases surface W=O concentration, and hence the activity. Raman spectroscopy shows that active single-site WO₃ species, including mono oxo-WO₃ ((O=)W(O-Si)₃ and (O=)W(O-Si)₄) and dioxo-WO₃ species (O=)₂W(O-Si)₂ were generated in 2%WO₃/SiO₂, while the WO₃ cluster and bulk WO₃ exist in 3-5%WO₃/SiO₂ and 7%WO₃/SiO₂, respectively. The

This material is reserved for educational use only, not allowed for commercial use.

5%WO₃/NaX and 5%WO₃/NaY provide lower activity due to coke formation over the acid sites. With high surface area and confined surface silanol of 5%WO₃/MCM-41% and 5%WO₃/SBA-15, *in situ* TR-EXAFS evidences the formation of only O=W(O-Si)₃. This species provides an isolated W=CH₂ site with relatively higher activity and is less prone to coke formation than the WO₃ cluster in 5%WO₃/SiO₂.

Keywords: ε-Caprolactone, ruthenium complex, 1,6-hexanediol, oxidation, Cross-metathesis, Acetylene removal, Ethylene, Tungsten oxide



This material is reserved for educational use only, not allowed for commercial use.

Forbidden to modify the content, and cite the document when use.

Acknowledgements

I would take this opportunity to acknowledge advisors Prof. Dr. Tawan Sooknoi and Co-Advisor Assoc. Prof. Dr. Kittisak Choojun, for the continually suggestions, graceful knowledge, and useful discussions throughout this work. In addition, we would like to sincere appreciate chairperson and committee members, Prof. Dr. Joongjai Panpranot, Assoc. Prof. Dr. Khamphree Phomphrai, Assoc. Prof. Dr. Karoon Sadorn and Asst. Prof. Dr. Chaval Sriwong, for the opinions and the guidance with a graceful.

I would like to thank Asst. Prof. Dr. Nararak Leesakul, and Asst. Prof. Dr. Saowanit Saithong, from Division of Physical Science and Center of Excellence for Innovation in Chemistry, Faculty of Science, Prince of Songkla University, and Assoc. Prof. Dr. Kittipong Chainok, from Materials and Textile Technology, Faculty of Science and Technology, Thammasat University for the new (*p*-cymene)RuCl(L_{p4}) complex, the crystal structure and X-ray refinement.

I am very grateful to Dr. Yingyot Poo-arporn and Dr. Wanwisa Limphirat, Beamline 2.2, and Dr. Wantana Klysubun, Beamline 8, Synchrotron Light Research Institute, Nakhon Ratchasima for the XAS analysis and suggestions.

We would like to distribute a thank to Catalytic Chemistry Research Unit members for their contribution of the ideas and facilities and most importantly their supports.

Furthermore, we would like to express our appreciation thanks to Department of Chemistry, Faculty of Science, King Mongkut's Institute of Technology Ladkrabang for advanced laboratory instruments, equipment, chemicals, and accommodation.

Last but not least, I would like to gracefully thank the parents and families for encouragement throughout this work.

Pratya Promchana

Table of contents

	Page
Abstract.....	I
Acknowledgements.....	III
Table of contents.....	IV
List of tables.....	VIII
List of figures.....	IX
List of schemes.....	XIV
Abbreviations/symbols.....	XV
Chapter 1 Introduction.....	1
1.1 Research motivation.....	1
1.2 Objectives of the study.....	3
1.3 Scopes of the study.....	3
1.4 Benefits of the study.....	5
Chapter 2 Theory and literature reviews.....	6
2.1 The oxidation of 1,6-hexanediol to ϵ -caprolactone.....	6
2.1.1 1,6-Hexanediol.....	6
2.1.2 ϵ -Caprolactone.....	6
2.1.3 Adipic acid.....	7
2.1.4 Oxidation.....	7
2.1.4.1 Oxidation's mechanism.....	8
2.1.4.2 The catalysts for the oxidation of alcohol.....	9
2.1.5 The geometrical effect of Ru complexes on.....	9
the oxidation of 1,6-hexanediol to ϵ -caprolactone	
2.1.6 Literature reviews.....	11
2.2 Acetylene/ethylene metathesis.....	15
2.2.1 Ethylene.....	15
2.2.2 Acetylene.....	15
2.2.3 1,3-Butadiene.....	16
2.2.4 Cyclohexene.....	17
2.2.5 Metathesis.....	17

This material is reserved for educational use only, not allowed for commercial use.

Forbidden to modify the content, and cite the document when use.

Table of contents (continued)

	Page
2.2.5.1 Olefin metathesis.....	18
2.2.5.2 Olefin metathesis' thermodynamics.....	19
2.2.5.3 Olefin metathesis mechanism.....	20
2.2.5.4 Heterogeneous catalysts for the olefin metathesis.....	20
2.2.5.5 Diel-Alder reaction.....	21
2.2.6 The geometrical effect of WO ₃ species on.....	22
acetylene/ethylene metathesis	
2.2.7 Literature reviews.....	24
Chapter 3 Research methodology.....	26
3.1 Reagents.....	26
3.2 Apparatuses.....	27
3.3 Experimental procedures.....	28
3.3.1 The oxidation of 1,6-hexanediol using Ru complex as catalysts	28
3.3.1.1 Synthesis of (<i>p</i> -cymene)RuCl ₂ (L).....	28
3.3.2 Acetylene/ethylene metathesis using WO ₃ - supported catalysts	29
3.3.2.1 SBA-15 synthesis.....	29
3.3.2.2 MCM-41 synthesis.....	30
3.3.2.3 WO ₃ catalysts preparation.....	30
3.3.3 Characterizations.....	30
3.3.3.1 NMR.....	30
3.3.3.2 Matrix-assisted laser desorption ionization-time.....	30
of flight mass spectrometer (MALDI-TOF MS) and fast liquid chromatography quadrupole Time-of-Flight (QTOF) Mass Spectrometry (LC-QTOF)	
3.3.3.3 X-ray crystallographic refinement.....	31
3.3.3.4 CHN analysis.....	31
3.3.3.5 UV-VIS spectroscopy.....	31

This material is reserved for educational use only, not allowed for commercial use.

Forbidden to modify the content, and cite the document when use.

Table of contents (continued)

	Page
Author biography.....	110



This material is reserved for educational use only, not allowed for commercial use.

Forbidden to modify the content, and cite the document when use.

List of tables

Table	Page
3.1 A series of the ligands L_P and L_N	28
4.1 L_P and L_N ligands for the (<i>p</i> -cymene) $RuCl_2(L)$ complexes.....	36
4.2 Pocket-site dimension (θ_c , °) of (<i>p</i> -cymene) $RuCl_2(L)$	38
4.3 Conversion and product distribution using (<i>p</i> -cymene) $RuCl_2(L)$ complexes as catalysts	41
4.4 Ru L_3 -edge energy and Cl K-edge energy of (<i>p</i> -cymene) $RuCl_2(L)$ complexes	42
4.5 Activity of (<i>p</i> -cymene) $RuCl_2(L_{P4})$ for 1,6-HD oxidation..... in various conditions ^a .	47
4.6 Physical and Chemical properties of WO_3/SiO_2 catalysts.....	52
4.7 Fitting parameters for the first coordination shell of 5% WO_3/SiO_2 ,..... reduced 5% WO_3/SiO_2 , 5% $WO_3/MCM-41$ and 5% $WO_3/SBA-15$ W L_3 -edge <i>in situ</i> TR-EXAFS spectra at 500 °C under air-zero	60
4.8 Acetylene removal via acetylene/ethylene cross-metathesis..... over WO_3 over silica support	62
4.9 Physical and chemical properties of WO_3 over confined supports.....	64
4.10 Acetylene/ethylene cross-metathesis over WO_3 supported..... on various confined supports	65
4.11 W L_3 -edge energy and average W oxidation state of all samples..... at 500 °C under air-zero and after 1-hexene treatment at 600 °C for 5 min	67
A1 Crystallographic detail of (<i>p</i> -cymene) $RuCl_2(L_{N3})$	91
A2 Selected bond distances (Å) and bond angles (°) for the Ru complexes.....	92
A3 6-Hydroxyhexan-1-al and ϵ -caprolactone selectivity at..... the similar conversion extrapolated from the reaction profile using (<i>p</i> -cymene) $RuCl_2(L)$ catalysts	98
B1 Energy gap derived from UV-VIS DRS spectra.....	102
B2 W L_3 -edge energy and average W oxidation state of all samples..... at 500°C under air-zero 30 mL·min ⁻¹	103

This material is reserved for educational use only, not allowed for commercial use.

Forbidden to modify the content, and cite the document when use.

List of figures

Figure	Page
2.1 Reaction sequences for autoxidation.....	8
2.2 Multistep electron transfer process for the oxidation of alcohol.....	9
2.3 Molybdenum (VI)- and tungsten (VI)-based centers coordinated.....	18
Alkoxide and imido ligands	
2.4 Hoveyda–Grubbs catalysts.....	19
2.5 Olefins metathesis' mechanism.....	20
2.6 A molecular structure of a) di-oxo, b) mono-oxo, and c) polymeric WO ₃	21
2.7 HOMO-LUMO of Diels-Alder reaction.....	22
3.1 Schematic diagram for the oxidation of 1,6-hexanediol.....	34
3.2 Schematic diagram for acetylene/ethylene metathesis.....	35
4.1 1,6-HD oxidation time profile using the (<i>p</i> -cymene)RuCl ₂ (L _{P4}) catalyst.....	39
a) with K ₂ CO ₃ and b) without base (conversion (●), 6-hydroxyhexan-1-al (■), 1,6-hexanedial (◆), ε-CL (▲), and adipic acid (x) (0.025 mmol Ru complex, 1 mmol 1,6-HD, under N ₂ atmosphere, 110 °C, 30 mL toluene, 0.2 mmol K ₂ CO ₃ , 8 mmol MIBK)	
4.2 Pseudo 1 st order kinetics of 1,6-HD oxidation using.....	40
a) (<i>p</i> -cymene)RuCl ₂ (L _P) and b) (<i>p</i> -cymene)RuCl ₂ (L _N) catalysts (0.025 mmol Ru complex, 1 mmol 1,6-HD, under N ₂ atmosphere, 110 °C, 30 mL toluene, 0.2 mmol base, 8 mmol MIBK)	
4.3 XANES spectra of Ru L ₃ -edge and Cl K-edge energies of a) and.....	43
a') (<i>p</i> -cymene RuCl ₂ (L _P) and b) and b') (<i>p</i> -cymene)RuCl ₂ (L _N) in toluene.	
4.4 Relation between <i>k</i> _{app} and the pocket size dimension of.....	44
(<i>p</i> -cymene)RuCl ₂ (L) complexes	
4.5 The relation between product selectivity and conversion.....	45
(0.025 mmol (<i>p</i> -cymene)RuCl ₂ (L _{P4}), 1 mmol 1,6-HD, under N ₂ atmosphere, 110 °C, 30 mL toluene, 0.2 mmol K ₂ CO ₃ , 8 mmol MIBK)	
4.6 Apesguia's plot of 1,6-HD oxidation using different amounts.....	46
of (<i>p</i> -cymene)RuCl ₂ (L _{P4}) catalyst (1 mmol 1,6-HD, under N ₂ atmosphere, 110 °C, 30 mL toluene, 0.2 mmol K ₂ CO ₃ , 8 mmol MIBK)	

This material is reserved for educational use only, not allowed for commercial use.

Forbidden to modify the content, and cite the document when use.

List of figures (continued)

Figure	Page
<p>4.7 1,6-HD oxidation time profiles using the (<i>p</i>-cymene)Ru(L_{P4})Cl₂ catalyst.....48 with a) 0.5 mmol 1,6-HD spiking at 60 min and b) 0.5 mmol 1,6-HD spiking at 30 min (conversion (●), 6-hydroxyhexan-1-al (■), 1,6-hexanedial (◆), ε-CL (▲), and adipic acid (×) (0.025 mmol Ru complex, 1 mmol 1,6-HD, under N₂ atmosphere, 110 °C, 30 mL toluene, 0.2 mmol K₂CO₃, 8 mmol MIBK)).</p>	48
<p>4.8 500 MHz ¹³C-CPMAS NMR spectra of MIBC and.....49 [Ru(OMIBC)₄]_∞ complex</p>	49
<p>4.9 500 MHz ¹H NMR spectra of (<i>p</i>-cymene)RuCl₂(L_{P4}) after.....50 The addition of 34 mmol MIBC at 110 °C for 5 min in toluene-d⁸; a) 0–10 ppm and b) zoom 0–4 ppm</p>	50
<p>4.10 (A) XRD diffraction patterns, (B) UV-VIS DRS spectra,.....53 (C) Raman spectra, and (D) Fourier transform of W L₃-edge <i>in situ</i> EXAFS spectra at 500°C under air-zero of WO₃ over silica support</p>	53
<p>4.11 Raman spectra of various WO₃/silica supports.....55</p>	55
<p>4.12 Effect of ethylene treatment on acetylene removal over.....56 5%WO₃/SiO₂ (A) at 450 °C when catalyst was (a) untreated, (b) treated at 450 °C for 2 h and (c) treated at 600 °C for 2 h, and B) at 200–600 °C (feed flow rate 15 (for A) or 20 mL·min⁻¹ (for B), acetylene/ethylene = 1/99 wt.%, N₂ flow rate 35 mL·min⁻¹)</p>	56
<p>4.13 Acetylene/ethylene cross-metathesis over non-reduced and.....58 reduced 5%WO₃/SiO₂ with/without ethylene treatment (feed flow rate 15 mL·min⁻¹ (acetylene/ethylene = 1/99 wt.%), N₂ flow rate 35 mL·min⁻¹, 450 °C)</p>	58
<p>4.14 (A) H₂-TPR of WO₃ supported SiO₂ and (A) and Fourier transform.....59 of W L₃-edge <i>in situ</i> TR-EXAFS spectra of calcined and reduced under H₂ at 500 °C for 30 min of 5%WO₃/SiO₂</p>	59

List of figures (continued)

Figure	Page
4.15 Effect of A) WO ₃ loading and B) W/F plot of acetylene/ethylene cross-metathesis over 2%WO ₃ /SiO ₂ ; (●) conversion, (▲) 1,3-butadiene, (■) cyclohexene, (feed flow rate 20 mL·min ⁻¹ (acetylene/ethylene = 1/99 wt.%), N ₂ flow rate 35 mL·min ⁻¹ , 450 °C, activation in ethylene at 600 °C for 2 h)	61
4.16 Raman spectra of WO ₃ over siliceous support in the range of A) 200-900 cm ⁻¹ and B) 900-1100 cm ⁻¹	64
4.17 Fourier transform of W L ₃ -edge <i>in situ</i> TR-EXAFS spectra with 1-hexene activation over A) 5%WO ₃ /MCM-41, B) 5%WO ₃ /SBA-15, and C) 5%WO ₃ /SiO ₂	68
4.18 A) a ratio of 1 st shell intensity and B) a ratio of 2 nd shell intensity under 1-hexene activation to calcined catalysts (I _r /I ₀)	69
A1 ¹ H 500 MHz NMR spectrum of (<i>p</i> -cymene)RuCl ₂ (L _{N3}) in chloroform-d ₁	90
A2 ¹³ C 500 MHz NMR spectrum of (<i>p</i> -cymene)RuCl ₂ (L _{N3}) in chloroform-d ₁	90
A3 ORTEP representation (50% probability ellipsoid) of complex (<i>p</i> -cymene)RuCl ₂ (L _{N3}) (minor disorder part of the methyl group at C6 are omitted for clarity)	91
A4 ¹ H 500 MHz NMR spectrum of (<i>p</i> -cymene)RuCl ₂ (L _{P1}) in chloroform-d ₁	93
A5 ¹ H 500 MHz NMR spectrum of (<i>p</i> -cymene)RuCl ₂ (L _{P2}) in chloroform-d ₁	93
A6 ¹ H 500 MHz NMR spectrum of (<i>p</i> -cymene)RuCl ₂ (L _{P4}) in chloroform-d ₁	94
A7 ¹ H 500 MHz NMR spectrum of (<i>p</i> -cymene)RuCl ₂ (L _{N1}) in chloroform-d ₁	94
A8 ¹ H 500 MHz NMR spectrum of (<i>p</i> -cymene)RuCl ₂ (L _{N2}) in chloroform-d ₁	95
A9 ¹ H 500 MHz NMR spectrum of (<i>p</i> -cymene)RuCl ₂ (L _{N4}) in chloroform-d ₁	95
A10 ¹ H 500 MHz NMR spectrum of (<i>p</i> -cymene)RuCl ₂ (L _{N5}) in chloroform-d ₁	96

List of figures (continued)

Figure	Page
A11 1,6-HD oxidation time profile using (<i>p</i> -cymene)RuCl ₂ L catalysts where.....97 a) L _{P1} , b) L _{P2} , c) L _{P3} , d) L _{P5} , e) L _{N1} , f) L _{N2} g) L _{N3} , h) L _{N4} , i) L _{N5} and j) [(<i>p</i> -cymene)RuCl ₂] ₂ catalyst (conversion (●), 6-hydroxyhexa-1-nal (■), 1,6-hexanedial (◇), ε-CL (▲), and adipic acid (×) (0.025 mmol Ru complex, 1 mmol 1,6-HD, under N ₂ atmosphere, 110 °C, 30 mL toluene, 0.2 mmol K ₂ CO ₃ , 8 mmol MIBK)	97
A12 UV-VIS spectra of (<i>p</i> -cymene)RuCl ₂ (L _{P4}) a) before (–) and.....99 after (–) heated at 110 °C in the presence of K ₂ CO ₃ in toluene	99
A13 1,6-HD oxidation time profile using (<i>p</i> -cymene)RuCl ₂ (L _{P4}) catalyst.....99 with a) the addition of equimolar ε-CL, b) KOH and c) <i>t</i> -BuOK (conversion (●), 6-hydroxyhexa-1-nal (■), 1,6-hexanedial (◇), ε-CL (▲), and adipic acid (×) (0.025 mmol Ru complex, 1 mmol 1,6-HD, under N ₂ atmosphere, 110 °C, 30 mL toluene, 0.2 mmol K ₂ CO ₃ , 8 mmol MIBK)	99
A14 Kinetics plot of 1,6-HD oxidation using (<i>p</i> -cymene)RuCl ₂ (L _{P4}) catalyst.....100 with the addition of equimolar ε-CL (◇), K ₂ CO ₃ (●), KOH (▲), and <i>t</i> -BuOK (■) (0.025 mmol Ru complex, 1 mmol 1,6-HD, under N ₂ atmosphere, 110 °C, 30 mL toluene, 0.2 mmol base, 8 mmol MIBK)	100
A15 TGA curve under air-zero (a) and mass spectra.....100 (b) attained by QTOF mass spectrometry electrospray analysis of Ru(MIBC) ₄	100
A16 500 MHz ¹ H NMR spectra of the reaction of (<i>p</i> -cymene)RuCl ₂ (L _{P4}).....101 with 34 mmol MIBC at 110 °C for 5 min in toluene-d ₈ after left overnight; a) 0-10 ppm and b) zoom 0-4 ppm	101
B1 A) normalized and B) 2 nd derivative W L ₃ -edge <i>in situ</i> TR-XANES spectra.....102 of all catalysts and W standard at 500°C under air-zero (^a Estimated at room temperature and ^b under H ₂ gas)	102
B2 Average oxidation state determination from W L ₃ -edge energy.....103 of W standard	103
B3 W L ₃ -edge <i>in situ</i> TR-EXAFS Fitting of a, a') 5%WO ₃ /SiO ₂104 and b, b') reduced 5%WO ₃ /SiO ₂ at 500°C	104

This material is reserved for educational use only, not allowed for commercial use.

Forbidden to modify the content, and cite the document when use.

List of figures (continued)

Figure	Page
B4 UV-VIS DRS spectra (A) and H ₂ -TPR profile (B) of WO ₃ over confined silica support	104
B5 NH ₃ -TPD of WO ₃ supported on various supports	105
B6 TGA curve of ethylene treated 5%WO ₃ /NaY, and 5%WO ₃ /NaX under air-zero (30 mL.min ⁻¹)	105
B7 Acetylene removal with time on stream over a) 5%WO ₃ /SiO ₂ , b) 5%WO ₃ /MCM-41 and c) 5%WO ₃ /SBA-15 (Feed flow rate 20 mL.min ⁻¹ (acetylene/ethylene = 1/99 wt.%), N ₂ flow rate 35 mL.min ⁻¹ , 450°C, activation in ethylene at 600°C for 2 h)	106
B8 XRD diffraction patterns of WO ₃ over confined supports a) wide angle and b) low angle	106
B9 W L ₃ -edge <i>in-situ</i> TR-EXAFS Fitting of a, a') 5%WO ₃ /MCM-41 and b, b') 5%WO ₃ /SBA-15 at 500°C	107
B10 The 2 nd derivative of W L ₃ -edge <i>in situ</i> TR-XANES spectra of a) 5%WO ₃ /SiO ₂ , b) 5%WO ₃ /MCM-41, and c) 5%WO ₃ /SBA-15 with 1-hexene activation at 600°C	107
B11 TGA curve of ethylene treated 5%WO ₃ /SiO ₂ , 5%WO ₃ /MCM-41 and 5%WO ₃ /SBA-15 under air-zero (30 mL.min ⁻¹)	108

List of schemes

Scheme	Page
2.1 The structure of 1,6-hexanediol.....	6
2.2 The structure of ϵ -caprolactone.....	6
2.3 The structure of adipic acid.....	7
2.4 The oxidative series with the degree of the oxidation.....	8
2.5 The structure of a) 1,3-butadiene and b) 1,2-butadiene.....	16
2.6 A representation of olefins metathesis.....	18
2.7 1-Butene/propylene cross-metathesis.....	19
2.8 Cycloheptene/ethylene ring-opening metathesis.....	19
3.1 A short representation of Ru-complexes.....	28
4.1 Structure of the (<i>p</i> -cymene)RuCl ₂ (L) complexes.....	37
4.2 Possible pathway for the 1,6-HD oxidation over (<i>p</i> -cymene)RuCl ₂ (L).....	44
4.3 W ⁴⁺ alkylidene formation over 5%WO ₃ /SiO ₂ during ethylene treatment..... and proposed mechanism of acetylene/ethylene cross metathesis.	57
4.4 Reduction of WO ₃ over 5%WO ₃ /SiO ₂	60
4.5 Acetylene/ethylene cross-metathesis and Diels-Alder reaction.....	61

Abbreviations/Symbols

°C	Degree Celsius
Cp	Cyclopentadienyl ligand
Cp*	Pentamethyl cyclopentadienyl ligand
4-OMe	4-Methylalkoxy group
4-CF ₃	4-Trifluorocarbon group
NHC	N-heterocyclic carbene
M-C(O)OH	Metallocarboxylic acid
PYA	Pyridylideneamide
dmobpy	4,4'-Dimethoxy-2,2'-bipyridine
<i>i</i> -PrOH	<i>iso</i> -Propyl alcohol
Ru-H	Hydrido Ru complex
RuH ₂	Ru dihydride
^t BuOOH	<i>tert</i> -Butyl hydroperoxide
DPPF	1,1'-Bis(diphenylphosphino)ferrocene
LDPE	Low-density polyethylene
HDPE	High-density polyethylene
^t BuOK	Potassium <i>tert</i> -butoxide
TOF	Turnover frequency
1,6-HD	1,6-Hexanediol
ε-CL	ε-Caprolactone
L	Ligand
L _{P1}	Tricyclohexyl phosphine
L _{P2}	Triphenylphosphine oxide
L _{P3}	(2-Ethoxyethyl) (diphenyl) phosphine oxide
L _{P4}	Triphenylphosphine
L _{P5}	Bis(diphenyl)phosphinomethane
L _{N1}	Pyridine
L _{N2}	4-Methylpyridine
L _{N3}	4- <i>tert</i> -Butylpyridine
L _{N4}	2,4-Dichloropyridine

This material is reserved for educational use only, not allowed for commercial use.

Forbidden to modify the content, and cite the document when use.

Abbreviations/Symbols (Continued)

L_{N5}	4-Dimethylaminopyridine
θ_c	Pocket-size dimension
k_{app}	Apparent rate constant
I_a	Associative interchange mechanism
MIBK	Methyl isobutyl ketone
MIBC	Methyl isobutyl carbinol or 2-oxyphenol
NMR	Nuclear Magnetic Resonance Spectroscopy
MALDI-TOF MS	Matrix-Assisted Laser Desorption Ionization-Time of Flight Mass Spectrometer
LC-QTOF	Fast Liquid Chromatography Quadrupole Time-Of-Flight
TR-XAS	Time-Resolved X-ray Absorption Spectroscopy
TR-XANES	Time-Resolved X-ray Absorption Near Edge Spectroscopy
TR-EXAFS	Time-Resolved Extended X-ray Absorption Fine Structure
XRD	X-Ray Diffraction Analysis
WD-XRF	Wavelength Dispersive X-ray Fluorescence Spectrophotometer
TPR	Temperature-Programmed Reduction technique
NH_3 -TPD	NH_3 -Temperature Programmed Desorption technique
DRS-UV	Differential Reflectance Spectroscopy
FT-Raman	Fourier Transforms Raman Spectroscopy
TGA	Thermogravimetric Analysis

CHAPTER 1

INTRODUCTION

1.1 Research Motivation

Enzymes is a biological catalyst, evolving in an environment for millions of years [1-5]. Most of enzymes are assembled *in vivo* from a metal and a three-dimensional protein network to generate the specific active site [6-9]. The variation of metal oxidation states and protein structures can lead to a various electronic and geometrical properties to offer the chemo-, regio-, and enantioselectivity for chemical reactions in cells [10-16]. In similar manner for catalysis, both electronic and geometrical properties of metal complex or metal active site directly affect the activity of both homogeneous and heterogenous catalysts [17-21]. Especially, the geometrical structure of the catalyst would modulate the feed adsorption kinetics, the site selective that leads to the specific regioselectivity [22-25]. Furthermore, the geometrical structure influences the electronic properties of the catalysts., especially the single-site metal complexes. Though, the geometrical structure of metal single-site complex in homogeneous and heterogenous catalysts would be manipulated with different parameters.

For the heterogeneous catalysis having metal complex as a catalyst, the geometrical structure of metal complex can be operated by using the different types and/or steric hindrance of ligands. In particular for the oxidation-cyclization of diols (1,4-buatiol, 1,6-hexandiol, etc..) to form lactone via “Oppenauer process,” the geometrical structure of Ru complexes deriving from the ligands has a vast effect. For tetrahedral RuL_4 catalysts, where L = monodentate phosphine, the complex has a large degree of freedom for alcohols and ketones to interact. This leads to the lower chance for the reaction and lower rate of cyclization. While the half-sandwich Ru complexes had been shown to improve both the activity and cyclization products. Since the half-sandwich Ru complexes offer only the bottom halve for the reactants to interact/coordinate, the degree of freedom of the complex would be lower leading to the higher chance of diols to interact with ketones and also increase the cyclization rate. Buntara *et al.* reported that the use of $[(p\text{-cymene})RuCl_2]_2$ and bis(diphenylphosphino) ferrocene (DPPF) could enhance 1,6-hexanediol oxidation to

This material is reserved for educational use only, not allowed for commercial use.

Forbidden to modify the content, and cite the document when use.

ϵ -caprolactone in acetone [26]. Similarly, Ito *et al.* examined the oxidation of 1,4-butanediol using $\text{Cp}^*\text{RuCl}[\text{Ph}_2\text{P}(\text{CH}_2)_2\text{NH}_2\text{-}\kappa^2\text{-P, N}]$ (cod) complexes in the presence of $^t\text{BuOK}$ [27]. It was suggested that chemo- and enantioselectivity for the Oppenauer oxidation could be governed by adding phosphine and amine ligands. Nevertheless, the effect of types and steric hindrance of ligands towards the geometrical structure of half-sandwich Ru complexes has not been studied. Furthermore, the electronic properties deriving from the different ligands has not yet been elucidated as well.

In sharp contrast, the geometrical structure of supported metal oxide catalysts mainly derived from the number of oxo ligands and the silanol anchoring site from the supports. This would lead to the dispersion and the formation of the different geometrical structures of the single-site metal oxide catalysts. For examples, a supported WO_3 catalyst could present in various species, including $(\text{SiO})_4\text{W=O}$, $(\text{SiO})_3\text{W=O}$, $(\text{SiO})_2\text{W(=O)}_2$, polymeric and bulk WO_3 species and providing the different activity. Schalkwyk *et al.* reported that 8% WO_3/SiO_2 (bulk WO_3) gave a low activity for 1-octene metathesis and 7-tetradecene selectivity, compared to 2% WO_3/SiO_2 (monomeric WO_3) [35]. On the other hand, bulk WO_3 seems favorable for isomerization and coke formation. In addition to the number of the oxo ligands, the interaction between WO_3 and the support also influences the activity. Furthermore, the amount of silanol of the support could have the direct influences on the generation of single-site WO_3 species in term of both amount and types. Even though, the most active form of WO_3 for metathesis is the single-site WO_3 , no one has ever evaluated the different activity of this different single-site WO_3 species.

In this thesis, the geometrical effect of single-site Ruthenium and Tungsten catalysts on the catalytic activity would be demonstrated. For the single-site Ru catalysts, half-sandwich (*p*-cymene) $\text{RuCl}_2(\text{L})$ complexes where L = N-donor (L_N) and P-donor (L_P) ligands were selected as a representative for a heterogeneous reaction using oxidation-cyclization of 1,6-hexadiol to ϵ -caprolactone via Oppenauer reaction. The effect of geometrical structures deriving from the different steric hindrance of L_N and L_P on i) the Ru electronic properties, ii) the reaction rate and iii) product selectivity was studied. In the heterogeneous catalysis, supported single-site WO_3 on various supports (SiO_2 , MCM-41, SBA-15, NaY, and NaX) was prepared and determined the catalytic performance for acetylene/ethylene metathesis as a model reaction. The effect of the WO_3 loadings and silanols from supports on the formation of WO_3 species

This material is reserved for educational use only, not allowed for commercial use.

was determined. The geometrical structure of the prepared WO_3 catalysts was also studied by examined by Extended X-ray absorption fine structure (EXAFS). The relationship between the geometrical structure of supported single-site WO_3 catalysts and activity was demonstrated.

1.2 Objectives of the study

1.2.1 To understand the electronic and geometrical effect of the active site on the oxidation of 1,6-hexanediol and acetylene/ethylene metathesis.

1.2.2 To synthesize a single crystal of new (*p*-cymene) $\text{RuCl}_2(\text{L}_{\text{N}3})$ complex.

1.2.3 To understand the promotional effect of the hydrogen donor and added bases on the oxidation of 1,6-hexanediol.

1.2.4 To understand the formation of W^{4+} alkylidene species upon ethylene and 1-hexene treatment.

1.2.5 To understand the effect of WO_3 reduction on the acetylene/ethylene metathesis.

1.2.5 To understand the effect of surface silanol (Si-OH), Al-OH, and the confinement of the WO_3 species on the supports for acetylene/ethylene metathesis.

1.2.6 To understand the cause of the deactivation of Ru complexes and WO_3 supported catalysts.

1.3 Scopes of the study

1.3.1 The oxidation of 1,6-hexanediol using Ru complex as catalysts.

1.3.1.1 The oxidation of 1,6-hexanediol was examined in a homogeneous phase using (*p*-cymene) $\text{RuCl}_2(\text{L})$ where L (L_{P} and L_{N}) = tricyclohexyl phosphine ($\text{L}_{\text{P}1}$), triphenylphosphine oxide ($\text{L}_{\text{P}2}$), (2-ethoxyethyl) (diphenyl) phosphine oxide ($\text{L}_{\text{P}3}$), triphenylphosphine ($\text{L}_{\text{P}4}$), bis(diphenyl)phosphinomethane ($\text{L}_{\text{P}5}$), pyridine ($\text{L}_{\text{N}1}$), 4-methylpyridine ($\text{L}_{\text{N}2}$), 4-*tert*-butylpyridine ($\text{L}_{\text{N}3}$), 2,4-dichloropyridine ($\text{L}_{\text{N}4}$), 4-dimethylaminopyridine ($\text{L}_{\text{N}5}$), respectively.

1.3.1.2 The formation of a new (*p*-cymene) $\text{RuCl}_2(4\text{-tert-butylpyridine} (\text{L}_{\text{N}3}))$ complex was verified by X-ray crystallographic refinement, solid-state carbon Nuclear Magnetic Resonance Spectroscopy (solid-state $^{13}\text{C-NMR}$), CHN analysis, and matrix-assisted laser desorption ionization-time of flight mass spectrometer (MALDI-TOF MS).

This material is reserved for educational use only, not allowed for commercial use.

Forbidden to modify the content, and cite the document when use.

1.3.1.3 The electronic effect of the Ru complexes on 1,6-hexanediol oxidation was examined by liquid phase X-ray Absorption Near Edge Spectroscopy (XANES) using toluene/MIBK (30:1 by volume) as a solvent.

1.3.1.4 The structural information of the Ru complexes was determined by X-ray crystallographic structure and Proton/Carbon Nuclear Magnetic Resonance Spectroscopy (^1H and ^{13}C -NMR).

1.3.1.5 The oxidation of 1,6-hexanediol was investigated at 110 °C under an inert atmosphere (N_2) using toluene as solvent and methyl iso-butyl ketone (MIBK) as a hydrogen acceptor.

1.3.1.6 The effect of the added base on 1,6-hexanediol oxidation was investigated by K_2CO_3 , $^t\text{BuOK}$, and KOH .

1.3.1.7 The deactivation of the Ru complexes was estimated by Apesguia estimation, UV-VIS spectroscopy, and 1,6-hexanediol or methyl iso-butyl carbinol (1,6-HD or MIBC) spiking technique.

1.3.2 Acetylene/ethylene metathesis over WO_3 supported catalysts.

1.3.2.1 WO_3 supported catalysts were prepared by wet impregnation method from ammonium metatungstate precursor.

1.3.2.2 Davisil SiO_2 , Zeolite NaY, Zeolite NaX, MCM-41, and SBA-15 were used as support.

1.3.2.3 The WO_3 dispersion and the interaction between WO_3 and the surface silanol were determined by X-ray diffraction analysis (XRD) and temperature-programmed reduction technique (TPR).

1.3.2.4 Acid properties of the catalysts were determined by the NH_3 -Temperature Programmed Desorption technique (NH_3 -TPD)

1.3.2.5 Acetylene/ethylene metathesis was performed in a fixed-bed reactor at 200-600 °C by 1%mol acetylene in ethylene at a feed rate of 5-20 $\text{mL}\cdot\text{min}^{-1}$ balanced with inert gas (N_2) to obtain a total flow rate of 55 $\text{mL}\cdot\text{min}^{-1}$, and contact time 80-800 $\text{g}\cdot\text{h}\cdot\text{mol}^{-1}$.

1.3.2.6 The electronic effect of the WO_3 species over the siliceous supports was investigated by *in situ* W L_3 -edge Time-resolved X-ray Absorption Near Edge Spectroscopy (TR-XANES).

1.3.2.7 The structural information of WO_3 species was investigated by Differential reflectance spectroscopy (DRS-UV), Fourier transform Raman spectroscopy (FT-Raman), and *in situ* W L_3 -edge Time-resolved Extended X-ray absorption fine structure (*in situ* W L_3 -edge TR-EXAFS).

1.3.2.8 The formation of W^{4+} alkylidene species was examined by ethylene treatment and 1-hexene treatment at 600 °C for 2 h using W L_3 -edge Time-resolved X-ray Absorption Spectroscopy (TR-XAS).

1.3.2.9 The deactivation of the catalysts upon the ethylene and 1-hexene treatment was investigated by Thermogravimetric Analysis (TGA) and *in situ* W L_3 -edge Time-resolved Extended X-ray absorption fine structure with 1-hexene treatment (*in situ* W L_3 -edge TR-EXAFS), respectively.

1.4 Benefits of the study

The study of an active site's electronic and geometrical effect on the catalytic activity of the oxidation of 1,6-hexanediol using Ru-complex as catalysts and acetylene/ethylene metathesis using WO_3 -supported catalysts will be shed light on other important chemical reactions. Moreover, it can pave the way for obtaining catalysts with higher efficiency.

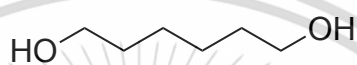
CHAPTER 2

THEORY AND LITERATURE REVIEWS

2.1 The oxidation of 1,6-hexadiol to ϵ -caprolactone

2.1.1 1,6-Hexanediol [28, 29]

1,6-Hexanediol is a double hydroxyl group-containing organic compound with the chemical formula of $(\text{CH}_2\text{CH}_2\text{CH}_2\text{OH})_2$ (Scheme 2.1).

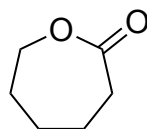


Scheme 2.1 The structure of 1,6-hexanediol

It is derived from bio-based feedstock in the form of a colorless solid which is insoluble in water. Commonly, it was industrially produced from the hydrogenation of adipic acid and its ester. Moreover, it could be prepared in the laboratory by reducing adipic acid using lithium aluminum hydride (LiAlH_4) as a reducing agent. However, the preparation in the laboratory is not available because it is costly and uneconomical. It can be used as an additive to improve the hardness and flexibility of polyesters as building up from a long hydrocarbon molecule. It can also be used as a polyurethane chain extender for the high hydrolysis resistance, high mechanical properties, and low glass transition temperature. It can be used as an intermediate to produce acrylics, adhesives, dyestuffs, unsaturated polyester resins, styrene, maleic anhydride, and fumaric acid.

2.1.2 ϵ -Caprolactone [30-33]

ϵ -Caprolactone is a cyclic ester-containing seven-membered ring (Scheme 2.2) forming a colorless liquid that is miscible in most organic solvents and water. It was named after the starting chemical caproic acid.



Scheme 2.2 The structure of ϵ -caprolactone

This material is reserved for educational use only, not allowed for commercial use.

Forbidden to modify the content, and cite the document when use.

Caprolactone is frequently produced by Baeyer-Villiger oxidation of cyclohexanone in peracetic acid. It was manufactured on a large scale for a biochemical feedstock of caprolactam. Moreover, it can be applied in the polymer industry, such as a facile monomer for the plastic with unique properties. Ring-opening polymerization of caprolactone would yield polycaprolactone in the bioplastic, medical, and surgery sectors.

2.1.3 Adipic acid [33-35]

Adipic acid, namely hexanedioic acid in IUPAC nomenclature, is an organic compound containing a di-carboxylic group with the formula of $(\text{CH}_2)_4(\text{COOH})_2$ (Scheme 2.3).

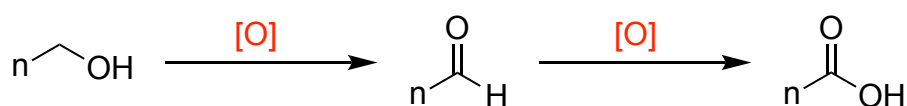


Scheme 2.3 The structure of adipic acid

It is produced more than 2.5 billion kilograms yearly for worldwide industries, for example, as a precursor for producing nylon-6 and E number food additive E355. However, it rarely occurs *in vivo*. Instead, it can be taken from the cyclohexanone and cyclohexanol mixture (KA oil) oxidation via multistep reactions. Cyclohexanol can be converted to ketone, its derivative, and nitrous acid. Nitrous oxide is equivalently produced in 1/1 of adipic acid through nitrolic acid intermediate. Additionally, this reaction can also yield glutaric and succinic acids as by-products. In a retrosynthesis, adipic acid was first obtained from fats' oxidation. Accordingly, its name is from the Latin word *adeps*, *adipis*, - "animal fat" or adipose tissue.

2.1.4 Oxidation [36]

Oxidation is the reaction relating to losing electrons or adding oxygen to a molecule, atom, or ion. It occurs as the molecule's charge increases; the opposite is called reduction. As the oxidation takes place, the oxidative series of the molecule is progressed (Scheme 2.4).



Scheme 2.4 The oxidative series with the degree of the oxidation

It was first pioneered in the study of combustion and fat oxidation by Lavoisier. Catalytic oxidation is the oxidation with the catalyst resulting in an enhanced reaction rate, e.g., decreased activation energy. It is indicated that the reaction required a lower temperature than that of the thermal oxidation (320-540 °C). Conventional oxidation commonly uses transition metals with an oxidizing agent such as H₂O₂, NaOI₄, peracetic acid, or atmospheric O₂ (aerobic oxidation). The oxidation of an alcohol to a carbonyl compound has been the center of many organic syntheses. As the oxidizing agent is utilized, the selection for the oxidizing agent is crucial. It must not severely react to an active site or over oxidize the reactant. The reaction via a radical mechanism was not easily controllable; an undesirable competitive reaction from the radical mechanism may lead to lower productivity. Some of the oxidation takes place without the oxidizing agent called dehydrogenative oxidation. The catalyst would change to hydride intermediate, which can be recovered by the reaction with amine or olefinic compound. In some cases, the hydrogen evolution would be observed, especially for the acceptorless dehydrogenative oxidation.

2.1.4.1 oxidation's mechanism [37]

The oxidation with the oxidizing agent or autoxidation involves the free radical chain mechanism (one-electron process), where the reactant is developed by the initiation, propagation, and termination process, as shown in **Figure 2.1**.

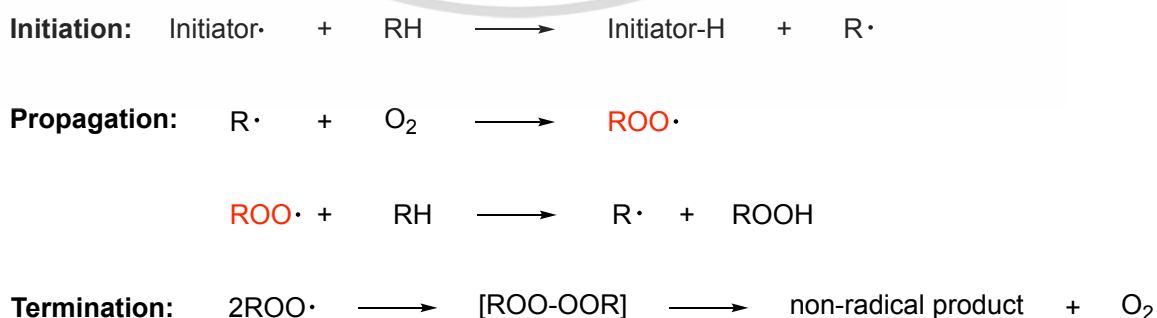


Figure 2.1 Reaction sequences for autoxidation

This material is reserved for educational use only, not allowed for commercial use.

Forbidden to modify the content, and cite the document when use.

The reactant would undergo homolytic cleavage by a thermal or photolytic event yielding a radical initiator (R·). It reacts with the oxygen molecule to peroxy radical compound (ROO·), a compound that abstracts a proton from the reactant, producing alkyl peroxide (ROOH). The reaction rate notably depends on the probability of C-H bond breaking (C-H bond strength). Later, the propagation is shut down by a reaction between two peroxy radicals forming a non-radical product and molecular oxygen.

Non-radical or hydrogen transfer process has been applied for the oxidation of alcohol using Ru-based catalysts. It was first developed after Liu *et al.* [38] examined aerobic oxidation with a hydrogen acceptor via a multistep electron-transfer process, as shown in Figure 2.2.

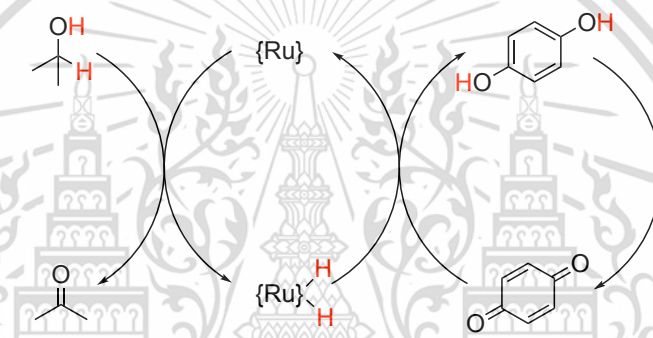


Figure 2.2 Multistep electron transfer process for the oxidation of alcohol

2.1.4.2 The catalysts for the oxidation of alcohol [39]

Transition metal-based catalysts such as Pd, Ru, Fe, Cu, Pt, Au, Ir, and Rh with the oxidizing agent or molecular O_2 were commonly used in the oxidation. In the last decades, metal with the ligand was exploited to achieve regio- and enantioselective reactions. The ligands play an important role in electronic and structural modification. For example, pyridine-containing palladium complexes can activate the reaction that palladium black cannot activate. In polymer media, the ligands can also prevent the precipitation of palladium black from palladium (II) complexes.

2.1.5 The geometrical effect of Ru complexes on the oxidation of 1,6-hexanediol to ϵ -caprolactone

The demand for ϵ -caprolactone (ϵ -CL) has been steady growth as it is a feedstock in polycaprolactone (PCL) and nylon-6 production (> 4 million tons a year)

[40, 41]. Due to the biodegradable and biocompatible properties of PCL [42-45], it could substitute petroleum-based polymers [46-50], particularly for medical applications [51-54]. Typically, ϵ -CL can be produced from the oxidation of 1,6-hexanediol (1,6-HD), a biomass derivative obtained from the hydrogenation of 5-hydroxymethylfurfural (HMF) and levulinic acid [55, 56]. Key challenge of this process is the oxidation of primary alcohol with consecutive cyclization. Accordingly, single-site metal complexes are proposed as a catalyst for effective oxidation under a mild condition with facile cyclization via the coordinate mechanism at the metal center.

Metal oxo complexes, such as ruthenium [57-59], iron [60-62], and cobalt [63-65], can act as a catalyst for alcohol oxidation with an oxidizing agent, e.g., H_2O_2 and/or NaIO_4 . This reaction is suggested to proceed via a radical intermediate generated from $\text{M}^{n+1}=\text{O}$ species [66, 67]. However, the metal oxo complexes generally provide a low activity due to the high stability of the reduced metal hydroxide species ($\text{M}^n\text{-OH}$). While non-oxo Ru complex (L_nRu) catalysts promote non-radical oxidation via alcohol insertion and β -hydrogen elimination. The reaction rate is also suppressed due to a relatively stable Ru-H intermediate, as reported by Espino *et al.* [68]. Hence, hydrogen acceptors are generally used to convert the Ru-H intermediate. Murahashi *et al.* used PhNO_2 , *p*-benzoquinone, and diphenylacetylene as hydrogen acceptors to enhance $\text{RuH}_2(\text{PPh}_3)_4$ activity [69]. This is similar to the "Oppenauer process" where alcohol is oxidized over a metal complex catalyst in the presence of ketone hydrogen acceptors [70].

In diols oxidation to lactone, most of these catalysts were limited by the cyclization due to a higher degree of freedom around the metal center. Half-sandwich non-metal oxo complexes, on the other hand, had been reported to provide higher regioselectivity and activity [71]. For example, Heeres *et al.* reported that the combination of $[(p\text{-cymene})\text{RuCl}_2]_2$ and bis(diphenylphosphino) ferrocene (DPPF) promotes 1,6-HD oxidation to ϵ -CL in acetone [72]. Ikariya *et al.* also successfully used $\text{Cp}^*\text{RuCl}[\text{Ph}_2\text{P}(\text{CH}_2)_2\text{NH}_2-\kappa^2\text{-P,N}]$ in the presence of *t*-BuOK for lactonization of 1,4-butanediol [27]. They suggested that, in addition to the polyhaptic ligand (Cp^*), phosphine and ammine ligands play a crucial role in enantioselectivity in the Oppenauer oxidation. However, excessive oxidation to dicarboxylic acid is often found in hygroscopic solvents. Alternatively, using a non-polar solvent could suppress the formation of a dicarboxylic acid and enhance the interaction between the complex

This material is reserved for educational use only, not allowed for commercial use.

Forbidden to modify the content, and cite the document when use.

and the feed (1,6-HD), leading to the higher cyclized product (ϵ -CL). On top of that, these unidentate ligands' electronic and geometrical effects on the reaction kinetics and cyclization selectivity have not been clarified. Moreover, the mechanism for associating the diols with the metal complex has still been debated [73-81].

Herein, the oxidation of 1,6-HD to ϵ -CL using (*p*-cymene)RuCl₂(L) as a catalyst was investigated in a non-polar medium (toluene). The influence of unidentate phosphine and ammine ligands (L_P and L_N) in half-sandwich Ru complexes on the activity and ϵ -CL selectivity was determined in the presence of methyl *iso*-butyl ketone (MIBK) as a hydrogen acceptor. XANES was used to determine the electronic structure of the complex in the reaction solution. Accessible pocket-site resulting from different ligands was evaluated from the crystal structure. The correlation between the apparent rate constant with both the electronic and geometrical aspects was explored to support a reaction pathway previously proposed by computational studies. The effect of bases was investigated, and the cause of the catalyst deactivation was also highlighted.

2.1.6 Literature reviews

Many researchers have worked on tunable geometrical properties of an active specie for a fascinating chemical reaction. It has been a key to attaining new opportunities for many syntheses in the decade.

Benitez *et al.* (2009) [82] investigated the electronic and geometrical effect of Au complexes coordinated with phosphine ligand in allene-dienes cycloaddition. The electronic property and their transition state structures were computed by the density functional theory (DFT). They found that the [4+3] cycloaddition without Au complexes gave the reaction barrier (ΔG^\ddagger) of 14.6 kcal.mol⁻¹. In contrast, [4+2] cycloaddition would be facilitated using phosphine Au complexes giving $\Delta G^\ddagger \sim 8$ kcal.mol⁻¹. An alkyl shift was determined rate-determining step that would occur with ΔG^\ddagger of 6.1, 6.0, and 5.7 kcal/mol for [AuP(^tBu)₂(*o*-biPh)]⁺, [AuP(OPh)₃]⁺, and [AuPPh₃]⁺, respectively. This suggested that the ability of electron transfer from Au *dπ*-electrons to C *pπ*-orbital and their structure leads to a lower ΔG^\ddagger for the cycloaddition reaction.

Wang *et al.* (2019) [83] investigated the Pd cluster's size-dependent electronic and electronic effect on aerobic oxidation of benzyl alcohol. A volcano curve of the activity and benzaldehyde selectivity vs. Pd particle sizes was observed. It was found

that Pd with the size of 4.5 nm provided the highest turnover frequency ($4.4 \times 10^4 \text{ h}^{-1}$). However, the highest benzaldehyde selectivity (94%) was observed using 20 nm of the Pd particle size. It implied that an ensemble effect of Pd resulted in a shift in benzyl alcohol and its reactive intermediate adsorption energy. The decrease in Pd particle size might decrease a work function and increase the adsorption strength of benzyl alcohol.

Kaminsky *et al.* (1997) [84] applied a chlorinated and fluorinated half-sandwich ligand to Ti complexes for styrene polymerization. Cyclopentadienyl (Cp) Ti complexes provided a relatively higher activity ($207 \text{ kg.mol}^{-1}.\text{h}^{-1}$) compared to TiCl_3 ($9 \text{ kg.mol}^{-1}.\text{h}^{-1}$). As pentamethyl cyclopentadienyl ligand (Cp^*) was used, the activity decreased to $157 \text{ kg.mol}^{-1}.\text{h}^{-1}$ because of the electron donation ability and its steric hindrance. Even though methyl-substituted cyclopentadienyl ligand contributed to lower activity, the syndiotactic polymerization would be promoted.

Pal *et al.* (2018) [85] synthesized $\text{Cp}^* \text{ Rh}$ and Ir complexes for the dehydrogenation of dimethylamine–borane combined with the DFT calculation and spectroscopic evidence. It was reported that Rh complexes provided a relatively higher activity ($\text{TOF } 52 \text{ h}^{-1}$) compared to Ir complexes (3 h^{-1}). This is because the formation of $\text{Rh}(\eta^4\text{-Cp}^*\text{H})$ was more favorable for the proton shuttling process during a reversible hydride transfer mechanism.

Yao *et al.* (2017) [86] synthesized half-sandwich Cp Ir complexes with the Schiff base ligands. The 4-trifluoromethyl group coordinated aromatic ligands gave the highest norbornene polymerization activity. This suggested that the electron-deficient metal center was more promising for the olefin coordination and insertion. Moreover, the 2-methylbenzyl-Ir complex offered a higher activity than those of 4-methylalkoxy (4-OMe) and 4-trifluorocarbon groups (4- CF_3). This is because ortho-substituted groups bonded aromatic rings could prevent polymerization's chain transfer process ($\beta\text{-H}$ elimination).

Gonell *et al.* (2020) [87] reported that the trans-effect of Ru complexes plays a crucial role in controlling the catalytic activity and stability of the catalyst in CO_2 electroreduction. The coordination of the pyridine ligand assists in a faster Cl dissociation rate compared to the N-heterocyclic carbene (NHC) ligand. For this reason, a higher CO electroreduction rate of 1000 s^{-1} was observed. Moreover, the geometrical effect was also studied by varying the NHC ligand's bite angle. They mentioned that

This material is reserved for educational use only, not allowed for commercial use.

Forbidden to modify the content, and cite the document when use.

closed proximity in the bite angle (90°) would weaken the trans effect on the Ru complexes. This leads to a lower basic metalcarboxylic acid ($M-C(O)OH$) and a slower overall reaction rate.

Navarro *et al.* (2020) [88] synthesized (*p*-cymene) Ru complexes with the different pyridylideneamide (PYA) ligands for tuning electronic and structural properties. The catalyst was applied for the hydrogen transfer reaction with *i*-PrOH (hydrogen donor) and KOH (base, 100/10/1 substrate/base/catalyst ratio). They found that the phenyl coordinated Ru complexes provided a complete conversion within 4 h. However, the Ru complexes with chelating carbene or zwitterionic PYA provided a slower reaction rate. The activity increased with ligand donation ability (phenyl > PYA \approx N-heterocyclic carbene > pyridine).

Joel *et al.* (2016) [58] synthesized ruthenium (III) complexes with bidentate N, N'-ligands for alcohol oxidation using NaO_4 as an oxidant. They reported that the Ru complexes with a *p*-cymene ring provided complete conversion within 30 min compared to those with a benzene ring. This suggested that the *p*-cymene ring could stabilize Ru (VI)=O intermediate upon the oxidation via a radical process. The Ru=O intermediate would be reacted with alcohol via β -H elimination forming Ru(V)-OH species. It was then reacted with an adjacent Ru=O for active site recovery. Moreover, higher activity was observed for the oxidation of 4-methyl cyclohexanol compared to 2-methyl cyclohexanol. This was suggested that a less steric hindrance of 4-methyl cyclohexanol leads to higher feed accessibility.

Aliende *et al.* (2012) [68] synthesized arene Ru (II) half-sandwich compounds with the functional ligand 4,4'-dimethoxy-2,2'-bipyridine (dmobpy) for transfer hydrogenation and alcohol oxidation. In the transfer hydrogenation process, the spectroscopic evidence showed that hydrido Ru complex (Ru-H) would be generated from β -H elimination. It could rapidly transfer hydrogen to another carbonyl compound yielding alcohol, respectively. Additionally, TOF values of 8400-9000 h^{-1} were reported upon alcohol oxidation using $tBuOOH$. However, no conversion was observed for the oxidation using H_2O_2 as an oxidant.

Naota *et al.* (1998) [69] described the oxidation of alcohol via the hydrogen transfer process. The alcohol reacted with the Ru center giving aldehyde and Ru dihydride (RuH_2). The Ru hydride intermediate was then responded with a hydrogen acceptor for recovering and continuing the catalytic cycle. In the reaction without a

This material is reserved for educational use only, not allowed for commercial use.

Forbidden to modify the content, and cite the document when use.

hydrogen acceptor, the Ru hydride could be retrieved by hydrogen gas liberation. In contrast to the conventional oxidation, the hydrogen transfer process was affected by steric hindrance around the Ru center, offering a particular chemo selectivity, especially for a lactonization. Moreover, this process favored primary alcohol, while conventional oxidation preferred secondary alcohol.

Maria *et al.* (1996) [89] studied Oppenauer-type oxidations of secondary alcohols to ketones. The oxidation was performed in refluxing acetone using phosphine or benzyl Ru complexes. This reaction was more favorable for aliphatic alcohol. The activity for the oxidation of cyclic alcohol depends on the geometrical of the reactant and Ru complex. A higher reactivity of cyclopentanol (90% yield) than cyclohexanol (20% yield) could be observed. However, the activity would be decreased under wet conditions ($H_2O > 0.6\%$) because of the competitive nucleophilic addition of water.

Ito *et al.* (2007) [27] studied the oxidation of a secondary alcohol and 1,4-butanediol in acetone using $Cp^*RuCl[Ph_2P(CH_2)_2NH_2-\kappa^2-P, N]$ with $tBuOK$. Extremely high activity for secondary alcohol oxidation would be observed. However, the reversible hydrogen transfer of ketone products could lead to the racemization of a chiral nonracemic secondary alcohol. Additionally, $Cp^*RuCl(Ph_2P(CH_2)_2NH_2)$ gave a relatively higher yield (>99%) compared to $Cp^*RuCl(1,5-cyclooctadiene)$ (<1%). This suggested amino ligand could play a significant role in the oxidation of diol. Though lactol was an intermediate, only diol and lactone could be observed, as evidenced by spectroscopic data. This suggested that lactol was in virtual equilibrium between the diol, which was rapidly converted compared to the formation of aldehyde via the Tischenko mechanism.

Ito *et al.* (2011) [90] examined the oxidation of 2-benzyl-1,4-butanediol in acetone at 30 °C for 1 h using $Cp^*RuCl(Ph_2PCH_2CH_2NH_2)$ as a catalyst. It provided β -benzyl- γ -lactone and α -benzyl- γ -lactone with a molar ratio of 77: 23. They suggested that using less steric hindrance [$(\eta^5-C_5H_5)Ru(CH_3CN)_3$] PF_6 would provide a product with non-regioselectivity. In contrast, using methyl-substituted Ru complex ($Cp^*RuCl(Ph_2PCH_2CH_2NH_2)$) would positively affect the regioselectivity. Moreover, a structural change in its phosphine-nitrogen ligand also improved selectivity. They also mentioned that the diol and lactol intermediate were interconverted in the oxidation.

The lactol could act as a hydrogen acceptor in the reaction without t BuOK, promoting disproportionation into the diol and isomeric lactones.

Buntara *et al.* (2011) [26] investigated the conversion of 1,6-hexanediol to caprolactone using, 1,1'-bis(diphenylphosphino)ferrocene (DPPF) and methyl iso-butyl ketone (MIBK) as a hydrogen acceptor. It was the first study on the oxidation of 1,6-hexanediol. Using MIBK instead of acetone could increase the reaction temperature due to the higher boiling point and hence the reaction rate. Moreover, the oxidation of 1,6-hexanediol proceeded entirely with high selectivity. However, the primary form of catalysts was not evaluated since DPPF can act as a ligand of the Ru complexes during the reaction.

2.2 Acetylene/ethylene metathesis

2.2.1 Ethylene [91]

Ethylene, chemical formula C_2H_4 , is the simplest olefinic hydrocarbon containing a single C=C bond ($H_2C=CH_2$). It is colorless, flammable, and sweet in taste and odor, naturally found in natural gas, petroleum, and plant hormones during ripening. Ethylene is a crucial chemical for the petrochemical industry. It can be produced from natural gas, ethane, propane, and naphtha cracking at 800-900 °C, giving a mixture of light gases. The melting point of ethylene is -169.4 °C, and while boiling point is -103.9 °C.

The commercial process increases the most considerable use of ethylene beyond one-half of all hydrocarbons. It is commonly used as a monomer in ethylene polymerization for a higher hydrocarbon and plays a significant role as a chemical feedstock for other worthy derivatives. The ethylene polymerization yields polyethylene, a polymer in domestic and household, especially for the packaging, coating, and container. The ethylene polymerization is carried out under high pressures and temperatures, giving low-density polyethylene (LDPE), which has different properties than the high-density polyethylene (HDPE) yielded from the polymerization over Ziegler-Natta catalysts.

2.2.2 Acetylene [92]

Acetylene, known as ethyne, is the simplest hydrocarbon with the triple bond in the acetylenic series or alkynes. It is a colorless and flammable gas frequently used as burning fuel in oxyacetylene welding and metal cutting. It is also a raw material for manufacturing many organic chemicals and plastics.

Pure acetylene is colorless gas holding a pleasant odor. Generally, it is prepared from the reaction between calcium carbide and water. However, traces of phosphine gas can be yielded as a side product causing a pungent garlic-like odor. Acetylene is readily decomposed into its elements, releasing heat. However, the acetylene decomposition could or could not give an explosion, depending on its place conditions. For example, pure acetylene gas under pressure above 15 pounds per square or in liquid or solid form can explode with extreme violence. Mixtures of acetylene in the atmosphere are explosive over a wide range of air concentrations, from about 2.5-87%. As it is burned with a particular air concentration, acetylene flame gives a pure white light. It can use to illuminate during the lack of electric power, for instance, buoys, lamps, and traffic signals. The heat combustion of acetylene produces a significant amount of energy. Thus, it is correctly applied for a torch with the highest oxyacetylene flame temperature (~6,000 °F, or 3,300 °C) over a known other mixture of combustible gases.

2.2.3 1,3-Butadiene [93]

1,3-Butadiene, the unsaturated hydrocarbon molecule with the simple chemical formula $(\text{CH}_2=\text{CH})_2$ (**Scheme 2.5a**). By the number of the double bond and its structure, it is the simplest conjugated diene with four carbon atoms. It is a colorless gas easily condensed to a liquid at a high concentration under ambient conditions. It is also industrially used as a monomer for synthetic rubber. Though it can be decomposed suddenly in the atmosphere, it is still found in the ambient air in urban and suburban areas from motor vehicle pollution. Butadiene can be found in another isomer, 1,2-butadiene, from the accumulation of double bonds in its carbon chain (**Scheme 2.5b**).



Scheme 2.5 The structure of a) 1,3-butadiene and b) 1,2-butadiene

It can be used to produce synthetic rubber such as SBR, SBS, and thermoplastic rubber. It can be used for the domestic household to make shoes, wheels, parts for the car industry, adhesives and sealants, asphalt, and polymer modification. Industrially, it was produced as a by-product of ethylene manufacturing from the steam cracking process. It was then separated by feeding into a butadiene extraction unit or extractive distillation process.

2.2.4 Cyclohexene [94]

Cyclohexene is an unsaturated hydrocarbon containing a six-membered carbon ring with the formula of C_6H_{10} . It is a colorless liquid with a pungent odor. It is used as an intermediate for a variety of industrial processes. However, it is not stable upon long-term storage under exposure to the light and air forming peroxide derivatives. It is commercialized by the partial hydrogenation of benzene established by the Asahi Chemical company. Firstly, the benzene can be converted to cyclohexylbenzene by acid-catalyzed alkylation and cyclohexene as a side product. Nonetheless, cyclohexylbenzene is used as a chemical feedstock to produce phenol and cyclohexanone. The successive hydration of cyclohexene also gives cyclohexanol, which is dehydrogenated to give cyclohexanone, a precursor to caprolactam, respectively. The oxidative cleavage of cyclohexene with hydrogen peroxide over tungsten catalyst yields adipic acid. It is also a precursor to the synthesis of maleic acid, dicyclohexyladipate, and cyclohexene oxide. Moreover, it can be used as a painting and polymer industry solvent.

2.2.5 Metathesis [95]

Metathesis, probably named a bond displacement reaction, involves an exchange of bonds between two molecules resulting in the products with an identical binding association. The bond between two molecules can be both ionic and covalent. Traditionally, one product can be precipitated from the metathesis reaction. The

This material is reserved for educational use only, not allowed for commercial use.

Forbidden to modify the content, and cite the document when use.

double decomposition is frequently encountered in old literature, where the name is more exclusively mentioned whenever one of the substances is separated from the solvent (by the ligand or ion exchange in the solid-state system).

2.2.5.1 Olefins metathesis

Olefin metathesis is the organic reaction, usually found in the petrochemical process, caused by the reorganization of the olefins by the fragmentation and recombination of carbon-carbon double bonds (**Scheme 2.6**).



Scheme 2.6 A representation of olefins metathesis

However, it often produces unwanted hazardous products because of the relatively active olefinic compounds. The olefin metathesis can be activated by the organometallic complexes and metal oxide catalysts, for example, Ti complexes, Re complexes, Ru complexes, MoO₃, Re₂O₇, and WO₃-based catalysts. The metathesis is commonly activated over a heterogeneous catalyst in the industrial process. Nonetheless, a well-defined organometallic complex seems to be more active than those solid-supported catalysts. The heterogeneous catalysts can be prepared from in situ activations of its metal salt, such as metal halide, together with organoaluminium or organotin compounds (WCl₆-EtOH-EtAlCl₂). The supports were commercially used to prepare a well-dispersed catalyst. Commercial catalysts are often based on molybdenum and ruthenium. At the same time, a well-defined organometallic complex is mainly exploited in small-scale production or academic research.

The homogeneous-based catalysts are categorized as Schrock-type catalysts and Grubbs-type catalysts. Schrock-type catalysts are mainly composed of molybdenum (VI)- and tungsten (VI)-based centers coordinated alkoxide and imido ligands, as shown in **Figure 2.3**.

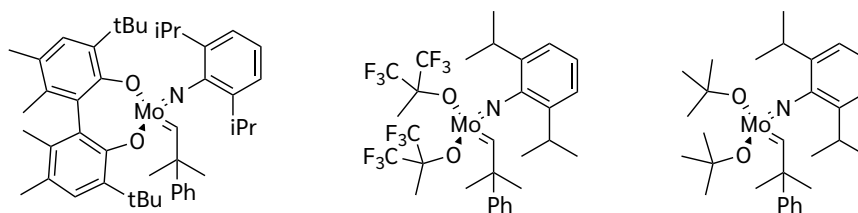


Figure 2.3 Molybdenum (VI)- and tungsten (VI)-based centers coordinated alkoxide and imido ligands.

Grubbs catalysts are ruthenium (II)-based carbene complexes modified with an isopropoxy-benzylidene ligand. It was commercialized under the name of the Hoveyda–Grubbs catalyst (**Figure 2.4**).

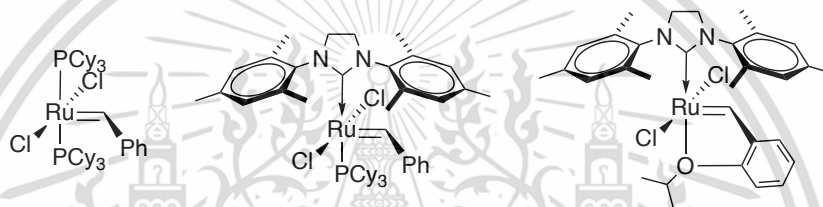


Figure 2.4 Hoveyda–Grubbs catalysts

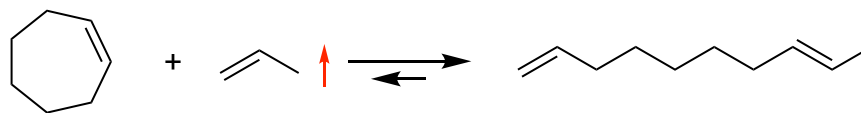
2.2.5.2 Olefin metathesis' thermodynamic

As the olefin metathesis causes a slight change in enthalpy (yielding new olefinic products with a similar structure), the product distributions are commonly related to the entropy change, according to the Le Chatelier's Principle. For example, cross- and ring-closing metathesis with alpha-olefins, a reverse reaction, ethenolysis, is possible under high ethylene pressure (high ethylene concentration), as shown in **Scheme 2.7**.



Scheme 2.7 1-Butene/propylene cross-metathesis

Similarly, the reverse reaction of ring-opening metathesis is more favorable at high alpha-olefins concentration. Additionally, the ability of ring strain release is also a driving force for ring-opening metathesis (**Scheme 2.8**).



Scheme 2.8 Cycloheptene/ethylene ring-opening metathesis

The ring-closing metathesis of a bulkier macromolecule was kinetically performed under high dilution conditions. The ring-closing metathesis for five- or six-membered rings seems more enthalpically favorable. Moreover, from Thorpe–Ingold effect, the reaction rate for intra-molecular cyclization would be enhanced by a steric hindrance of the molecule. Thus, bulkier higher olefins could be more favorable than those from light olefins.

2.2.5.3 Olefin metathesis mechanism [96]

Hérisson and Chauvin firstly proposed the mechanism of alkene metathesis over transition metal oxide catalysts. Typically, a direct [2+2] cycloaddition between two olefins is hindered by a structural forbidden (two-body collision), consequently in high activation energy. Chauvin's mechanism involves the [2+2] cycloaddition over a metal alkylidene, forming a metallocyclic intermediate. Subsequently, it was decomposed by a cycloelimination, giving a new alkene and alkylidene active site (**Figure 2.5**). The association with d-orbitals of metal can decrease the activation energy - a modest temperature.

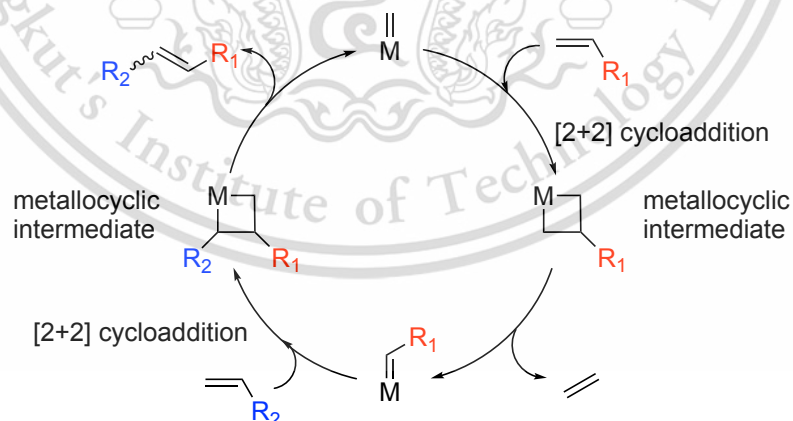


Figure 2.5 Olefins metathesis' mechanism

This material is reserved for educational use only, not allowed for commercial use.

Forbidden to modify the content, and cite the document when use.

2.2.5.4 Heterogeneous catalysts for the olefin metathesis

A supported heterogeneous metal oxides of group VI and group VII, such as molybdenum, tungsten, and rhenium, are often employed in industrial processes. WO_3 -supported silica was firstly used for propene self-metathesis in the Triolefin process developed by Phillips. On the other hand, a reverse reaction produced propylene was commercialized by ABB Lummus Technology at Houston's approach. An alpha olefins production for plasticizers and detergents was developed by Shell Higher Olefins Process (SHELL). $\text{MoO}_3/\text{Al}_2\text{O}_3$ or WO_3/SiO_2 -based catalysts were used in the worldwide olefins production with the efficiency of 1.2 million tons/year. However, with the production condition and a wide-ranging olefins feed, WO_3 was frequently used because of its poisoning resistivity (from sulfide and oxygenated compounds) and reproductivity.

WO_3 over SiO_2 support exists in various forms; mono-oxo, di-oxo WO_3 , and polymeric WO_3 , as shown in **Figure 2.6**. At high WO_3 loading, the polymeric WO_3 , which is less active than those mono- and dioxo WO_3 , can be formed [97].



Figure 2.6 A molecular structure of a) di-oxo, b) mono-oxo, and c) polymeric WO_3

2.2.5.5 Diel-Alder reaction [98]

Diels-Alder reaction involves in [4+2]-cycloaddition between a conjugated diene and a dienophile (alkene/alkyne) in 4π -electrons of diene and 2π -electrons of dienophile. The driving force for the reaction depends on the formation of new energetically stable σ -bonds compared to the π -bonds. For an alkynyl dienophile metathesis, the alkynyl adduct can also act as a dienophile in case it is not too sterically hindered. Moreover, the reaction between diene and dienophile could cumulate the double bond forming a substituted allene (no conjugated system). With an easy operation, it is the most prevailing synthetic method for unsaturated six-membered rings such as cyclohexene. It can also perform in the reaction between the

heteroatom-containing diene or the dienophile (nitrogen or oxygen atom) in an alternative synthesis of a six-membered ring heterocyclic compound.

The highest occupied MO of the diene (HOMO) and the lowest unoccupied MO of the dienophile (LUMO) overlapping thermally occurs in Diels-Alder Reaction because it is afforded in the orbitals with similar energy (**Figure 2.7**). The reaction can be facilitated by an electron-withdrawing group, CHO, COR, COOR, CN, C=C, Ph, or halogen, on a dienophile due to the lower energy of LUMO. On the other hand, the diene should possess an electron-donating group for increasing HOMO energy.

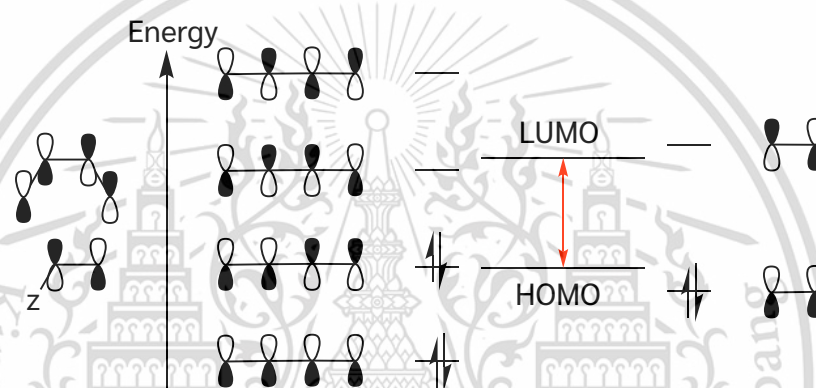


Figure 2.7 HOMO-LUMO of Diels-Alder reaction.

2.2.6 The geometrical effect of WO_3 species on acetylene/ethylene metathesis

Ethylene is an essential chemical building block widely used for polymerization in polymer synthesis. It is traditionally produced from the naphtha steam cracking process at high temperatures ($\sim 700^\circ\text{C}$), where hydrocarbon feedstock is thermally cracked to ethylene, propylene, and butene with a trace of polyunsaturated products, such as acetylene and butadiene [99-102]. However, high purity ethylene is particularly required for polymerization because polyunsaturated impurities readily poison the Ziegler-Natta catalyst, leading to a rapid deactivation [103-107]. Accordingly, selective hydrogenation of acetylene is typically applied for high purity ethylene treatment, exploiting expensive platinum and palladium catalysts. However, competitively

excessive ethylene and acetylene hydrogenation to low-valued ethane and coke formation were very common.

One of the promising routes to selectively remove acetylene from the ethylene-rich feed is the cross-metathesis of acetylene/ethylene to produce 1,3-butadiene worthily. In addition to selective removal of acetylene, the 1,3-butadiene formed are valuable feedstocks for butadiene-styrene and acrylonitrile-butadiene-styrene copolymers. For acetylene/ethylene cross-metathesis, T. Ioan-Teodor *et al.* [108] successfully applied ruthenium carbene complex under the homogeneous system with approximately 70% selectivity of 1,3-butadiene. However, relatively high pressure (11-14 bar) and low temperature (80 °C) were required, and the catalyst can be readily deactivated due to acetylene polymerization. While naphtha steam cracking is operated at low pressure (<2 bar) and high temperature (>700 °C), it is unlikely that such a homogeneous system can be practically applied.

Alternatively, heterogeneous catalysts, such as tungsten oxide (WO_3), molybdenum oxide (Mo_2O_3), rhenium oxide (Re_2O_7), and their mixed oxide have been reported for metathesis. WO_3 supported catalyst is the most promising for low-pressure/high-temperature metathesis due to its high stability, low feed sensitivity, and toxicity. It was suggested that the activity was increased with time and stable after 2 h indicating WO_3 was a pre-catalyst for the propylene metathesis, suggesting that the olefin can reduce WO_3 to form tungsten alkylidene species [109]. However, not all WO_3 was uniformly active since the activity was decreased with the formation of bulk WO_3 , in contrast to monomeric WO_3 , formed by strong interaction with the supports [110]. Mono- and di-oxo WO_3 were found at low metal loading and more active than those polytungstate at a high loading [97]. In a supportive manner, 1-octene metathesis using 8wt.% WO_3/SiO_2 provides low 7-tetradecene selectivity, as compared to that of 2wt.% WO_3/SiO_2 [111]. While bulk WO_3 preferably promotes isomerization and coke formation.

To obtain highly dispersed mono- and di-oxo WO_3 , low loading WO_3 on support with a high surface area, would be considered. The surface OH groups (silanol) adjacent to the active W site assisted in styrene metathesis giving the higher conversion [112]. Moreover, to activate mono-oxo Mo(IV) species with propene, the silanol-assisted pathway is more kinetically accessible than the non-OH-assisted mechanism [113]. The silanol not only assisted in the activation but also affected the structural stabilization

This material is reserved for educational use only, not allowed for commercial use.

Forbidden to modify the content, and cite the document when use.

of the surface metal oxide species. Therefore, the amount and type of silanol over the surface would be essential to improve the activity. Furthermore, introducing the Lewis acid site (Al^{3+}) can improve the catalytic performance of $\text{WO}_3/\text{Al-MCM-41}$ for 1-butene/ethylene cross-metathesis attributing to the maximum monomeric WO_3 species and the higher metal-support interaction [114]. However, the cross-metathesis of acetylene/ethylene over supported WO_3 catalysts has never been reported.

In this work, the selective acetylene/ethylene cross-metathesis using WO_3 -supported SiO_2 , MCM-41, SBA-15, NaY, and NaX, were investigated for selective acetylene removal from the ethylene-rich feed. The effect of pretreatment conditions (ethylene and H_2 treatment) and WO_3 loading on the formation of active WO_3 and $\text{W}=\text{CH}_2$ species were investigated using Raman and Time-Resolved X-ray Absorption Spectroscopy (TR-XAS). The role of the supports with Al-OH and confined structure on the dispersion of WO_3 active sites was also studied. The proximity of $\text{W}=\text{CH}_2$ species was also highlighted.

2.2.7 Literature reviews

Ioan-Teodor *et al.* (2012) [115] studied acetylene/ethylene metathesis using Hoveyda-Grubbs second-generation catalyst. It was found that acetylene conversion and 1,3-butadiene selectivity were increased with the ethylene/acetylene molar ratio. However, 1,3-butadiene selectivity was limited at 50% at 80 °C with 10 mg catalyst in 20 mL CH_2Cl_2 , ethylene/acetylene=32.5 mix at a total pressure of 14 bar. Moreover, the catalyst deactivation would be observed from the formation of propylene, butene, C5 dienes, and C6 polyunsaturated.

Debecker *et al.* (2013) [109] prepared $\text{WO}_3\text{-SiO}_2\text{-Al}_2\text{O}_3$ catalysts by an aerosol process for ethylene/butene cross-metathesis. They found that the catalysts prepared from the aerosol process had a higher metal dispersion ($0.5\text{W atoms}\cdot\text{nm}^{-2}$) than the conventional impregnation ($1.0\text{W atoms}\cdot\text{nm}^{-2}$). It offered a higher surface area, and the strong interaction between WO_3 and $\text{SiO}_2\text{-Al}_2\text{O}_3$ support forming a short $\text{W}=\text{O}$ bond which was not easily reduced by H_2 . Furthermore, this catalyst was found to be the most active for propene metathesis ($65\text{ mmol}\cdot\text{g}^{-1}\cdot\text{h}^{-1}$) compared to the conventional $\text{WO}_3\text{-SiO}_2\text{-Al}_2\text{O}_3$ ($45\text{ mmol}\cdot\text{g}^{-1}\cdot\text{h}^{-1}$) and WO_3/SiO_2 ($2\text{ mmol}\cdot\text{g}^{-1}\cdot\text{h}^{-1}$), respectively. They suggested that electron-withdrawing Al would deliver a positive effect on the formation of the carbene.

This material is reserved for educational use only, not allowed for commercial use.

Forbidden to modify the content, and cite the document when use.

Chauvin *et al.* (2015) [110] investigated the effect of surface tungsten oxide (WO_3) species on isopropanol dehydration. The formation of WO_3 species was controlled by WO_3 loading and evaluated by the spectroscopic method. They found that the surface WO_3 species (di-oxo or mono-oxo WO_3) could be generated at $0.7 \text{ atom W}\cdot\text{nm}^{-2}$. At higher WO_3 surface density, amorphous or crystalline WO_3 could be formed. The lower WO_3 dispersion led to a lower isopropanol conversion and TOF (WO_x surface species \approx amorphous $\text{WO}_3 >$ crystalline WO_3).

Lwin *et al.* (2016) [97] investigated the effect of surface tungsten oxide (WO_3) species on propylene metathesis. The formation of WO_3 species was examined by *in situ* spectroscopy. At below 8% WO_3 loading, mono- and dioxo WO_3 were present as an active site for propylene metathesis. However, polymeric WO_3 was obtained at higher WO_3 loading. The catalyst with the predominant dioxo- WO_3 species gave the highest propylene conversion compared to the others. An acidity of WO_3 , especially polymeric WO_3 , was also attributed to propylene dimerization, isomerization, and polymerization.

Chan *et al.* (2019) [116] synthesized pyridine oxo tungsten complex supported SiO_2 catalysts for nonene metathesis. They suggested W=O species were a pre-catalyst acquiring an activation. Upon removing pyridine ligands, the activity was increased ($14\text{-}28 \text{ min}^{-1}$) compared to fresh catalysts (0.01 min^{-1}). They also suggested that the catalysts with higher OH group density were more effective for forming active tungsten (IV) alkylidene species in olefins without allylic C-H group via a proton-assisted initiation mechanism. However, both olefins with and without the allylic group were involved in a critical proton-transfer process.

Handzlik *et al.* (2021) [113] studied the formation of an active molybdenum species and the effect of the surface silanol group combined with the DFT calculation. They suggested that the alkylidene Mo species were generated from the olefinic reduction of dioxo-Mo (VI) species to mono-oxo Mo (IV) species. It was then reorganized to Mo (VI) alkylidene species. They also mentioned that this silanol-assisted mechanism was more favorable than the others, such as the pseudo-Wittig mechanism, 2-hydrogen shift mechanism, allyl mechanism, and oxidative coupling mechanism.

CHAPTER 3

Research methodology

3.1 Reagents

Chemicals	Grade of Purity	Manufactures
1. Dichloro (<i>p</i> -cymene) ruthenium (II) dimer	100%	Aldrich
2. Triphenylphosphine (PPh ₃)	99%	Sigma-Aldrich
3. Triphenylphosphite (P(OPh) ₃)	97%	Aldrich
4. Tricyclohexylphosphine (PCy ₃)	100%	Aldrich
5. 4-Dimethylaminopyridine	98%	Fluka
6. 1,6-Hexanediol	97%	Aldrich
7. Adipic acid	99%	Acros Organics
8. Potassium <i>tert</i> -butoxide (^t BuOK)	98%	Aldrich
9. Potassium carbonate (K ₂ CO ₃)	99%	Rankem
10. (2-Ethoxyethyl) (diphenyl) phosphine oxide	100% 96%	Aldrich Aldrich
11. 4- <i>tert</i> -Butylpyridine	99%	Aldrich
12. 4-Methylpyridine	97%	Aldrich
13. 2,4-Dichloropyridine	97%	Aldrich
14. 4-(Trifluoromethyl) pyridine	99.8%	Carlo Erba
15. Toluene	85.5%	Carlo Erba
16. Potassium hydroxide (KOH)	99%	Acros Organics
17. ϵ -Caprolactone (ϵ -CL)	99%	Emplura
18. Methyl iso-butyl ketone (MIBK)	98%	Aldrich
19. 1-Methyl-2-pentanol (MIBC)	99%	Acros Organics
20. Dodecane	-	-
21. Deionized water	37%	Carlo Erba
22. Hydrochloric acid	99%	Carlo Erba
23. Pyridine	99.98%	Fischer
24. Dichloromethane	-	Carlo Erba
25. Petroleum ether	99.9%	Carlo Erba

This material is reserved for educational use only, not allowed for commercial use.

Forbidden to modify the content, and cite the document when use.

26. Methanol	99.0%	RCI Labscan
27. Ethanol	99.99%	Praxair
28. Air-zero	99.99%	United Industrial Gas
29. High purity N ₂	99.999%	United Industrial Gas
30. Ultra-High purity N ₂	99.9%	Fluka
31. Ammonium metatungstate hydrate	99.9	Aldrich
32. Davisil [®] SiO ₂	-	Carlo Erba
33. Zeolite NaY (Si/Al=200)	-	Carlo Erba
34. Zeolite NaX (Si/Al=1)	-	Aldrich
35. Triblock copolymer Pluronic P123	37%	Carlo Erba
36. Hydrochloric acid	96%	Carlo Erba
37. Sulfuric acid	99%	Aldrich
38. Tetraethyl orthosilicate (TEOS)	30-50%	Aldrich
39. Sodium silicate	96%	Aldrich
40. Cetyltrimethylammonium bromide (CTAB)	99%	Carlo Erba
41. 1-Hexene		

3.2 Apparatuses

1. Laboratory glassware
2. Hotplate and stirrer
3. Hot-air oven
4. Dual manifold
5. Horizontal tube furnace
6. NMR tube
7. Filter paper, Whatman, No. 41
8. 4 Digits precision weighing balance, Mettler Toledo, ME403
9. Micropipette, Mettler Toledo

This material is reserved for educational use only, not allowed for commercial use.

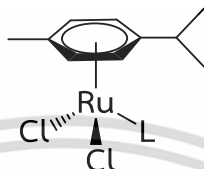
Forbidden to modify the content, and cite the document when use.

3.3 Experimental procedure

3.3.1 the oxidation of 1,6-hexanediol using Ru complex as catalysts

3.3.1.1 Synthesis of (*p*-cymene)RuCl₂(L)

The typical structure of Ru complexes ((*p*-cymene)RuCl₂(L)) with a particular ligand (L) was represented in **Scheme 3.1**.



Scheme 3.1 a short representation of Ru-complexes

The ligands (L) were designated as L_P (for phosphine-based) and L_N (for pyridine-based), composing a variety of ligands as shown in **Table 3.1**.

Table 3.1 a series of the ligands L_P and L_N

L _P	Phosphine Ligands	L _N	Pyridine Ligands
L _{P1}	P(Cy) ₃	L _{N1}	Pyridine
L _{P2}	P(OPh) ₃	L _{N2}	4-methylpyridine
L _{P3}	PO(Ph ₂)(C ₂ H ₅)	L _{N3}	4- <i>tert</i> -butylpyridine
L _{P4}	PPh ₃	L _{N4}	2,4-dichloropyridine
L _{P5}	bis(diphenylphosphino)methane	L _{N5}	4-dimethylaminopyridine

The Ru complexes were synthesized similar to those reported in the literature [117-123]. Briefly, for L_P, (*p*-cymene)RuCl₂(L_{P1}) was synthesized from 1 mmol ([Ru(*p*-cymene)Cl₂]₂) and 2 mmol tricyclohexylphosphine in 60 mL of methanol refluxing under an inert atmosphere at 60 °C for 1 h to obtain a red crystal. (*p*-cymene)RuCl₂(L_{P2}) was synthesized from 1 mmol ([Ru(*p*-cymene)Cl₂]₂) and 2 mmol triphenyl phosphite in 100 mL of hexane. The solution was refluxed for 5 h and evaporated to obtain a red crystal.

(*p*-cymene)RuCl₂(L_{P3}) was synthesized from 1 mmol ([Ru(*p*-cymene)Cl₂]₂) and 2 mmol (2-ethoxyethyl)(diphenyl) phosphine oxide in 40 mL dichloromethane under an ambient condition overnight. The red-brown crystal was washed several times with

This material is reserved for educational use only, not allowed for commercial use.

Forbidden to modify the content, and cite the document when use.

diethyl ether. (*p*-cymene)RuCl₂(L_{P4}) was synthesized from 1 mmol ([Ru(*p*-cymene)Cl₂]₂) and 1 mmol triphenylphosphine in 25 mL of methanol. The solution was stirred under an ambient condition for 1 h to obtain a red-brown crystal. The crystal was washed several times with methanol and diethyl ether and dried at 60 °C. (*p*-cymene)RuCl₂(L_{P5}) was taken from Asst. Prof. Dr.Nararak Leesakul, Department of Chemistry and Center for Innovation in Chemistry, Faculty of Science, Prince of Songkla University.

For pyridine-based ligands, (*p*-cymene)RuCl₂(L_{N1}) was synthesized by the reaction of 1 mmol ([Ru(*p*-cymene)Cl₂]₂) and 2 mmol pyridines in 30 mL toluene under refluxing for 3 h to obtain a yellow crystal. It was filtrated and washed with hexane, respectively. (*p*-cymene)RuCl₂(L_{N2}) was synthesized from 1 mmol [Ru(*p*-cymene)Cl₂]₂ and 4 mmol 4-methylpyridine in 200 mL methanol. The solution was refluxed for 4 h to obtain a red crystal. (*p*-cymene)RuCl₂(L_{N4}) and (*p*-cymene)RuCl₂(L_{N5}) were synthesized from 1mmol [Ru(*p*-cymene)Cl₂]₂ and 2 mmol 2,4-dichloropyridine or 4-dimethylaminopyridine in 50 mL tetrahydrofuran. The solution was vigorously stirred for 1 h to obtain a dark yellow crystal.

A new (*p*-cymene)RuCl₂(L_{N3}) was synthesized from the reaction between 1 mmol [Ru(*p*-cymene)Cl₂]₂ and 2 mmol of 4-*tert*-butyl pyridine in 40 mL dichloromethane under an ambient condition overnight. The red-brown crystal was washed with diethyl ether several times and recrystallized in the mixture of petroleum ether and dichloromethane solution (3:1 by volume).

3.3.2 Acetylene/ethylene metathesis using WO₃-supported catalysts

3.3.2.1 SBA-15 synthesis [124]

SBA-15 was synthesized by adding 18.7 g of a triblock copolymer Pluronic P123 and ethanol in 10.8 g of 35% HCl solution. 40.2 g of TEOS was added to the gel composition of 1.0TEOS: 0.017P123: 5.7HCl: 173H₂O: 40C₂H₅OH. Subsequently, the solution was vigorously stirred at 35 °C for 20 h. Then, the solution was transferred to a Teflon-lined stainless-steel autoclave and autogenously heated at 80 °C for 24 h. Afterward, the precipitate was washed, dried at 60 °C overnight, and calcined at 550 °C for 6 h with the ramping rate of 1 °C·min⁻¹, respectively.

3.3.3.2 MCM-41 synthesis [125]

A solution of 9.90 g of sodium silicate in 30 mL deionized water was added dropwise to the solution of 8.12 g cetyltrimethylammonium bromide (CTAB) in 80 mL deionized water. The pH of the suspension was adjusted to 12 by 2M H₂SO₄ solution. The mixture was vigorously stirred under an ambient condition for 1 h, transferred to a Teflon-lined stainless-steel autoclave, and hydrothermally treated at 100 °C for 48 h. The white particle was collected, dried at 60 °C overnight, and calcined at 550 °C for 6 h with the ramping rate of 1 °C·min⁻¹, respectively.

3.3.3.3 WO₃ catalysts preparation

The catalysts were considered for preparing at 2, 3, 5, and 7%WO₃/SiO₂. Ammonium metatungstate hydrate was used as a precursor. It was dissolved in deionized water to make the solution with a final concentration of 0.5 M. The solution was dropped onto the supports and dried at 110 °C overnight under an ambient condition. The dried impregnated catalyst was calcined in a horizontal tube furnace at 500 °C for 5 h with a heating rate of 5 °C·min⁻¹ under airflow (60 mL·min⁻¹). For other supports (NaY, NaX, MCM-41, and SBA-15), WO₃ loading was prepared at 5% wt. in a similar procedure.

3.3.4 Characterization

3.3.4.1 NMR

¹H and ¹³C NMR spectra were characterized by BrukerDPX-500 and JEOL Resonance JNM-ECZ500R spectrometer (500 MHz). The sample was dissolved and diluted using deuteriochloroform (CDCl₃) and deuterotoluene (toluene-d₈) as a solvent. ¹³C magic angle spinning (MAS) NMR spectra were recorded using a JEOL Resonance JNM-ECZ500R spectrometer (400MHz).

3.3.4.2 Matrix-assisted laser desorption ionization-time of flight mass spectrometer (MALDI-TOF MS) and fast liquid chromatography quadrupole Time-of-Flight (QTOF) Mass Spectrometry (LC-QTOF)

A mass per charge (m/z) of a new (*p*-cymene)RuCl₂(L_{N3}) complex was counted on microflex®, Bruker, matrix-assisted laser desorption ionization-time of flight mass spectrometer (MALDI-TOF MS) using acetonitrile as diluent. A mass per charge (m/z) of a Ru(MIBC)₄ complex was measured on micrOTOF-Q, Bruker, electrospray ionization-time of flight mass spectrometer (LC-QTOF)

This material is reserved for educational use only, not allowed for commercial use.

Forbidden to modify the content, and cite the document when use.

3.3.4.3 X-ray crystallographic refinement

A single crystal of a new (*p*-cymene)RuCl₂(L_{N3}) was recrystallized in a mixture of dichloromethane and diethyl ether. The diffraction was performed by a Bruker APEX-II CCD diffractometer with graphite-monochromated Mo K_α radiation ($\lambda = 0.71073 \text{ \AA}$), 33925 reflections. The diffraction was collected by APEX3, SAINT, and SADABS, solved by ShelXT software and refined by SHELXL to obtain the structural information. Anisotropic thermal parameters were refined for all non-hydrogen. All hydrogen atoms were placed in the calculation. The WinGX and Olex2 1.3 programs were used to prepare the materials and molecular graphics for publication. The crystallographic structure was obtained from the supports by Asst. Prof. Dr. Nararak Leesakul, Department of Chemistry and Center for Innovation in Chemistry, Faculty of Science, Prince of Songkla University.

3.3.4.4 CHN analysis

CHN elemental composition of the complex was quantitatively measured by the Flash Smart, Thermo Scientific, CHNS/O analyzer.

3.3.4.5 UV-VIS spectroscopy

UV-VIS spectra were collected on GENESYS 10S with the wavelength region scanned from 200-800 nm at 0.4 nm of the resolution. An acquiring time in the scanning was set at 15 s.

3.3.4.6 Diffuse reflectance UV-VIS spectrophotometer

The sample 0.1 g was mixed and ground in the crystal of barium sulfate (~1g) for dilution. It was subsequently pressed on the sample holder, covered by a quartz slide, and measured on UV-VIS spectrometer, T92+, PG instruments using pure boric acid for a baseline correction. The spectra were collected from the range of 200-800 nm.

3.3.4.7 X-ray diffractometry

The crystallinity and structural characteristics of the catalysts were identified by X-ray diffraction spectrophotometer, DMAX2200 Ultima+ (Rigaku) diffractometer by Cu K_α radiation ($\lambda = 1.504056 \text{ \AA}$). The powder was finely ground prior to pressing on the sample holder. The data was collected at Bragg angle (2θ) from 0.5-10° and 5° to 90° with the scanning rate of 5° min⁻¹.

3.3.4.8 Wavelength Dispersive X-ray fluorescence spectrophotometer (WD-XRF).

0.5 g of sample powder was mixed and ground in 4.5 g of boric acid before putting in an Al₂O₃ pan. Subsequently, the number of elements embedded in the sample was measured by a Wavelength Dispersive X-ray fluorescence spectrophotometer, S8 Tiger using CuK α radiation ($\lambda = 1.504056 \text{ \AA}$).

3.3.4.9 Specific surface area and pore size distribution

The surface area, pore size distribution, and adsorption isotherm of the samples were measured by Autosorb-1, Quantachrome. The catalysts were introduced to the glass cell equipped with degassing station. The cell was evacuated at 350 °C under vacuum to vanish the gas and moisture on the sample surface. Subsequently, cryogenic N₂ was subjected to the sample and measured an adsorption-desorption from 10⁻⁶-10⁻¹ torr of P/P₀. The surface area was calculated based on the BET equation. The pore size was also determined by the BJH method.

3.3.4.10 Acidity and acid strength

~0.2 g of the sample was pelletized by a swing arm hydraulic press at ~1 ton for 1 min and crushed into 700-850 μm . The pellets were packed into a quartz tube in the middle of quartz wool slabs. Subsequently, it was activated at 500 °C for 2 h under air-zero (30 mL \cdot min⁻¹) before saturating by 1%mol NH₃ in He with the flow rate of 30 mL \cdot min⁻¹ for an hour. An excessive of NH₃ molecules on the sample surface was purged by helium flush. The data was collected from 30-900 °C at step size 0.004 with a heating rate of 10 °C \cdot min⁻¹ by microvolume Thermal conductivity detector, VICI, Valco instrument. The peak area was calibrated by a pulse of 1%mol NH₃ in He in a 100 μL sample loop.

3.3.4.11 Temperature programmed reduction (H₂-TPR)

The sample was prepared and activated by a similar procedure as section 3.3.4.7. The reducibility of the sample was measured in 10%H₂/Ar background. The data was collected from 50-900 °C at step size 0.004 with a heating rate of 10 °C \cdot min⁻¹ by microvolume Thermal conductivity detector, VICI, Valco instrument. The peak area was calibrated by a pulse of 1%mol H₂ in Ar in a 100 μL sample loop and CuO standard.

3.3.4.12 Thermogravimetric analysis

The ethylene-treated sample's thermogravimetric analysis curve (TGA) was recorded under an oxidative atmosphere (air-zero). ~5-10 mg of sample was weighed into a micro Al₂O₃ crucible and placed into a heating chamber in a thermogravimetric analyzer, TGA/DSC1, Mettler Toledo. The sample was monotonically heated from 30 to 900 °C at the heating rate of 5 °C·min⁻¹ under the flow of air-zero (30 mL·min⁻¹).

3.3.4.13 Fourier Transform Raman spectroscopy

A Fourier Transform Raman spectroscopy (FT-Raman) was collected by Raman spectrometer, Nanoproton, Ramantouch (force) with 785 nm laser, the laser excitation 6.11 mW, exposure time 100 s, from a wave number of 0 to 2000 cm⁻¹ using Si as standard.

3.3.4.14 X-ray Absorption spectroscopy

X-ray absorption spectroscopy (XAS) was measured by the support from beamline 8 SUT-SLRI XAS of Synchrotron Light Research Institute (SLRI) (Public Organization), Thailand. 2.5 mmol of the Ru complex and 8.0 mmol of MIBK (1.0 mL) were dissolved in 29 mL of toluene stored in a polypropylene bag. KCl, RuCl₃, and ([Ru(*p*-cymene)Cl₂)₂) were used as a standard. The electron energy was 1.25-10.0 keV, beam current 80-150 mA, and maximum photon flux was about 1.0×10⁸-10¹⁰ photon·100 m·s⁻¹. The X-ray beam size was 10 mm (width) × 1 mm (height). The germanium (220) double single crystals were used as a monochromator to probe Ga element for X-ray absorption near edge structure (XANES). The spectra were normalized, processed, and analyzed on Athena software.

Time-resolved X-ray absorption spectroscopy (TRXAS) was conducted with the support of beamline 2.2 XAS of the Synchrotron Light Research Institute (SLRI), Thailand. W L₃-edge XANES and EXAFS spectra were measured in transmission mode using a Si (111) bent-crystal monochromator and a linear image NMOS sensor. The data were collected simultaneously during the experiment. The sample was primarily activated under air-zero (30 mL·min⁻¹) at 500 °C with a heating rate of 2 °C·min⁻¹ and held for 3 h. Subsequently, the temperature was raised to 600 °C with a heating rate of 10 °C·min⁻¹ under He (30 mL·min⁻¹). The vapor of 1-hexene in He (45 °C) was introduced (30 mL·min⁻¹) into the chamber using a saturator at weight hourly space velocity (WHSV) 45 h⁻¹ when the temperature reaches 600 °C. The 1-hexene treatment

This material is reserved for educational use only, not allowed for commercial use.

kept activated for 1 h together with the data collection. The spectra were normalized, processed, and analyzed on Athena software. The coordination and structural information were determined on Artemis software using W_2O_7 and WO_3 as a model structure.

3.3.5 General procedure for the oxidation of 1,6-hexanediol

A reaction vessel was equipped with vacuum and inert gas N_2 through the dual manifold connecting with a set of the reaction vessel; a round bottom flask, a condenser, and a paraffin washing bottle, as shown in **Figure 3.1**. A round bottom flask was charged with 0.2 mmol bases (K_2CO_3 , KOH, or $tBuOK$) and 1 mmol of 1,6-hexanediol. After being evacuated by 3 cycles of vacuum and N_2 purge, 20 mL of a stock solution containing 2.5mM of the Ru complex in toluene/MIBK (30:1 by volume) was injected into the reaction vessel. 10 mL of the toluene/MIBK was added to make the final volume of 30 mL. 1,6-Hexanediol oxidation occurs by vigorously stirring at 110 °C under an N_2 atmosphere. An aliquot was taken at the time, added 1 mL of 1M HCl, and quenched in an ice bath (-5 °C). The supernatant was separated, added with 0.1 mL of *n*-dodecane as internal standard, made a final volume of 1 mL using toluene, and analyzed by GC-FID, Agilent 7890B, equipped with MXT-1 column and FID-detector.

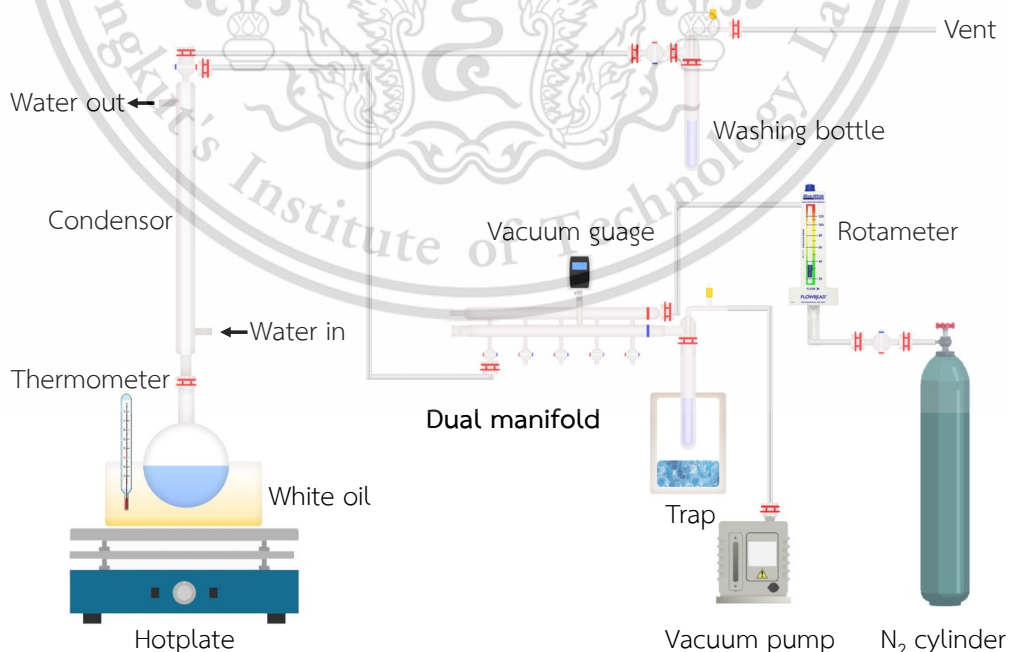


Figure 3.1 Schematic diagram for the oxidation of 1,6-hexanediol

This material is reserved for educational use only, not allowed for commercial use.

Forbidden to modify the content, and cite the document when use.

3.3.6 General procedure for the acetylene/ethylene metathesis

WO₃ supported catalysts were pressed on a swing arm hydraulic press and sieved in 600-850 micrometer sizes. It was packed into an 8 mm diameter quartz tube between quartz wool slabs. The quartz beads were filled on top to adjust the feed flow profile. The fragmented quartz rod was also placed at the bottom. Prior to the activity testing, the catalyst was activated under air-zero (30 mL·min⁻¹) at 500 °C for 4 h. N₂ was introduced during a ramping temperature to 600 °C. Subsequently, the catalyst was treated with ethylene (30 mL·min⁻¹) for 2 h. The temperature was held at 450 °C together with the introduction of 1%mol acetylene/ethylene balanced with N₂ (total flow 55 mL·min⁻¹). It would be noted that higher flow gas was subjected through the upper flow controller to maintain a constant flow. The gas product was collected every 20 min for 6 h using 250 μL of a sample loop by online GC, Agilent 6890, equipped with HP-plot (Al₂O₃) column and FID-detector. The fixed-bed reactor scheme is represented in **Figure 3.2**.

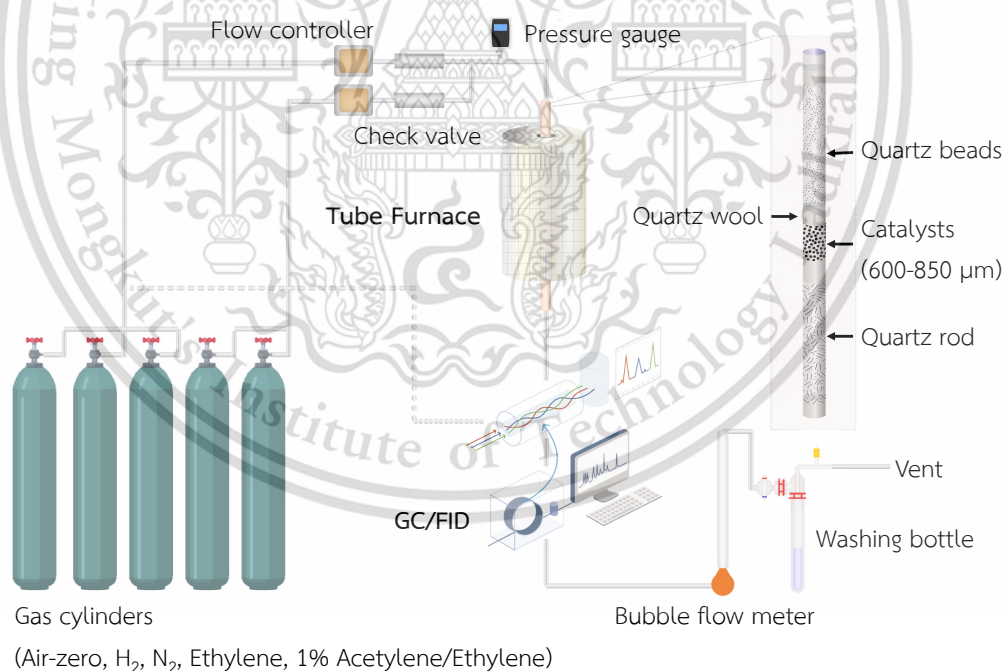


Figure 3.2 Schematic diagram for acetylene/ethylene metathesis

CHAPTER 4

Main results and discussion

4.1 The catalytic oxidation of 1,6-hexanediol to ϵ -caprolactone over (*p*-cymene)RuCl₂(L) complexes

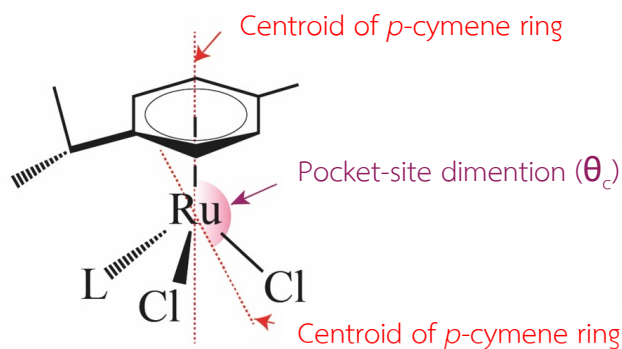
4.1.1 Syntheses

NMR spectra and crystallographic details of the new (*p*-cymene)RuCl₂(L_{N3}) complex are shown in Table A1 and Figure A1–A3 (Appendix A) [117–123], respectively. Other (*p*-cymene)RuCl₂(L) compounds with phosphine ligands (L_{P1–P5}), and pyridine-base ligands (L_{N1–N5}), shown in Table 4.1, were prepared by the reaction between commercially available [(*p*-cymene)RuCl₂]₂ and the corresponding ligands in methanol, as reported in the literature (Figure A4–A10, Appendix A).

Table 4.1 L_P and L_N ligands for the (*p*-cymene)RuCl₂(L) complexes

L _P	Phosphine ligands	L _N	Pyridine ligands
L _{P1}	P(cyclohexyl) ₃	L _{N1}	Pyridine
L _{P2}	P(OPh) ₃	L _{N2}	4-Methylpyridine
L _{P3}	PO(Ph ₂)(C ₂ H ₅)	L _{N3}	4- <i>tert</i> -Butylpyridine
L _{P4}	PPh ₃	L _{N4}	2,4-Dichloropyridine
L _{P5}	Bis(diphenylphosphino) methane	L _{N5}	4-Dimethylaminopyridine

The steric and electronic effects of the ligands could be derived from the different cone angles of the L_P ligands or the other substituted groups of the pyridine ring for L_N ligands. All complexes have pseudo-tetrahedral geometry, as shown in Scheme 4.1.



Scheme 4.1 Structure of the (*p*-cymene)RuCl₂(L) complexes

According to the single-crystal XRD of all (*p*-cymene)RuCl₂(L) complexes, the Ru–Cl(1), Ru–Cl(2), Ru–N or Ru–P, and Ru–(centroid of the *p*-cymene ring) bond lengths varied depending on the ligands (L), as shown in **Table A2, Appendix A**. For (*p*-cymene)RuCl₂(L_N) complexes, the N–Ru–(centroid of the *p*-cymene ring) angles are in the same range (127–129°). However, these angles are somewhat smaller than that of the (*p*-cymene)RuCl₂(L_P) (128–134°). This could be attributed to the greater steric hindrance of bulky phosphine ligands. It is worth noting that other angles have changed to accommodate this variation.

As previous studies suggest that the catalytic initiation process of this type of complex involves the association of the feed, especially alcohols [78, 79], the angle of the (centroid of *p*-cymene ring)–Ru–L would determine the accessibility of a reactant to coordinate with the complex. The geometrical effect from these ligands can be deduced from the “pocket-site” defined by an accessible space around the angle of (centroid of the *p*-cymene ring)–Ru–(centroid of 2Cl) (θ_c), as shown in **Scheme 4.1**, due to the lower steric hindrance of the chloro-ligands.

One could expect that θ_c would depend on the geometrical effect of the L–Cl–Cl ligands, especially the steric constraints from L. As seen in **Table 4.2**, the bulkier the L, the larger the Ru-cone angle, and hence the smaller the θ_c . The complex with a smaller θ_c would have a relatively smaller pocket-site dimension. Accordingly, the θ_c of L_N complexes is larger than those of the L_P complexes. This is because the L_N (planar structure ligands) is much less bulky than L_P (trigonal pyramidal structure ligands). It should be noted that the modification of the pyridine ring (L_N) results in a

slight change of θ_c . On the other hand, a considerable variation of the θ_c was observed for L_P with different P-substituted moieties.

Table 4.2 Pocket-site dimension (θ_c , °) of (*p*-cymene)RuCl₂(L)

Entry	Ligands	θ_c (°)
1	L_{P1} P(cyclohexyl) ₃	140.09
2	L_{P2} P(OPh) ₃	143.29
3	L_{P4} PPh ₃	143.63
4	L_{P5} Bis(diphenylphosphino) methane	145.21
5	L_{N1} Pyridine	148.28
6	L_{N2} 4-Methylpyridine	147.67
7	L_{N3} 4- <i>tert</i> -Butylpyridine	147.96
8	L_{N5} 4-Dimethylaminopyridine	147.63

4.1.2 Catalytic activity

The oxidation of 1,6-HD using (*p*-cymene)RuCl₂(L_{P4}) as a catalyst at 1 h (**Figure 4.1a**) yielded ϵ -CL as the main product with small amounts of 6-hydroxyhexan-1-al and 1,6-hexanedial. A trace of adipic acid was also obtained. According to the reaction profile (**Figure 4.1a**), 6-hydroxyhexan-1-al was initially produced, presumably from the oxidation at one of the hydroxyl groups of 1,6-HD. As the conversion increased, the yield of 6-hydroxyhexan-1-al was decreased, while ϵ -CL yield was increased. This suggests that 6-hydroxyhexan-1-al is an intermediate undergoing consecutive cyclization and oxidation to the ϵ -CL. In a similar manner, 1,6-hexanedial was also initially produced but then decreased with the conversion. This product could be derived from the oxidation of 6-hydroxyhexan-1-al but then consumed, presumably by H-transfer from the Ru-H intermediate. Alternatively, some 1,6-hexanedial could be further oxidized to a trace amount of adipic acid [126].

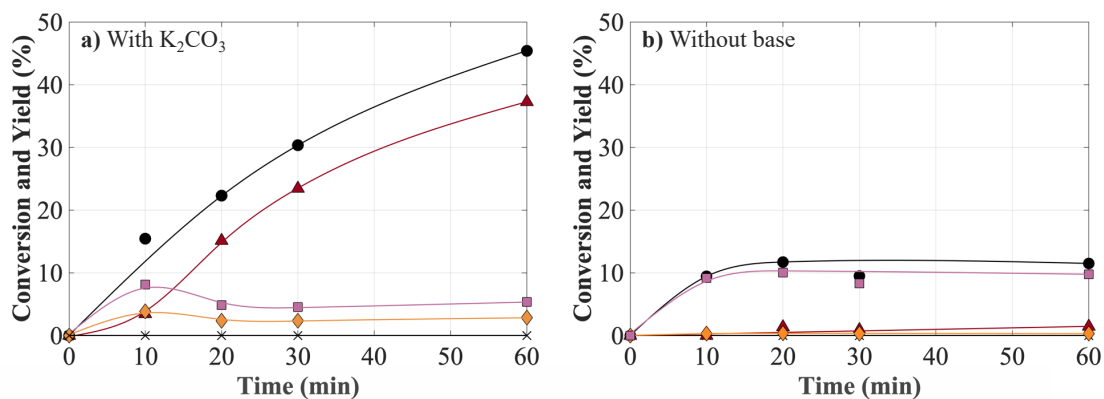


Figure 4.1 1,6-HD oxidation time profile using the $(p\text{-cymene})\text{RuCl}_2(\text{L}_{\text{P}4})$ catalyst a) with K_2CO_3 and b) without base (conversion (●), 6-hydroxyhexan-1-al (■), 1,6-hexanedial (◆), $\epsilon\text{-CL}$ (▲), and adipic acid (×) (0.025 mmol Ru complex, 1 mmol 1,6-HD, under N_2 atmosphere, 110 °C, 30 mL toluene, 0.2 mmol K_2CO_3 , 8 mmol MIBK))

In sharp contrast, lower activity was obtained when no K_2CO_3 was added to the reaction (**Figure 4.1b**). In this case, 6-hydroxyhexan-1-al was mainly produced with a small amount of $\epsilon\text{-CL}$. Deprotonation and association of 1,6-HD to the catalyst complex could likely be suppressed in the absence of a base. This is because the proton abstraction of the primary alcohol (1,6-hexanediol) would be faster than that of the secondary alcohol (oxepan-2-ol). Thus, further cyclization and oxidation would be limited in the absence of a base, while the initial product, 6-hydroxyhexan-1-al, can be obtained with/without the base. Another report [127] also suggested that no reaction takes place without a base; this finding emphasizes that K_2CO_3 is required, particularly for the oxidation of oxepan-2-ol intermediate to $\epsilon\text{-CL}$.

For the phosphine ligands ($\text{L}_{\text{P}1\text{-P}5}$), the conversions of $(p\text{-cymene})\text{RuCl}_2(\text{L}_{\text{P}})$ catalysts in the presence of K_2CO_3 increased from 4 to 55% for $\text{L}_{\text{P}1}$ to $\text{L}_{\text{P}5}$ (**Table 4.3, entries 2–6**). 6-Hydroxyhexan-1-al and $\epsilon\text{-CL}$ are produced as major products. From the reaction profiles (**Figure A11, Appendix A**), all reactions follow pseudo 1st order kinetics, as shown in **Figure 2a**. Accordingly, the apparent rate constants (k_{app}) can be estimated, which is consistent with the observed conversion (**Table 4.3**). The k_{app} increases in the order of $\text{L}_{\text{P}1} < \text{L}_{\text{P}2} < \text{L}_{\text{P}3} < \text{L}_{\text{P}4} < \text{L}_{\text{P}5}$, which is ~100 times from $\text{L}_{\text{P}1}$ to $\text{L}_{\text{P}5}$. Hence, the phosphine ligands clearly influence the reaction activity. This could be attributed to the i) electronic and/or ii) geometric effect of the phosphine ligands in the $(p\text{-cymene})\text{RuCl}_2(\text{L}_{\text{P}})$ complexes.

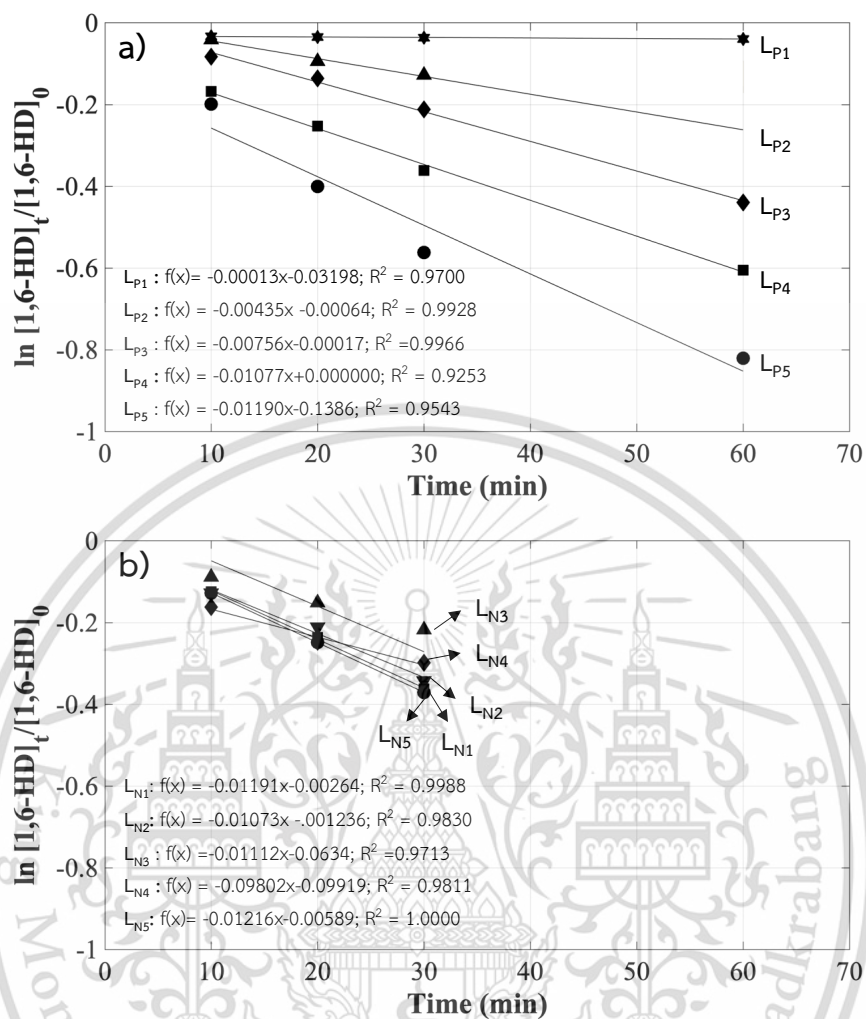


Figure 4.2 Pseudo 1st order kinetics of 1,6-HD oxidation using a) (*p*-cymene)RuCl₂(L_p) and b) (*p*-cymene)RuCl₂(L_N) catalysts (0.025 mmol Ru complex, 1 mmol 1,6-HD, under N₂ atmosphere, 110 °C, 30 mL toluene, 0.2 mmol base, 8 mmol MIBK)

Table 4.3 Conversion and product distribution using (*p*-cymene)RuCl₂(L) complexes as catalysts

Entry	Ligand	θ_c (°)	Base	Conversion (%) ^b	Yield (%)				k_{app}^a (x 10 ⁻³ min ⁻¹)
					6-Hydroxy hexan-1-al	1,6-Hexanedial	Adipic acid	ϵ -CL	
1	L _{P4}	143.63	-	11	9.3	0.0	0.0	1.7	-
2	L _{P1}	140.09	K ₂ CO ₃	4	3.9	0.0	0.0	0.1	0.1
3	L _{P2}	143.29	K ₂ CO ₃	14	9.2	0.0	0.0	4.8	4.6
4	L _{P3}	-	K ₂ CO ₃	36	9.9	0.4	0.0	25.7	7.6
5	L _{P4}	143.63	K ₂ CO ₃	46	3.2	4.6	0.0	38.2	10.8
6	L _{P5}	145.21	K ₂ CO ₃	55	11.1	2.1	0.1	41.7	11.9
7	L _{N1}	148.28	K ₂ CO ₃	42	8.3	2.4	0.1	31.2	11.9
8	L _{N2}	147.67	K ₂ CO ₃	50	10.0	1.8	0.0	38.2	10.1
9	L _{N3}	147.96	K ₂ CO ₃	47	3.9	3.1	0.0	40.0	11.1
10	L _{N4}	-	K ₂ CO ₃	30	10.1	0.0	0.0	20.1	9.8
11	L _{N5}	147.63	K ₂ CO ₃	47	4.3	3.2	0.1	39.5	12.2

^a (0.025 mmol Ru complex, 1 mmol 1,6-HD, under N₂ atmosphere, 110 °C, 1 h, 30 mL toluene, 0.2 mmol K₂CO₃, 8 mmol MIBK). ^b Conversion and yields after 60 min resident time.

However, there does not seem to be an electronic effect derived from these phosphine ligands since the electron density of the Ru center in all the (*p*-cymene)RuCl₂(L_P) complexes remains similar despite the different L_P ligands. This was deduced from the X-ray adsorption near-edge structure (XANES) spectroscopy of these (*p*-cymene)RuCl₂(L_P) complexes in the toluene solution (imitating the reaction solution), as shown in **Figure 4.3a** and **a'** and **Table 4.4**. In fact, the Ru L₃-edge energy for all complexes was observed at ~2834 eV. In turn, the Cl K-edge energy notably decreases from L_{P1} > L_{P2} > L_{P3} > L_{P4} > L_{P5} (2820.2 to 2817.5 eV, **Table 4.4**, **entries 1-5**, and **Figure 4.3a'**). In other words, the lower the steric hindrance from the L_P, the higher the electron density of the Cl ligand. According to the crystallographic data, the L_P ligand with less steric constraints showed a shorter Ru–P bond (**Table A2**, **entries 1-3**, **Appendix A**), providing a stronger interaction with the Ru center. Accordingly, a lower interaction between Ru and the Cl ligand could be expected, leading to a longer

This material is reserved for educational use only, not allowed for commercial use.

Forbidden to modify the content, and cite the document when use.

Ru–Cl bond. This suggests that the chloro-ligand in the complex with less sterically bulky ligands would have a weaker sigma donation to the Ru (a longer Ru–Cl bond), yielding a lower electron density. It is possible that the similar electron density at the Ru center of these (*p*-cymene) RuCl₂(L_P), despite the difference in L_P ligands could be compensated by the arrangement of the Ru–Cl, Ru–P, and Ru–C bonds. Accordingly, the electronic effect by the ligand may not account for the observed difference in the activity of the (*p*-cymene)RuCl₂(L_P) catalysts.

Table 4.4 Ru L₃-edge energy and Cl K-edge energy of (*p*-cymene)RuCl₂(L) complexes

Entry	Ligand	Ru L ₃ -edge energy (eV)	Cl K-edge energy (eV)
1	L _{P1}	2834.1	2820.2
2	L _{P2}	2834.2	2819.4
3	L _{P3}	-	-
4	L _{P4}	2834.2	2819.1
5	L _{P5}	2834.2	2817.5
6	L _{N1}	2833.9	2819.0
7	L _{N2}	2834.2	2819.2
8	L _{N3}	2834.0	2819.0
9	L _{N4}	2834.0	- ^a
10	L _{N5}	-	-
11	[(<i>p</i> -cymene)RuCl ₂] ₂	2832.7	2819.8

^a Cl K-edge energy cannot be determined since there is the additional Cl which is substituted on the pyridine-based ligand.

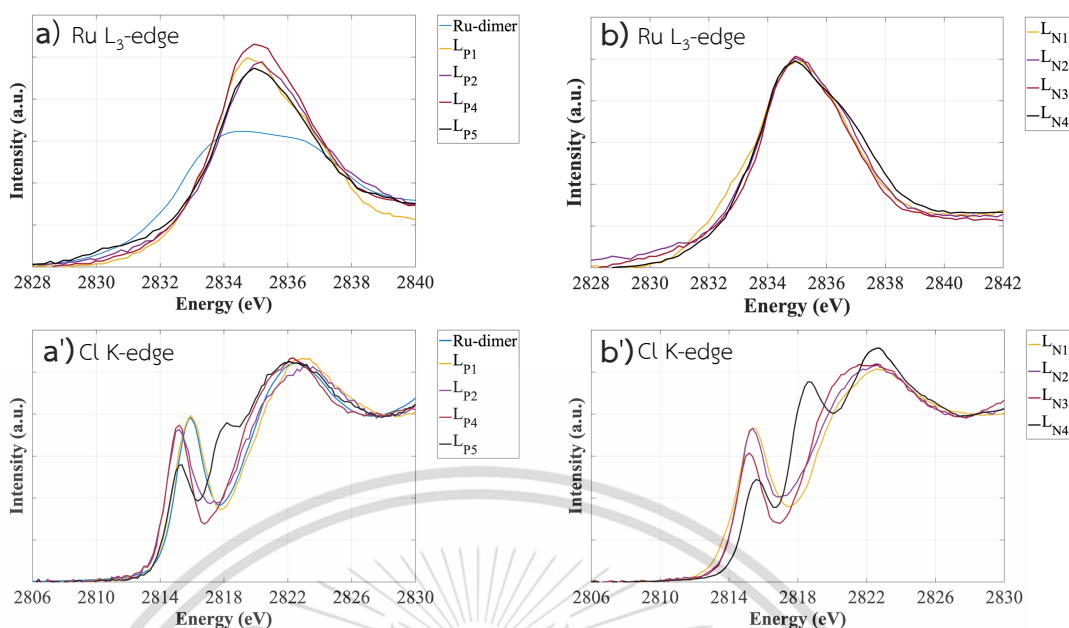


Figure 4.3 XANES spectra of Ru L₃-edge and Cl K-edge energies of a) and a') (*p*-cymene)RuCl₂(L_P) and b) and b') (*p*-cymene)RuCl₂(L_N) in toluene

On the other hand, the reaction rate constant (k_{app} , **Table 4.3, entries 2–6**) increases when the L_P ligands become less sterically bulky, suggesting a geometric effect from the L_P ligands. This indicates that the accessibility of 1,6-HD to the ruthenium center plays a crucial role in the reaction pathway. In fact, the reaction rate constants (k_{app}) for the (*p*-cymene)RuCl₂(L_P) complexes critically depend on the θ_c , as depicted in **Figure 4.4**. As mentioned earlier, the less steric hindrance caused by the L_P, the larger the θ_c . The variation of θ_c from only 140–145° leads to an increase in k_{app} values by 100 orders of magnitude. The larger the pocket-site dimension, as deduced from θ_c , the higher the reaction rate [128, 129]. Accordingly, the reaction pathway appears to proceed via an associative interchange (I_a) mechanism for (*p*-cymene)RuCl₂(L_P) complexes, as shown in **Scheme 4.2**. These kinetic data (**Figure 4.2 and 4.4**) are the first experimental evidence supporting the associative interchange mechanism for alcohol oxidation among the debated mechanisms by computational studies [74, 81]. Accordingly, it seems that the difference in the substituted groups of L_P does not significantly affect the electron density at the Ru center but rather the Ru–Cl bond length, which regulates accessibility. This again indicates the geometrical effect of the phosphine ligand on the observed activity. The increase in the rate

constant for the L_p complex with a larger pocket-site dimension (θ_c) could suggest the associative interchange mechanism of 1,6-HD oxidation (Scheme 4.2).

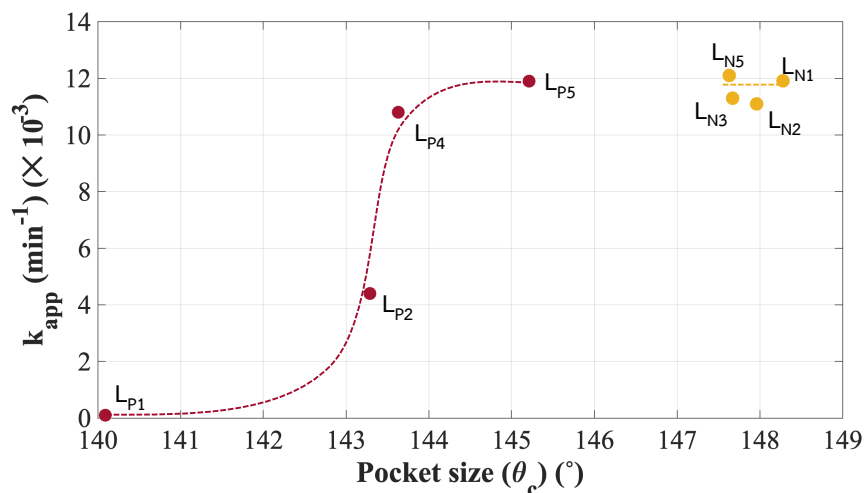
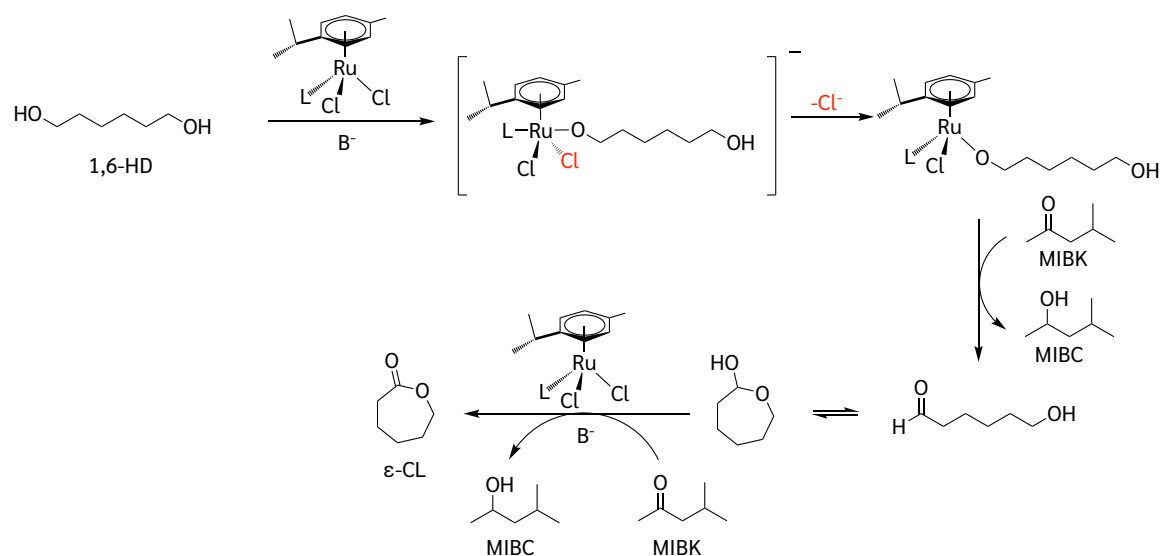


Figure 4.4 Relation between k_{app} and the pocket size dimension of (*p*-cymene) $RuCl_2(L)$ complexes



Scheme 4.2 Possible pathway for the 1,6-HD oxidation over (*p*-cymene) $RuCl_2(L)$

However, the k_{app} values of the (*p*-cymene) $RuCl_2(L_N)$ complexes are relatively similar ($\sim 10\text{--}12 \times 10^{-3} \text{ min}^{-1}$, Table 4.3, entries 7-11, Figure 4.2b) and independent of θ_c (Figure 4.4). This suggests that the accessibility of the 1,6-HD to the ruthenium center of the L_N complexes is not limited. In other words, (*p*-cymene) $RuCl_2(L_N)$ has enough space for the feed association. Besides the independence of the pocket-size dimension (θ_c), the similar activity amongst L_N complexes could be the reason for their similar electronic properties (Figure 4.3b and b'). For all (*p*-cymene) $RuCl_2(L_N)$

complexes, the edge energies of Ru were similar (~ 2834 eV, **Table 4.4, entries 6–9**) and relatively close to those of the (*p*-cymene)RuCl₂(L_P) complexes. This suggests that the Ru center in these complexes (both L_N and L_P) possesses a similar electron density. Despite different L_N ligands, Ru–N and Ru–Cl bonds are in the same range (2.1 Å and 2.4 Å, respectively, **Table A2, Appendix A**). This is presumably because the difference in substituted groups (–Cl, –CH₃, –N(CH₃)₂) would provide no significant effect on the steric hindrance for these relatively flat pyridine ligands. In line with this view, the θ_c of all the (*p*-cymene)RuCl₂(L_N) complexes and hence the edge energies of Cl in these complexes are quite similar.

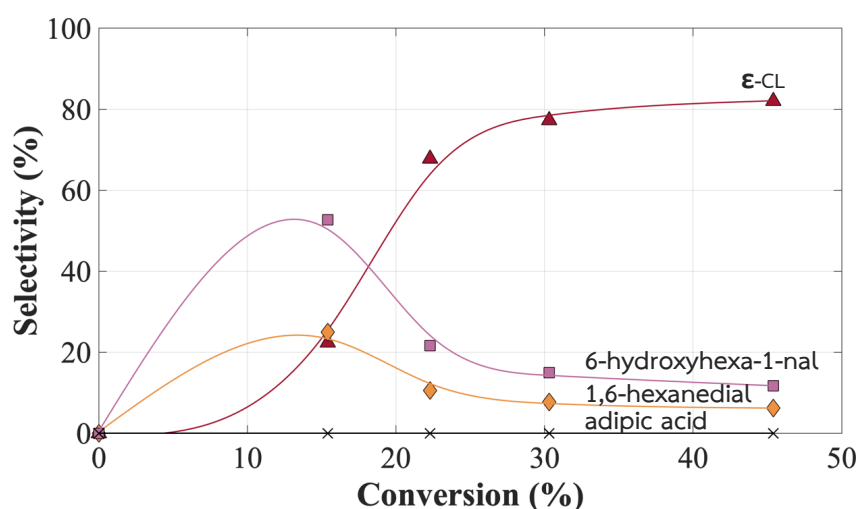


Figure 4.5 The relation between product selectivity and conversion (0.025 mmol (*p*-cymene)RuCl₂(L_{P4}), 1 mmol 1,6-HD, under N₂ atmosphere, 110 °C, 30 mL toluene, 0.2 mmol K₂CO₃, 8 mmol MIBK)

Despite the different L_P and L_N ligands, all catalysts provide similar selectivity for 6-hydroxyhexan-1-al ($\sim 36\%$) and for ϵ -CL ($\sim 64\%$) at 28% 1,6-HD conversion, extrapolated from the reaction profiles (**Table A3, Appendix A**). For example, the product selectivity over (*p*-cymene)RuCl₂(L_{P4}) depends only on the conversion, as shown in **Figure 4.5**. At low conversion, the selectivity of 6-hydroxyhexan-1-al was relatively high since it was a primary product, as proposed in **Scheme 4.2**. As the conversion increased, the ϵ -CL selectivity increased, while the primary product, 6-hydroxyhexan-1-al was consumed. As the product selectivity was the same and depends on the conversion for both L_P and L_N complexes, it is likely that these

catalysts promote 1,6-HD oxidation with a similar reaction pathway, that is, an associative interchange (I_a) mechanism.

It is essential to mention that upon performing the reactions under these conditions, using all the (*p*-cymene) $\text{RuCl}_2(\text{L}_P)$ and (*p*-cymene) $\text{RuCl}_2(\text{L}_N)$ catalysts, the 1,6-HD conversions never went beyond 50%. This limitation could result from i) deficiency of the hydrogen acceptor (MIBK) and/or ii) deactivation of the catalysts. However, in all the experiments, MIBK was added in excess (8 eq. as compared to 1,6-HD) and remained in large quantities after the reaction, as detected in the GC-chromatogram. Thus, the limitation of MIBK as a hydrogen acceptor might not be the case. To validate catalyst deactivation in a batch reaction, Apesguia's estimation method was applied [130, 131]. In this method, the relationship between the conversion vs. catalyst weight \times time (*i.e.*, resident time) would be independent of the amount of catalyst used. If the catalyst were deactivated, such a relationship would be decreasingly deviated, particularly when a small amount of catalyst was employed, as shown in **Figure 4.6**.

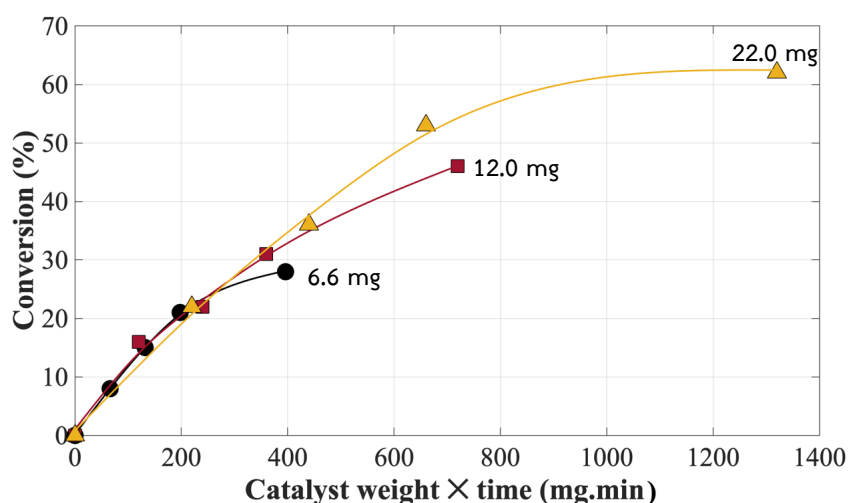


Figure 4.6 Apesguia's plot of 1,6-HD oxidation using different amounts of (*p*-cymene) $\text{RuCl}_2(\text{L}_{P4})$ catalyst (1 mmol 1,6-HD, under N_2 atmosphere, 110 °C, 30 mL toluene, 0.2 mmol K_2CO_3 , 8 mmol MIBK)

A similar relationship between conversion vs. catalyst weight \times time was initially observed for the reaction using different weights of catalysts. In other words, a similar conversion was obtained for the reaction using more catalyst with a shorter resident

time, as compared to that using less catalyst with a longer resident time, that is, the same catalyst weight \times time. This suggests that the catalyst remains active at the beginning of the reaction. However, at a higher catalyst weight \times time (>400 mg \cdot min), the reaction with a smaller amount of catalyst provides a relatively lower conversion. This indicates that, as the reaction progressed, the number of the active sites readily decreased with time. Hence, the reaction using small amounts of the catalyst remains active for a short resident time.

Table 4.5 Activity of (p-cymene)RuCl₂(L_{P4}) for 1,6-HD oxidation in various conditions^a

Entry	Base	1,6-HD (mmol)	ϵ -CL (mmol)	MIBC (mmol)	MIBK (mmol)	Conversion (%)	k_{app} ($\times 10^{-3}$ min ⁻¹)
1	K ₂ CO ₃	1	-	-	8	30	10.8
2	K ₂ CO ₃	1	1	-	8	30	10.2
3	K ₂ CO ₃	0.5	-	1	7	0	-
4	KOH	1	-	-	8	17	4.2
5	^t BuOK	1	-	-	8	20	3.7

^a (0.025 mmol Ru complex, under N₂ atmosphere, 110 °C, 30 mL toluene, 0.2 mmol base, 8 mmol MIBK, conversion after 30 min resident time).

The observed catalyst deactivation could be derived from i) thermal decomposition and/or ii) product adsorption. The thermal decomposition was ruled out because the UV-vis spectra of the (p-cymene)RuCl₂(L_{P4}) complex remained the same after treatment with K₂CO₃ in toluene at 110 °C for 1 h (Figure A12, Appendix A). Alternatively, ϵ -CL could be coordinated to the Ru center, inhibiting the association of the incoming 1,6-HD, which leads to the deactivation. To validate this assumption, the reaction was performed with a 1 : 1 mole ratio of 1,6-HD : ϵ -CL (Table 4.5, entry 2). The result showed that the conversions and k_{app} are similar to those without the ϵ -CL added (Table 4.5, entries 1-2, Figure A13 and A14 (Appendix A)). This suggests that the competitive association of ϵ -CL does not cause the deactivation; the catalysts could still promote the reaction even in the presence of equimolar ϵ -CL and 1,6-HD.

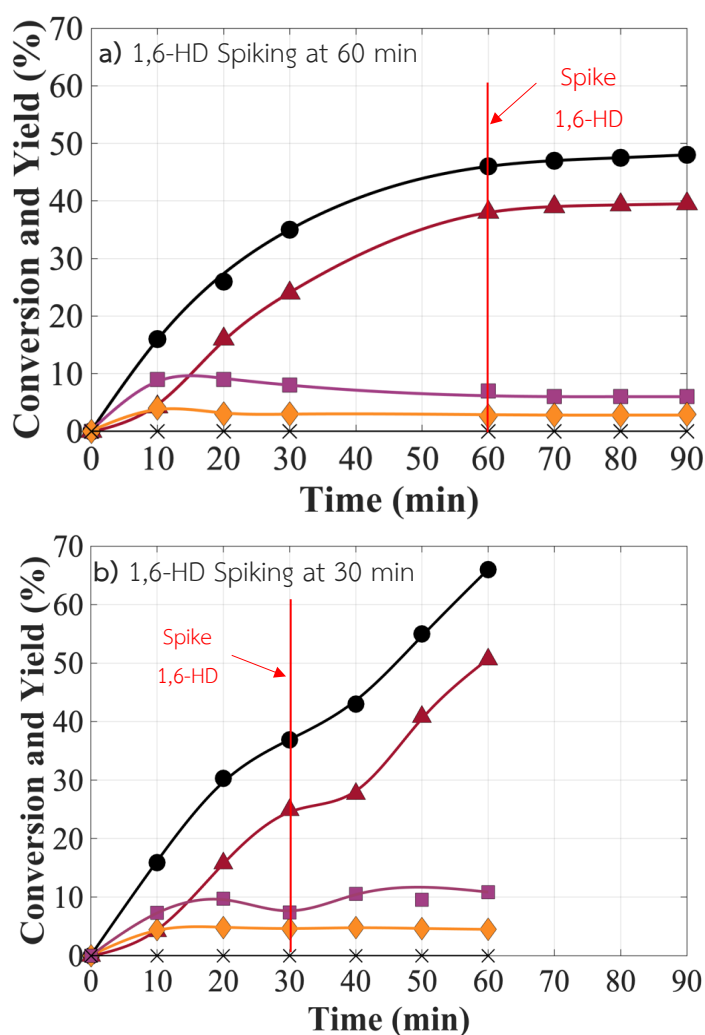


Figure 4.7 1,6-HD oxidation time profiles using the (*p*-cymene)Ru(L_{p4})Cl₂ catalyst with a) 0.5 mmol 1,6-HD spiking at 60 min and b) 0.5 mmol 1,6-HD spiking at 30 min (conversion (●), 6-hydroxyhexan-1-al (■), 1,6-hexanedial (◆), ϵ -CL (▲), and adipic acid (×) (0.025 mmol Ru complex, 1 mmol 1,6-HD, under N₂ atmosphere, 110 °C, 30 mL toluene, 0.2 mmol K₂CO₃, 8 mmol MIBK))

In addition to ϵ -CL, methyl isobutyl carbinol (MIBC) is produced as MIBK is hydrogenated (see **Scheme 4.2**). This MIBC could possibly interfere with the catalytic cycles since the secondary alcohol (MIBC) is more ready to react with Ru than the primary alcohol (1,6-HD). To verify the effect of MIBC, the reaction in the presence of MIBC was carried out using 1.0 mmol MIBC : 0.025 mmol Ru to mimic the amount of MIBC at the 50% conversion. Surprisingly, no catalytic activity was observed (**Table 4.5, entry 3**). In a similar manner, the spike of 1,6-HD into the reaction after the progress

of 50% conversion (at 1 h) inhibited the reaction from proceeding further, as shown in **Figure 4.7a**. This suggests that the oxidation of 1,6-HD was inhibited when MIBC was produced as much as ~40 times higher than the Ru catalysts. However, the catalyst remains active when the MIBC/Ru is less than ~25. It is deduced from the experiments in **Figure 4.7b** that the reaction can continuously proceed when 1,6-HD was spiked at 37% conversion. At this conversion level, the MIBC was produced at approximately 25 equivalences (0.6 mmol MIBC : 0.025 mmol Ru). This indicates that the MIBC : Ru mole ratio is essential to maintain the catalytic activity of the catalyst. It is likely that the MIBC could be competitive with the 1,6-HD to coordinate or react with the catalysts.

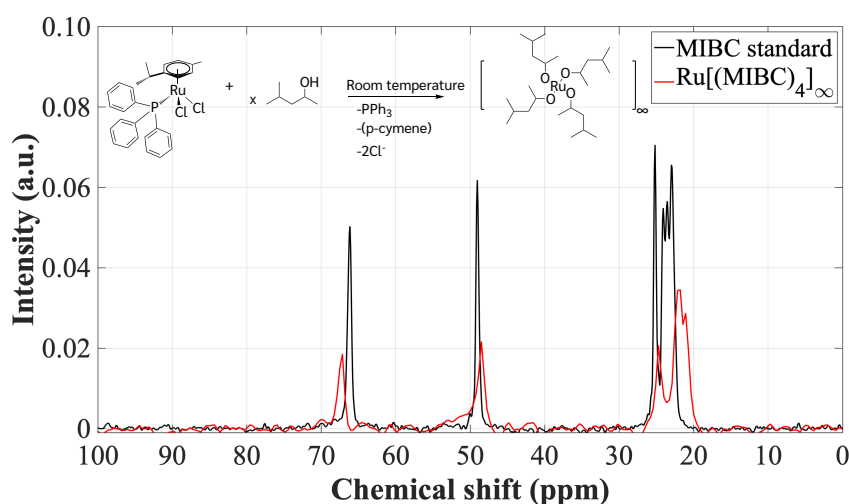


Figure 4.8 500 MHz ^{13}C -CPMAS NMR spectra of MIBC and $[\text{Ru}(\text{OMIBC})_4]_\infty$ complex

In a supporting manner, the brown solids were precipitated after mixing $(p\text{-cymene})\text{RuCl}_2(\text{L}_{\text{P}4})$ and MIBC (in excess) in toluene at room temperature without the base for 1 h. From **Figure 4.8**, the ^{13}C CPMAS NMR spectrum of the brown solid clearly shows characteristics of MIBC. This could be attributed to the Ru alkoxide species formed by the reaction of MIBC with the Ru complex. The LC-QTOF mass spectra and TGA analysis suggest that the brown precipitate would be $\text{Ru}(\text{OR})_4$ (**Figure A15, Appendix A**). The formation of inactive Ru alkoxide could result from the oxidative decomposition of L when an excessive amount of alkoxides, especially MIBC/ $t\text{BuOK}$, is present. Metal alkoxide formation by reaction between a metal complex and alcohol has also been reported in the literature, especially magnesium complexes [132, 133]. This side reaction readily causes deterioration of the catalyst's complex, particularly at high MIBC concentration, compared to Ru and the feed (1,6-HD). Accordingly, the

reaction is typically inhibited at ~50% conversion. In contrast, the Ru alkoxide does not readily form at 37% conversion. Hence, after adding 1,6-HD, the reaction is no longer limited, as observed previously. This is due to the higher 1,6-HD : MIBC ratio (>0.5) that prevents the side reaction between the Ru complex and MIBC.

Besides the MIBC that could react with the catalyst, the base type also affects the catalyst's stability. The use of KOH (pKa ~10.2) and ^tBuOK (pKa ~15.7) instead of K₂CO₃ (pKa ~17.0) reduces the reaction rate by approximately three-fold (from ~4.17 to ~3.68 × 10⁻³ min⁻¹, **Table 4.5**, and **Figure A13** and **A14 (Appendix A)**). Even though this reaction proceeds much faster in the presence of the base (K₂CO₃), as shown earlier, the addition of the stronger base possibly causes the side reaction with alcohol or hydroxide to form Ru alkoxide or hydroxide. In excess MIBC, the remaining [(*p*-cymene)RuCl₂(L_{p4})] complex is in the order of K₂CO₃ > KOH > ^tBuOK. This can be deduced from the decrease in L_{p4} and *p*-cymene signals of the complexes in **Figure 4.9**. The disappearance of these signals is due to the decomposition of (*p*-cymene)RuCl₂(L_{p4}) by MIBC in the presence of a strong base. The fact that the free triphenylphosphine ligand (~7–8 ppm) and *p*-cymene (~4.6 ppm) signals were not initially observed in **Figure 4.9**, especially with ^tBuOK, is presumably due to the precipitation upon the complex decomposition. It is likely that [(*p*-cymene)RuLClO^tBu]_x could be primarily precipitated and later decomposed to Ru(OMIC)₄, as evidenced in **Figure 4.8**.

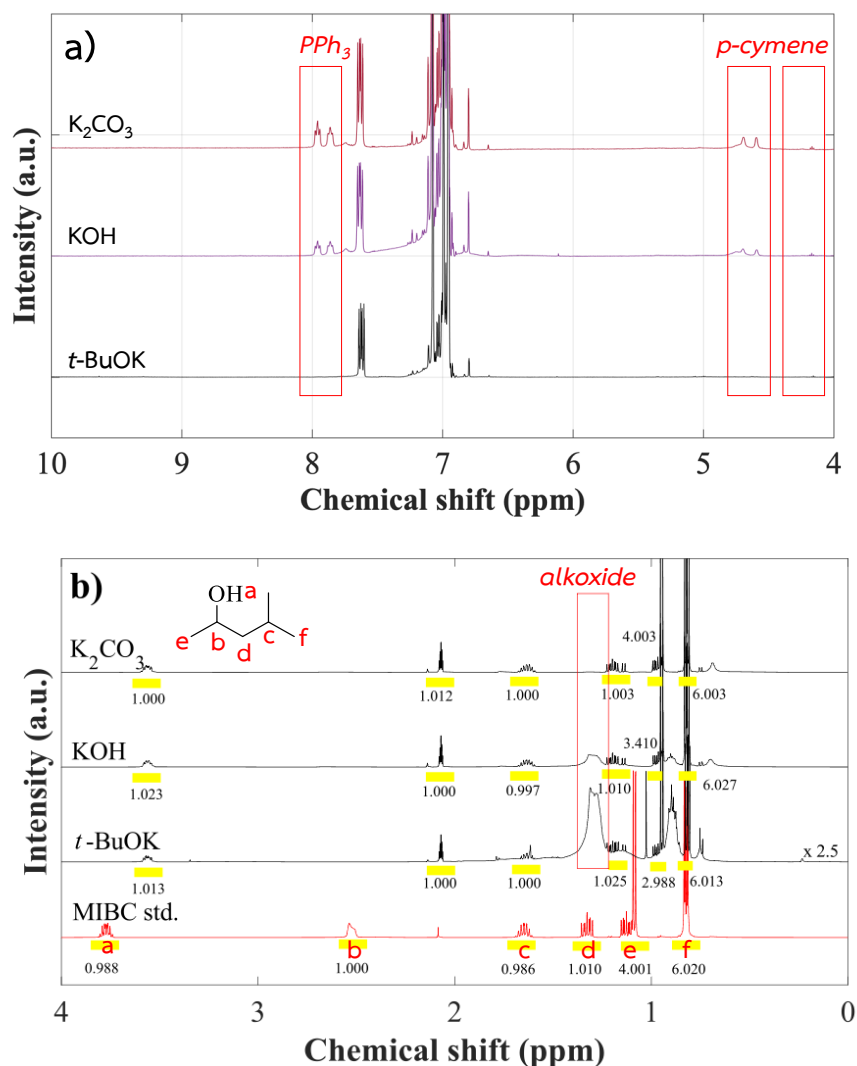


Figure 4.9 500 MHz ^1H NMR spectra of $(p\text{-cymene})\text{RuCl}_2(\text{L}_{\text{P}4})$ after the addition of 34 mmol MIBC at 110 °C for 5 min in toluene- d_8 ; a) 0–10 ppm and b) zoom 0–4 ppm

In a supportive manner, the free triphenylphosphine and p -cymene ligands were later evidenced for all samples, including that with t -BuOK, after leaving the reaction mixtures overnight (**Figure A16, Appendix A**). This indicates the dissolution of triphenylphosphine and p -cymene ligands after decomposition to $\text{Ru}(\text{OMIC})_4$. Accordingly, no triphenylphosphine and p -cymene signals were observed in the ^{13}C CPMAS NMR spectrum of the precipitate ($\text{Ru}(\text{OMIC})_4$). It has also been mentioned in the literature that the activity of ruthenium complexes for several alcohol oxidations depends on the bases [127]. However, they did not fully address the side reactions of the base since no kinetic studies were performed. Therefore, the base does not only

play a vital role in enhancing the catalytic activity but also affects the stability of the Ru complexes.

4.2 Acetylene/ethylene cross-metathesis over supported WO₃ catalysts

4.2.1 Physicochemical properties of WO₃/SiO₂ catalysts

The surface area and chemical composition of the supported tungsten oxide over silica are summarized in **Table 4.6**. The WO₃ loading in each catalyst is close to the expected values. All loaded WO₃ samples showed a lower surface area (365-248 m²·g⁻¹) than its parent support (385 m²·g⁻¹). The higher the WO₃ loading, the lower the surface area. This could be attributed to the loaded WO₃ could cover the surface of the SiO₂.

Table 4.6 Physical and Chemical properties of WO₃/SiO₂ catalysts

Entry	Samples	Specific surface area (m ² /g) ^a	WO ₃ (wt.%) ^b	Acidity (mmol/g) ^c	H ₂ -consumption (mmol/g) ^d	Reduction (%) ^e
1	2%WO ₃ /SiO ₂	365	2.54	4.0	0.265	81
2	3%WO ₃ /SiO ₂	349	3.42	5.9	0.427	96
3	5%WO ₃ /SiO ₂	328	5.10	6.1	0.731	102
4	7%WO ₃ /SiO ₂	248	7.43	6.5	0.247	26
5	SiO ₂	381	-	-	-	-

^a Multipoint BET ^b WD-XRF ^c Estimated from the integration of NH₃-TPD signal ^d Estimated from the integration of H₂-TPR signal ^e Calculated from H₂-consumption.

The crystallite WO₃ diffraction peaks were only observed in 7%WO₃/SiO₂, as shown in **Figure 4.10A (d)**, suggesting that bulk WO₃ was present in 7%WO₃/SiO₂. In a supportive manner, UV-VIS DRS spectra of the 7% WO₃/SiO₂ showed an absorption at 457 nm (**Figure 10B (d)**), representing the bulk WO₃ species as reported by Ross-Medgaarden *et al.* [134]. The band gap energy of these samples (~2.75 eV, **Table B1, Appendix B**) is also consistent with the bulk WO₃ (2.80 eV). In contrast, the lower absorption (230 and 350 nm, **Figure 4.10B (a-c)**, **Appendix B**) was observed for

2-5%WO₃/SiO₂, with higher band gap energy (4.5 and 5.2 eV, **Table B1**) that corresponds to the isolated WO₃ (*i.e.*, di-oxo and mono-oxo WO₃) or smaller WO₃ clusters (*i.e.*, dimeric WO₃ and WO₃ clusters). In line with this view, only Raman spectra of 7%WO₃/SiO₂ (**Figure 4.10C (d)**) showed the W=O vibrations of bulk WO₃ at 268 cm⁻¹ ($\delta(W=O)$, 711 ($\nu_{as}(W=O)$), and 804 cm⁻¹ ($\nu_s(W=O)$) [134]. Furthermore, W 5d ligand field splitting of an octahedral W unit could be observed in the 2nd derivative in situ TR-XANES spectra of 7%WO₃/SiO₂ (**Figure B1, Appendix B**). The W L₃-edge in situ TR-EXAFS spectra of 7%WO₃/SiO₂ (**Figure 4.10D**) also show the radial distance at 1.37 and 2.75 Å for W–O and W–O–W bond, corresponding to the bulk WO₃ species as reported by Kuzmin and Purans [135].

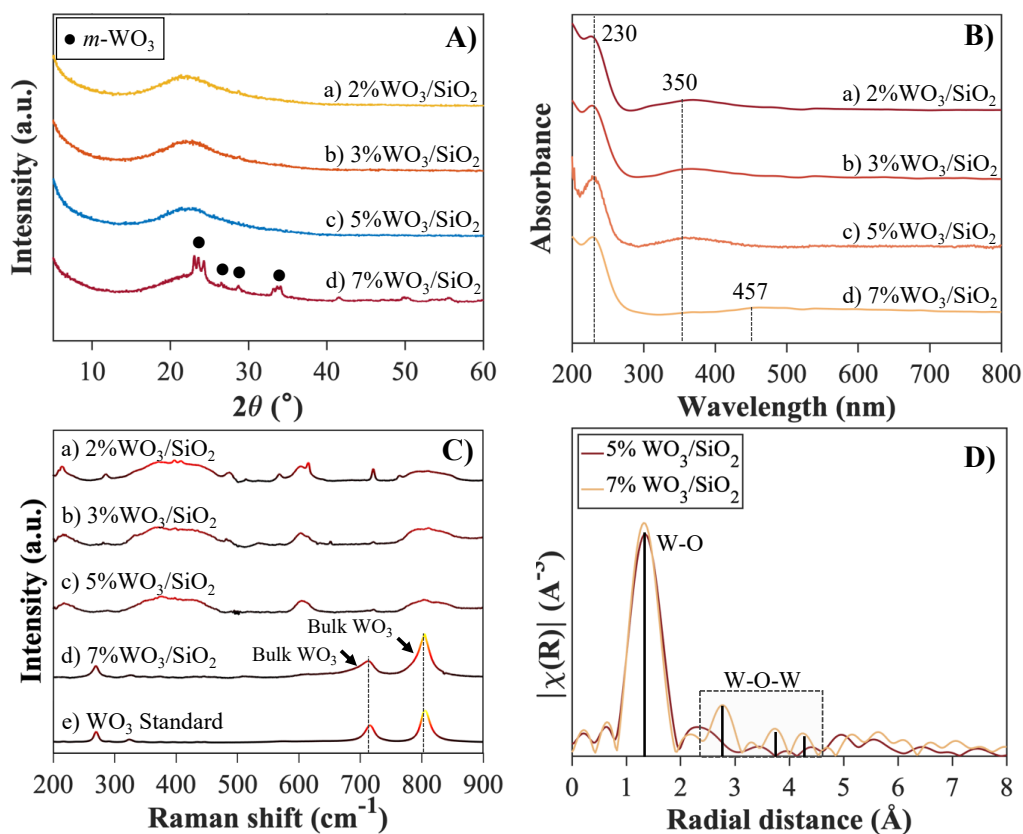


Figure 4.10 (A) XRD diffraction patterns, (B) UV-VIS DRS spectra, (C) Raman spectra, and (D) Fourier transform of W L₃-edge *in situ* EXAFS spectra at 500°C under air-zero of WO₃ over silica support

On the other hand, bulk WO₃ characteristic peak was not detected in the Raman spectra of 2%WO₃/SiO₂, 3% WO₃/SiO₂, and 5% WO₃/SiO₂ (**Figure 4.10 C (a-c)**). W L₃-edge *in situ* TR-XANES and the 2nd derivative spectra of 5% WO₃/SiO₂ also showed

a similar single asymmetrical peak of tetrahedral tungsten oxide in contrast to a doublet peak of octahedral W unit in 7% WO₃/SiO₂ and (NH₃)₆H₂W₁₂O₄₀ (**Figure B1, Appendix B**). Moreover, Fourier transforms of W L₃-edge in situ TR-EXAFS spectra of this sample show only 1st shell W–O coordination (**Figure 4.10D**). The Raman shifts at ~998, and 1025 cm⁻¹ for mono-oxo WO₃ species with four and five coordination (O=W(O–Si)₃ and O=W(O–Si)₄) were particularly pronounced in 2%WO₃/SiO₂ (**Figure 4.11a**). In addition, weak scattering peaks at 975 and 985 cm⁻¹ reveal the formation of WO₃ clusters and di-oxo WO₃ ((O=)₂W(O–Si)₂) [136-138], as shown in **Figure 4.11**. At the same time, the WO₃ cluster (975 cm⁻¹) was predominant in 3%WO₃/SiO₂ and 5%WO₃/SiO₂ samples.

The difference in WO₃ species, as evidenced by Raman spectroscopy, suggests that the formation of WO₃ depends on WO₃ loading compared to the available silanol on the surface of the supports. At a low WO₃ loading (2%WO₃/SiO₂), WO₃ tends to disperse in a monomeric form (di-oxo and mono-oxo WO₃). This is because the surface silanol is sufficiently available for anchoring WO₃ species. With a relatively strong interaction between the surface silanol and the tungsten precursors (*i.e.*, (NH₃)₆H₂W₁₂O₄₀) [139], agglomeration to bulk WO₃ is somewhat inhibited upon calcination. As the WO₃ loading increases, the tungsten precursor remains in closed proximity, weakening the interaction between the surface silanol and the WO₃. Accordingly, agglomeration to bulk WO₃ was observed, particularly for the 7%WO₃/SiO₂. Consequently, surface silanol of the support plays a significant role in accommodating monomeric WO₃, which would be the most active species for the acetylene/ethylene cross-metathesis [113].

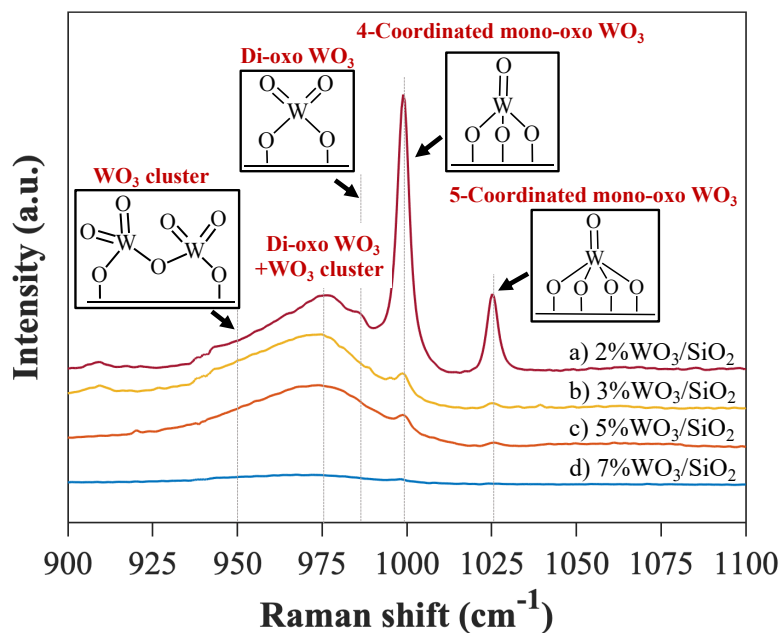


Figure 4.11 Raman spectra of various $\text{WO}_3/\text{silica}$ supports

4.2.2 Acetylene/ethylene cross-metathesis over WO_3/SiO_2 catalysts

Over the as-prepared 5% WO_3/SiO_2 , acetylene removal is gradually increased with time on stream, as seen in **Figure 4.12A (a)**. This suggests that the as-prepared WO_3 was not an active site but a catalyst precursor for acetylene/ethylene cross-metathesis. The hydrocarbon feed (ethylene or acetylene) would primarily react with the WO_3 during the reaction to form W^{4+} alkylidene species ($\text{W}=\text{CH}_2$) via pseudo-Wittig reaction (**Scheme 4.3**), as suggested in the literature [140]. The acetylene/ethylene metathesis over this W^{4+} alkylidene active site initially is proceeded by [2+2] cycloaddition of $\text{M}=\text{CH}_2$ (i) and acetylene, forming a four-membered metallocyclic intermediate (ii). Then, the ring-opening of intermediate (ii) would yield vinyl carbene tungsten intermediate (iii) that could undergo [2+2] cycloaddition with ethylene, forming a four-membered metallocyclic intermediate (iv). The rearrangement of the intermediate (iv) would result in 1,3-butadiene, recovering active $\text{W}=\text{CH}_2$ species (i) as shown in **Scheme 4.3**.

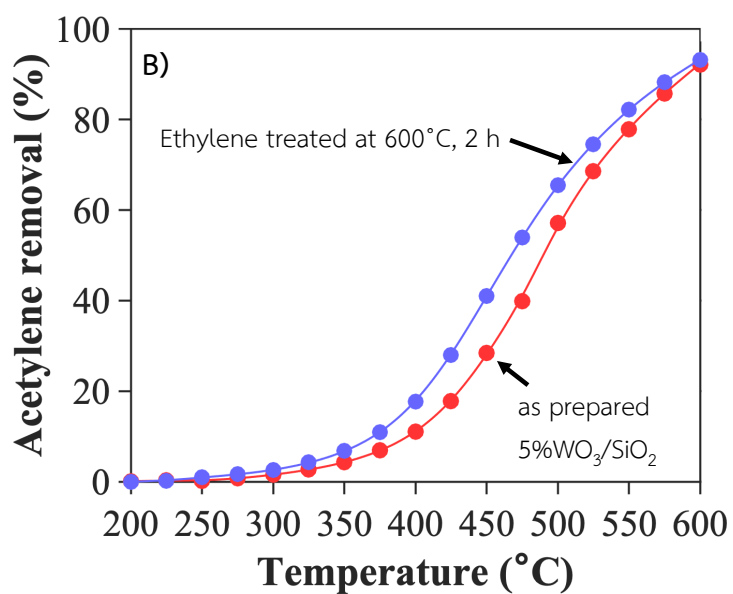
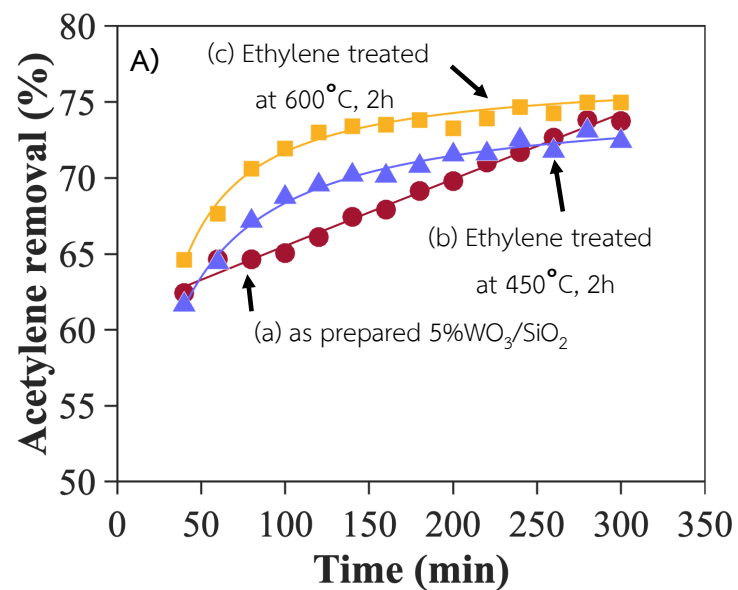
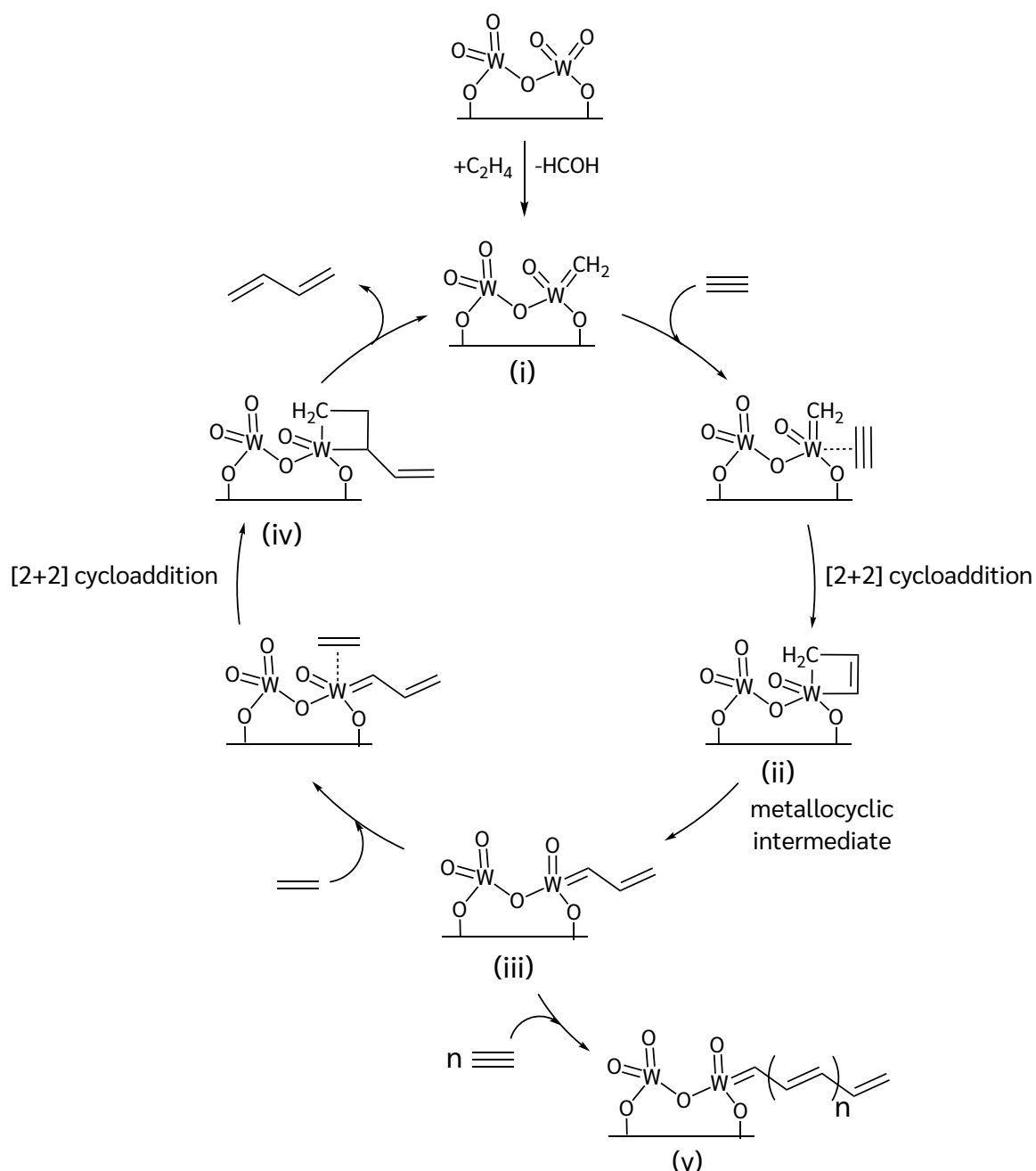


Figure 4.12 Effect of ethylene treatment on acetylene removal over 5%WO₃/SiO₂ (A) at 450 °C when catalyst was (a) untreated, (b) treated at 450 °C for 2 h and (c) treated at 600 °C for 2 h, and B) at 200-600 °C (feed flow rate 15 (for A) or 20 mL·min⁻¹ (for B), acetylene/ethylene = 1/99 wt.%, N₂ flow rate 35 mL·min⁻¹)



Scheme 4.3 W^{4+} alkylidene formation over 5% WO_3/SiO_2 during ethylene treatment and proposed mechanism of acetylene/ethylene cross metathesis

The acetylene removal rapidly increased after in situ treatment with ethylene at 450 °C for 2 h. Similarly, the ethylene treatment at 600 °C can readily improve the induction period, and a steady-state removal can be reached within 2 h. This indicates that ethylene treatment can primarily promote the formation of $W=CH_2$ species and consequently suppress the induction period [97]. Supportively, higher acetylene removal was obtained over the catalyst with ethylene-treating at 600 °C compared to

the prepared WO_3/SiO_2 (Figure 4.12B). At a similar conversion, the ethylene-treated WO_3/SiO_2 requires ~ 25 °C lower than the as-prepared WO_3/SiO_2 . According to the temperature profile, the reaction temperature of 450 °C was applied for selective acetylene removal throughout this work.

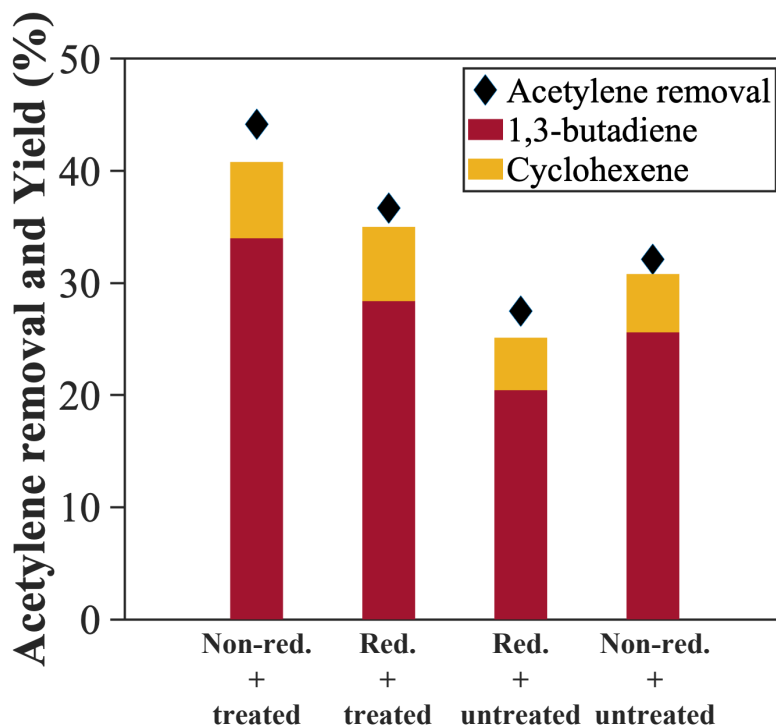


Figure 4.13 Acetylene/ethylene cross-metathesis over non-reduced and reduced 5% WO_3/SiO_2 with/without ethylene treatment (feed flow rate 15 $\text{mL}\cdot\text{min}^{-1}$ (acetylene/ethylene = 1/99 wt.%), N_2 flow rate 35 $\text{mL}\cdot\text{min}^{-1}$, 450 °C)

As an active $\text{W}=\text{CH}_2$ must be generated from $\text{W}=\text{O}$ species, a concentration of surface $\text{W}=\text{O}$ would determine the catalytic activity. Accordingly, the 5% WO_3/SiO_2 reduced at 500 °C for 2 h before treatment with ethylene at 600 °C provides a lower acetylene removal (37%) compared to the non-reduced catalyst (44%, Figure 4.13). The reduced 5% WO_3/SiO_2 without ethylene treatment even showed lower activity than those without reduced. This can be explained by a reduction of surface $\text{W}=\text{O}$ as seen from the hydrogen consumption at ~ 450 °C in the H_2 -TPR profile (Figure 4.14A).

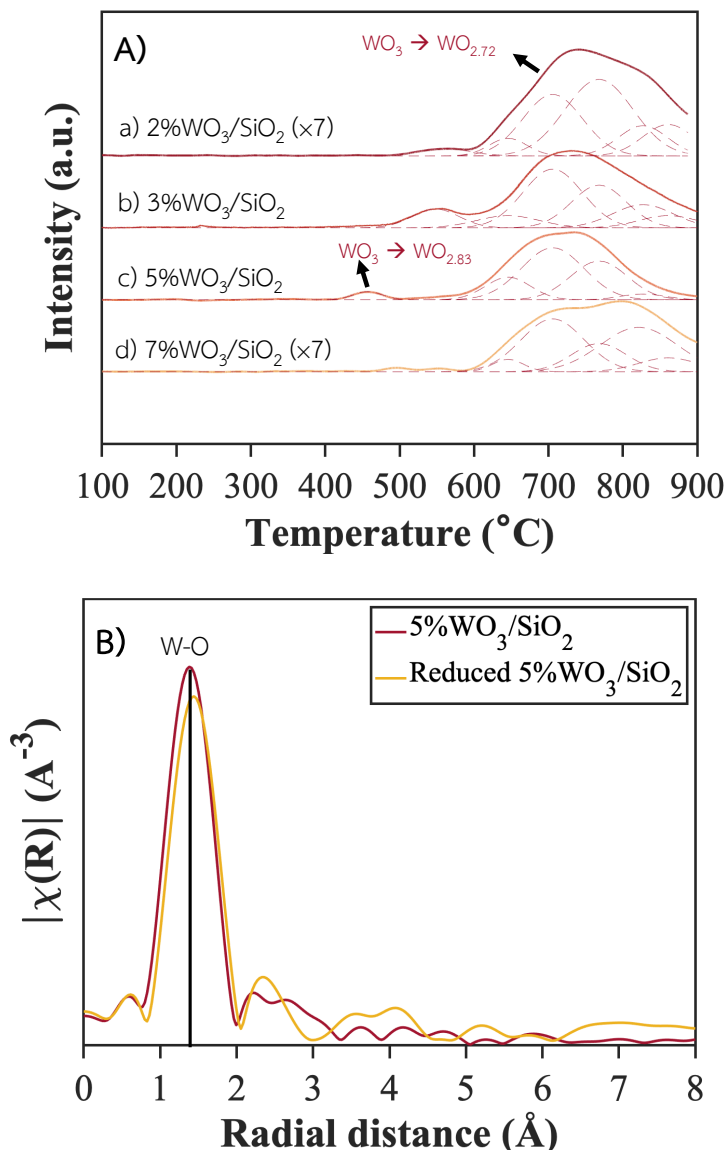
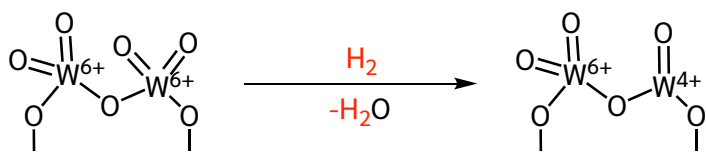


Figure 4.14 (A) H₂-TPR of WO₃ supported SiO₂ and (A) and Fourier transform of W L₃-edge *in situ* TR-EXAFS spectra of calcined and reduced under H₂ at 500 °C for 30 min of 5%WO₃/SiO₂

In line with this view, the average oxidation state of WO₃ species in 5%WO₃/SiO₂ decreased from +6.0 to +5.3 (Table B2, entries 1–2, Appendix B) after reduction at 500 °C. These values were estimated from W L₃-edge energy using WO₃ (W⁶⁺), (NH₄)₆H₂W₁₂O₄₀ (W⁶⁺), and W foil (W⁰) standards, as shown in Figure B2 (Appendix B). Jiang *et al.* [141] have also mentioned that, upon H₂ reduction, the oxo group at the oxygen-terminated surface was readily removed as water, leading to a lower concentration of surface W=O (the active site precursor) with a decrease in average W oxidation state (a combination of W⁶⁺ and W⁴⁺ species), as proposed in Scheme 4.4.



Scheme 4.4 Reduction of WO_3 over $5\%\text{WO}_3/\text{SiO}_2$

Table 4.7 Fitting parameters for the first coordination shell of $5\%\text{WO}_3/\text{SiO}_2$, reduced $5\%\text{WO}_3/\text{SiO}_2$, $5\%\text{WO}_3/\text{MCM-41}$ and $5\%\text{WO}_3/\text{SBA-15}$ W L_3 -edge *in situ* TR-EXAFS spectra at $500\text{ }^\circ\text{C}$ under air-zero

Entry	Samples	Shell	C.N.	S_0^2	σ^2 (\AA^2)	e_0	ΔR	R (\AA)	R-factor (%)
1	$5\%\text{WO}_3/\text{SiO}_2$	W-O	4.0	0.86	0.0107	4.9	-0.150	1.78	2.4
2	reduced $5\%\text{WO}_3/\text{SiO}_2$	W-O	3.7	0.86	0.0097	14.3	-0.070	1.86	3.0
3	$5\%\text{WO}_3/\text{MCM-41}$	W-O	4.0	0.86	0.0106	13.1	0.019	1.82	1.1
4	$5\%\text{WO}_3/\text{SBA-15}$	W-O	4.0	0.86	0.0105	15.4	0.019	1.83	0.7

C.N., σ^2 , and R stand for coordination number, Debye-waller factor, and bond length, respectively.

WO_3 and W_2O_7 were used as the standard for fitting.

In a supportive manner, W L_3 -edge *in situ* Time-Resolved EXAFS spectra (*in situ* TR-EXAFS) for the reduced $5\%\text{WO}_3/\text{SiO}_2$ at $500\text{ }^\circ\text{C}$ also evidenced a decrease in W=O first shell intensity, as shown in **Figure 14B**. This again suggested that the reduction of WO_3 leads to lower oxygen coordination around tungsten (from 4.0 to 3.7, **Table 4.7, entry 2, Figure B3, Appendix B**). In line with this view, Wilken *et al.* report that a few amounts of WO_3 can be partially reduced to form $\text{WO}_{2.90}$ [142]. A decrease in surface W=O concentration would result in a decreased activity but not selectivity. This is because the remaining W=O can be transformed to active W=CH₂ sites, promoting acetylene removal via acetylene/ethylene cross-metathesis with a similar 1,3-butadiene selectivity for both reduced and non-reduced catalysts.

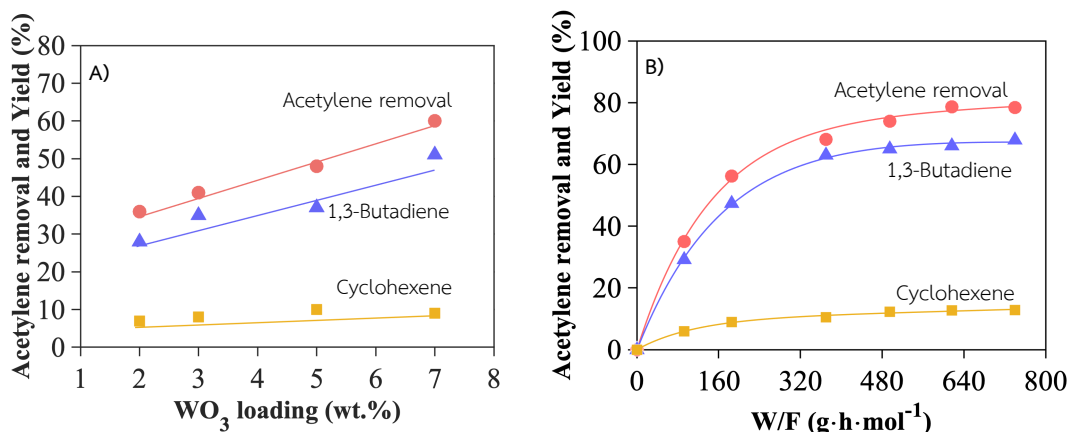
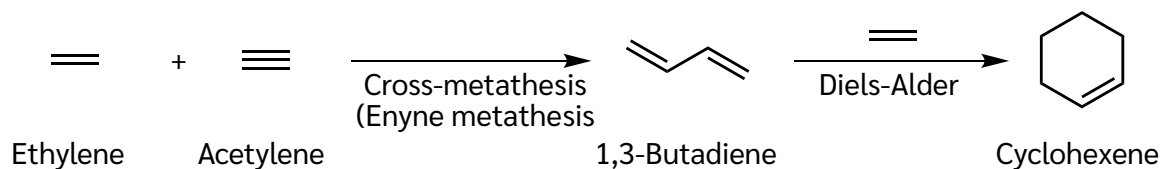


Figure 4.15 Effect of A) WO_3 loading and B) W/F plot of acetylene/ethylene cross-metathesis over $2\%\text{WO}_3/\text{SiO}_2$; (●) conversion, (▲) 1,3-butadiene, (■) cyclohexene, (feed flow rate $20\text{ mL}\cdot\text{min}^{-1}$ (acetylene/ethylene = $1/99$ wt.%), N_2 flow rate $35\text{ mL}\cdot\text{min}^{-1}$, $450\text{ }^\circ\text{C}$, activation in ethylene at $600\text{ }^\circ\text{C}$ for 2 h)

As the surface $\text{W}=\text{O}$ is required to form active $\text{W}=\text{CH}_2$, the acetylene removal was linearly enhanced with WO_3 loading, as shown in **Figure 4.15A**. 1,3-butadiene was also increasingly produced as a major product (78-85% selectivity). At the same time, cyclohexene was a secondary product emerging from Diels-Alder of ethylene and the 1,3-butadiene primarily produced (**Scheme 4.4**) [143, 144]. It is likely that, in excess of ethylene, the 1,3-butadiene formed on the surface may well react with ethylene before desorption. For the same reason, high ethylene coverage results in the dimerization of 1-butene and 2-butene, as detected in trace amounts [145, 146]. The acetylene removal was also raised with W/F, as presented in **Figure 4.15B**. 1,3-butadiene yield was increased to a greater extent, up to ~68%, while cyclohexene was steadily produced to ~12% yield. The reaction pathway for acetylene removal via acetylene/ethylene cross-metathesis over $5\%\text{WO}_3/\text{SiO}_2$ is present in **Scheme 4.4**.



Scheme 4.4 Acetylene/ethylene cross-metathesis and Diels-Alder reaction.

Despite a linear relation between activity and WO_3 loading, the turn-over-frequency (TOF) was decreased with WO_3 loading, as shown in **Table 4.8**. This suggests that relatively less active W species are present at the high WO_3 loading. As 7% WO_3/SiO_2 contained mainly bulk WO_3 (as discussed earlier in **Figure 4.10**), the decrease in TOF at high WO_3 loadings could be attributed to the presence of this species that has been previously observed by Wang *et al.* [147]. This is because the bulk WO_3 crystallites possess a relatively less external surface, leading to low W=O species - an active site precursor for acetylene/ethylene cross-metathesis. The lower W=O species were also reported for bulk WO_3 compared to highly dispersed WO_3 on the silica support [148-151].

Table 4.8 Acetylene removal via acetylene/ethylene cross-metathesis over WO_3 over silica support

Entry	Catalysts	TOF (h^{-1})	Acetylene removal (%) ^o	Yield (%) ^o		Selectivity (%) ^o	
				1,3-Butadiene	Cyclohexene	1,3-Butadiene	Cyclohexene
1	2% WO_3/SiO_2	53	36	28	7	78	25
2	3% WO_3/SiO_2	45	41	33	8	80	23
3	5% WO_3/SiO_2	35	48	37	10	77	28
4	7% WO_3/SiO_2	30	60	51	9	85	18

Feed flow rate 20 $\text{mL}\cdot\text{min}^{-1}$ (acetylene/ethylene = 1/99 wt.%), N_2 flow rate 35 $\text{mL}\cdot\text{min}^{-1}$, 450 °C, activation in ethylene at 600 °C for 2 h. ^oEvaluated at 300 min on stream.

On the other hand, the catalyst with low WO_3 loading, particularly 2% WO_3/SiO_2 , provides TOF up to 53 h^{-1} . No bulk WO_3 was observed in this catalyst, while the monomeric WO_3 , e.g., mono and di-oxo WO_3 , were mainly present, as shown in **Figure 4.11**. This suggests that such single-site WO_3 is more active than the bulk species, presumably due to a higher dispersion. While the 3% WO_3/SiO_2 and 5% WO_3/SiO_2 exhibit TOF lower than 2% WO_3/SiO_2 . This is because these catalysts contain mainly WO_3 clusters with a relatively small amount of monomeric WO_3 , as discussed earlier (**Figure 4.11**).

Despite high dispersion, the monomeric WO_3 species (found primarily on 2% WO_3/SiO_2) appears to be more active than the WO_3 clusters (mainly found in 3% and 5% WO_3/SiO_2). This is because the monomeric WO_3 possessed relatively high

electron density around the fermi level attributed to O-2p electrons and W-5d electrons [152-155]. In line with this view, a lower average W oxidation state of +5.6 was observed in 2%WO₃/SiO₂ when compared to +6.0 of the WO₃ cluster in 5%WO₃/SiO₂ (**Table B2, entries 1 and 3, Appendix B**). Such high electron density may facilitate the formation of W=CH₂ species that promotes overall [2+2] cycloaddition for the acetylene/ethylene cross-metathesis. In sharp contrast, the lower electron density of WO₃ species in 5% WO₃/SiO₂ and 7%WO₃/SiO₂ (average W oxidation state of +6.0 and +6.3, **Table B2, entries 1 and 4, Appendix B**) would destabilize the W=CH₂ species, resulting in a decreased reaction rate. In a similar manner, [4+2] cycloaddition (Diels-Alder) activity would also decrease, leading to low cyclohexene selectivity (~18% selectivity) over 7%WO₃/SiO₂, as compared to those over the 2%-5%WO₃/SiO₂ (23-25% selectivity).

4.2.3 Effect of supports on WO₃/W=CH₂ species

In addition to the WO₃ loading, the formation of active single-site WO₃ depends on the interaction between WO₃ and the silica support. As the surface silanol acts as an anchoring site for WO₃, a higher number of silanol could readily accommodate the single-site WO₃, the most active species, as discussed previously. For this reason, increasing WO₃ support interaction and anchoring sites would favor the supports with surface Al-OH. Accordingly, 5%WO₃/NaY and 5%WO₃/NaX were examined to compare with 5%WO₃/SiO₂ (in which only the WO₃ cluster is formed). It can be seen from **Figure 4.16A(a)** that bulk WO₃ was the only species formed over 5%WO₃/NaY, while the WO₃ cluster was formed over 5%WO₃/NaX (**Figure 4.16A (b)**). Despite similar surface area for both supports (**Table 4.5, entries 1 and 2**), a higher Al-OH density in 5%WO₃/NaX probably provides proper site proximity, accommodating smaller WO₃ species as seen by DR-UV (**Figure B4A, Appendix B**). This indicates that Al-OH over NaY and NaX could play a role in anchoring WO₃. The strong interaction between WO₃ and Al-OH was also observed in H₂-TPR, as shown in **Figure B4B (Appendix B)**.

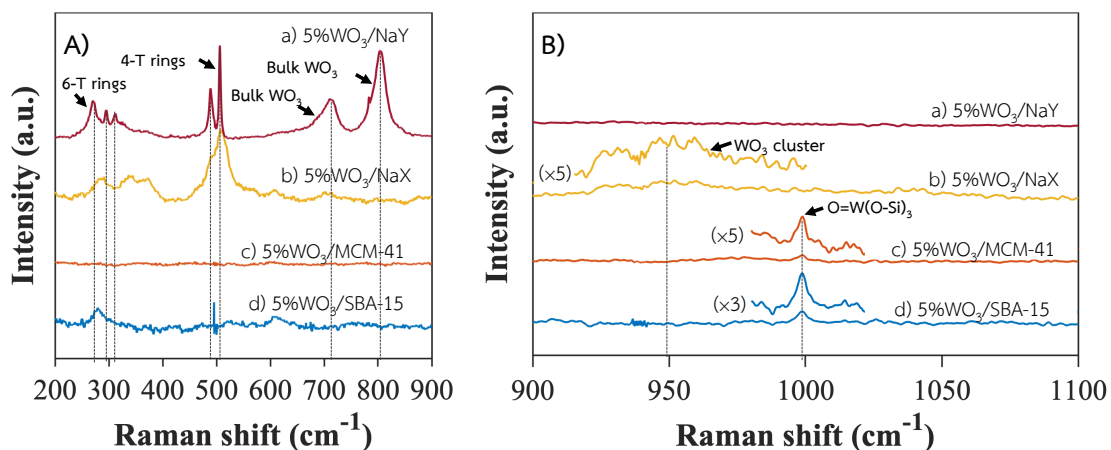


Figure 4.16 Raman spectra of WO_3 over siliceous support in the range of A) 200-900 cm^{-1} and B) 900-1100 cm^{-1}

However, 5% WO_3/NaY provides a lower acetylene removal and TOF (25 h^{-1} , Table 4.9, entry 1) compared to 5% WO_3/SiO_2 (35 h^{-1} , Table 4.6, entry 3). As mentioned earlier, this is presumably because of the less active WO_3 (bulk) formation. Moreover, an exposed Al-OH in this support would result in higher strength acid sites (Table 4.9, entry 1-2, Figure B5, Appendix B). This can readily promote acetylene/ethylene oligomerization and coke formation, which rapidly deactivates the catalyst, as evidenced by the TGA result (Figure B6, Appendix B). Maksasithorn *et al.* reported that the NaOH-treated acid site mitigation of WO_3/SiO_2 can suppress coke formation [156]. In a supportive manner, 5% WO_3/NaX , Al-OH rich support, shows no activity for acetylene/ethylene cross-metathesis (Table 4.10 entry 2), despite a more active WO_3 cluster being present in this catalyst.

Table 4.9 Physical and chemical properties of WO_3 over confined supports

Entry	Samples	Total surface (m^2/g)	External surface (m^2/g) ^b	Pore Volume (mL/g) ^b	WO_3 Loading (wt.%) ^c	Acidity (mmol/g) ^d	H_2 -consumption (mmol/g) ^e	Reduction (%) ^f
1	5% WO_3/NaY	555 (696) ^a	35 (58) ^a	0.26 (0.35) ^a	5.13	28.6	0.379	57
2	5% WO_3/NaX	561 (660) ^a	38 (63) ^a	0.30 (0.40) ^a	5.66	79.6	0.254	35
3	5% $\text{WO}_3/\text{MCM-41}$	365 (1076) ^a	53 (143) ^a	0.37 (0.61) ^a	5.40	7.3	0.726	103
4	5% $\text{WO}_3/\text{SBA-15}$	571 (967) ^a	37 (156) ^a	0.46 (0.93) ^a	5.06	6.7	0.596	91

^a Parent support ^b BJH method ^c WD-XRF ^d Estimated from the integration of NH_3 -TPD signal ^e Estimated from the integration of H_2 -TPR signal ^f Calculated from H_2 -consumption.

Table 4.10 Acetylene/ethylene cross-metathesis over WO₃ supported on various confined supports

Entry	Catalysts	TOF (h ⁻¹)	Acetylene removal (%) ^a	Yield (%) ^a		Selectivity (%) ^a	
				1,3-Butadiene	Cyclohexene	1,3-Butadiene	Cyclohexene
1	5%WO ₃ /NaY	25	35	30	5	86	14
2	5%WO ₃ /NaX	0	0	0	0	0	0
3	5%WO ₃ /MCM-41	40	58	49	8	85	14
4	5%WO ₃ /SBA-15	46	62	53	9	85	16

Feed flow rate 20 mL·min⁻¹ (acetylene/ethylene = 1/99 wt.%), N₂ flow rate 35 mL·min⁻¹, 450 °C, ethylene treatment at 600 °C for 2 h. ^a Evaluated at 300 min.

In sharp contrast, low-acidic supports (none of Al–OH) with higher surface area and hexagonal pore structure, namely 5%WO₃/MCM-41 and 5%WO₃/SBA-15, provides higher acetylene removal (58% and 62%, **Table 4.10 entry 3-4**) and stability (**Figure B7, Appendix B**). 1,3-butadiene selectivity was also slightly enhanced (85%), and very low selectivity of cyclohexene was observed (14%) (**Table 4.10, entry 3**). This is because these supports possess a relatively high surface area (**Table 4.9, entries 4-5**) compared to the typical silica support. Moreover, the isolated silanol within the confined hexagonal mesoporous SiO₂ would be favorable for anchoring WO₃ species, presumably due to an increase in the three-dimensional local hydrogen bond density [157]. Accordingly, various types of monomeric WO₃ species (**Figure 4.11**) would be dispersed in 5% WO₃/MCM-41 and 5%WO₃/SBA-15, leading to a high amount of exposed W=CH₂ active site on the surface for acetylene/ethylene cross-metathesis.

The formation of such highly dispersed WO₃ in 5%WO₃/MCM-41% and 5%WO₃/SBA-15 was evidenced by the peak of mono-oxo WO₃ species with four coordination (O=W(O–Si)₃) at 998 cm⁻¹ in Raman spectra (**Figure 4.16B (c) and (d)**) [158-160], similar to that found in 2%WO₃/SiO₂ (**Figure 4.11**). Gao *et al.* suggested that the O=W(O–Si)₃ with a strongly bound W–O–Si covalent bond can be observed over meso-cellular silica foam [148]. Yang *et al.* also reported that O–W(O–Si)₃ can be formed over SBA-15 [148]. In addition, in situ TR-XANES of 5%WO₃/MCM-41% and 5%WO₃/SBA-15 shows the W L₃-edge energy of 10208.9 eV and average W oxidation state of +5.3 (**Table B2, entries 7 and 8, Appendix B**), consistent to W⁵⁺ in the O–W(O–Si)₃. In a supportive manner, in situ TR-EXAFS fitting exhibits the WO₃ species

with a coordination number (CN) of 4 for both 5%WO₃/MCM-41% and 5%WO₃/SBA-15 (Table 4.7, entries 3 and 4, and Figure B9 (Appendix B)).

The lower W L₃-edge energy and average W oxidation state (+5.3) were observed for 5%WO₃/MCM-41% and 5%WO₃/SBA-15, as compared to 2%WO₃/SiO₂. This is because the additional W⁶⁺ species, i. e., O=W⁶⁺(O-Si)₄ and (O=)₂W⁶⁺(O-Si)₂, were present in 2%WO₃/SiO₂, providing the average W oxidation state of +5.6. Accordingly, the mono-oxo WO₃ species with four coordination (O=W(O-Si)₃) would mainly exist in these confined silica supports. In a supportive manner, the O=W⁶⁺(O-Si)₄ and (O=)₂W⁶⁺(O-Si)₂ species were not detected by the Raman spectra (Figure 4.11 and 4.16B).

When 5%WO₃/MCM-41 and 5%WO₃/SBA-15 were treated with 1-hexene at 600 °C, the formation of W=CH₂ active sites from the O=W(O-Si)₃ species during the olefin treatment can be evidenced by a sudden red shift (within 5 min) in the W edge energy (~0.4 eV, Table 4.11). This suggests the rapid reduction of W=O species to W=CH₂ species by “pseudo-Wittig” reaction with 1-hexene, as discussed previously in Section 4.2.1. This is because these catalysts possess high surface silanols that promote the formation of W=CH₂ species. Handzlik *et al.* also reported that the silanol group adjacent to WO₃ could assist in the activation of the mono-oxo Mo(IV) species to form W=CH₂ species in which it is more kinetically accessible than those non-OH-assisted mechanisms [113]. Accordingly, the catalysts with O=W(O-Si)₃ species would provide a higher amount of the exposed W=CH₂ active site on the surface. While, for the WO₃ clusters in 5%WO₃/SiO₂, there might be some unreactive tungsten species that remained on the surface after contacting with 1-hexene. This could be supported by a slightly higher average W oxidation state of +4.3 for 5%WO₃/SiO₂, compared to that of +4.1 for 5%WO₃/SBA-15 and 5%WO₃/MCM-41. It is worth noting that the tetrahedral structure of these W species was retained during 1-hexene treatment at 600 °C for 1 h, as deduced from a similar 2nd derivative W L₃-edge TR-XANES spectra (Figure B10, Appendix B).

Table 4.11 W L₃-edge energy and average W oxidation state of all samples at 500 °C under air-zero and after 1-hexene treatment at 600 °C for 5 min

Catalysts	Calcined at 500 °C		Treated at 600 °C with 1-hexene at 5 min		Edge Shift (eV)
	Energy edge	Average	Energy edge	Average	
	(eV)	oxidation state	(eV)	oxidation state	
5%WO ₃ /MCM-41	10208.9	5.3	10208.5	4.1	-0.4
5%WO ₃ /SBA-15	10208.9	5.3	10208.5	4.1	-0.4
5%WO ₃ /SiO ₂	10209.2	6.0	10208.6	4.3	-0.6

Although the electronic state and local structure of the active W=CH₂ was somewhat similar for 5%WO₃/MCM-41 and 5%WO₃/SBA-15, as compared to 5%WO₃/SiO₂, Fourier transforms W L₃-edge *in situ* TR-EXAFS spectra suggest the formation of only isolated W=CH₂ site for 5%WO₃/MCM-41% and 5%WO₃/SBA-15, as shown in **Figure 4.17A** and **4.17B**.

Despite a similar first shell radial distance for W–O and W–C coordination [136], no higher coordination shell (3-4 and 6-8 Å) can be observed over 5%WO₃/MCM-41 and 5%WO₃/SBA-15. This implies the formation of single-site W=CH₂ species (CH₂=W(O–Si)₃) after treating with 1-hexene at 600 °C. In addition, the relative intensity of first shell W–C (or W–O) scattering (**Figure 4.18A**) remains constant during the treatment for 1 h, indicating a high stability of such single-site W=CH₂ species in 5%WO₃/MCM-41 and 5%WO₃/SBA-15. This isolated and stable W=CH₂ single site could promote a rapid [2+2] cycloaddition and higher acetylene removal and be responsible for the observed high activity of these catalysts.

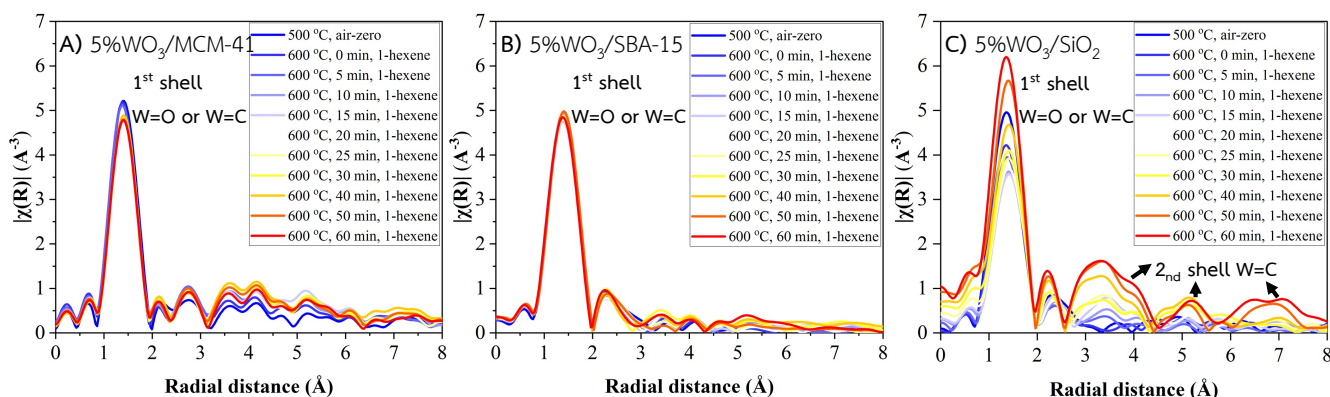


Figure 4.17 Fourier transform of W L_3 -edge *in situ* TR-EXAFS spectra with 1-hexene activation over A) 5%WO₃/MCM-41, B) 5%WO₃/SBA-15, and C) 5%WO₃/SiO₂

In a different manner, a higher coordination W–C shell (3–4 and 6–8 Å) can be observed in 5%WO₃/SiO₂ (**Figure 4.17C**). This again suggests that the W=CH₂ species generated from the WO₃ cluster (in 5%WO₃/SiO₂) exist in close proximity, compared to that generated from mono-oxo WO₃ (in 5%WO₃/MCM-41 and 5%WO₃/SBA-15). This probably promotes the oligomerization of higher olefins, as reported by Spamer *et al.* [161]. In fact, the TGA result under air-zero of 5%WO₃/SiO₂ after ethylene treatment shows a higher carbon content than 5% WO₃/MCM-41 and 5%WO₃/SBA-15 (**Figure B11, Appendix B**). In line with this view, the relative intensity of second shell scattering (presumably W–C) keeps increasing after treatment with 1-hexene (**Figure 4.18B**). The formation of coke deposits in close proximity to the W=CH₂ active site would limit accessibility and hence activity of 5%WO₃/SiO₂, as compared to 5% WO₃/MCM-41 and 5%WO₃/SBA-15.

One could expect that the pore size may affect the catalytic performance other than the WO₃ species present in the catalysts. This is not the case for this study since the rate of metathesis is considerably fast, and the reaction is thermodynamically controlled. Moreover, the acetylene/ethylene metathesis is not shape-selective. Kinetic diameters of both reactants and products are relatively small (<0.4 nm) as compared to the pore size of SBA-15 and MCM-41 (3–50 nm). There would be no external and/or internal diffusion limitation for this reaction. Accordingly, the pore size of SBA-15 and MCM-41 investigated shall not affect the observed intrinsic rate.

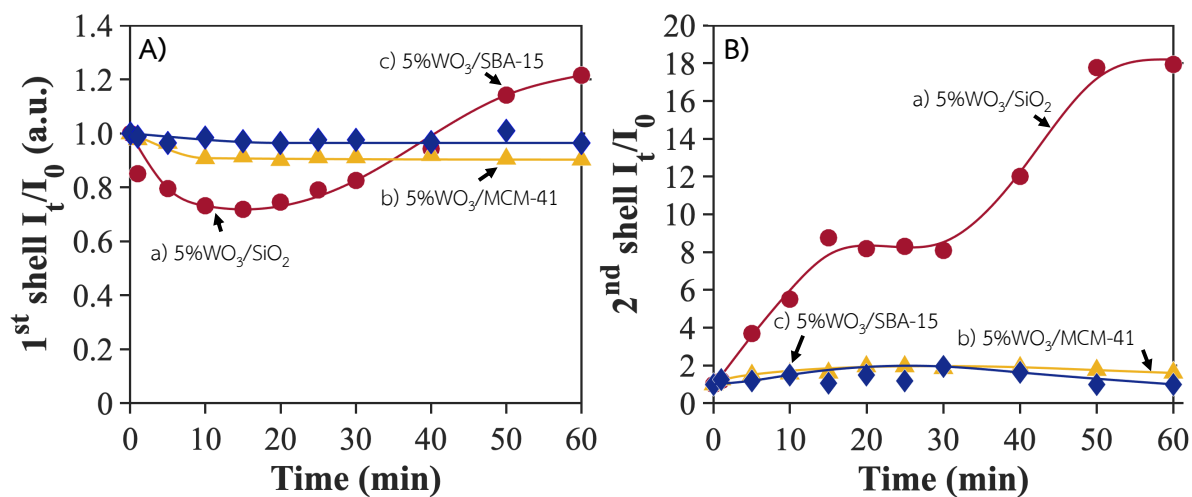


Figure 4.18 A) a ratio of 1st shell intensity and B) a ratio of 2nd shell intensity under 1-hexene activation to calcined catalysts (I_t/I_0)

CHAPTER 5

Conclusions and suggestions

5.1 Conclusions

ϵ -Caprolactone (ϵ -CL) can be successfully produced from 1,6-HD oxidation using (*p*-cymene)RuCl₂(L) complexes as catalysts and MIBK as a hydrogen acceptor in non-polar media. The catalytic activity of (*p*-cymene)RuCl₂(L_p) complexes is mainly governed by the geometrical effect derived from a pocket-site dimension (θ_c). As the increases θ_c only from 140° to 145°, the reaction rate constant (k_{app}) increases by 100 orders of magnitude, despite the same electron density of Ru in the complexes. This experimental evidence suggests that the reaction may involve an associative interchange (I_a) mechanism, as previously suggested by computational studies. No effect of θ_c on catalytic activity is observed for the (*p*-cymene)RuCl₂(L_N) complexes, presumably due to their readily accessible pocket-site dimension ($\theta_c > 145^\circ$). The ϵ -CL selectivity depends only on the 1,6-HD conversion for both L_p and L_N complexes. The catalytic reaction is limited by methyl isobutyl carbinol (MIBC), a hydrogenated form of MIBK produced during the reaction. Especially at MIBC:1,6-HD ≥ 2 , MIBC competitively reacts with the ruthenium complex, forming inactive Ru(OR)₄. In addition, bases (^tBuOK and KOH) stronger than K₂CO₃ cause deterioration of the catalyst.

Acetylene removal from ethylene-rich feed can be achieved by acetylene/ethylene cross-metathesis using WO₃-supported catalysts. Ethylene treatment can activate WO₃ to W=CH₂, an active site for the acetylene/ethylene cross-metathesis. 1,3-butadiene was produced as a major product (78% selectivity) together with minor product cyclohexene (14% selectivity) from the Diels-Alder reaction between 1,3-butadiene and ethylene. The hydrogen treatment of WO₃ leads to a decrease in W=O and WO₃ agglomeration, resulting in a declined acetylene removal activity. The mono-oxo and di-oxo WO₃ species formed in 2%WO₃/SiO₂ provide a higher rate of acetylene removal (53 h⁻¹) compared to the WO₃ cluster (45 h⁻¹, for 3-5%WO₃/SiO₂) and bulk WO₃ (30 h⁻¹, for 7%WO₃/SiO₂). Though the framework Al acts as an anchoring site for higher WO₃ dispersion, 5%WO₃/NaX and 5%WO₃/NaY give lower acetylene removal due to coke formation from the acid sites during ethylene treatment. For the confined siliceous supports, the mono-oxo WO₃ species

with four coordination ($\text{CH}_2=\text{W}(\text{O}-\text{Si})_3$) in 5% $\text{WO}_3/\text{MCM-41}$ and 5% $\text{WO}_3/\text{SBA-15}$ provides relatively higher activity (40 and 46 h^{-1}) compared to the WO_3 cluster in 5% WO_3/SiO_2 . Although a similar electronic property of $\text{W}=\text{CH}_2$ species (average W oxidation state of +4.2) formed from both the mono-oxo WO_3 and WO_3 cluster, an isolated and stable $\text{W}=\text{CH}_2$ species generated from the mono-oxo WO_3 readily promotes [2+2] cycloaddition for acetylene/ethylene cross-metathesis. In addition, the coke formation is less pronounced over the isolated $\text{W}=\text{CH}_2$ species than that generated from the WO_3 cluster. The findings could lend an alternative approach for ethylene purification simply by adding a supported WO_3 catalytic bed at the cracker exit.

5.2 Suggestions

5.2.1 It was very useful that the crystal structure of Ru complexes was studied in liquid phase XAS experiment.

5.2.2 To define the precise oxidation of each WO_3 species, *in situ* ethylene treatment XPS analysis was very interesting.

5.2.3 Due to the formation of WO_3 species was varied by atmosphere and condition, the experiment of WO_3 treating under air, H_2 and water, and *in situ* technique were fascinating.

5.2.4 It was very attractive to obtain highly dispersed WO_3 species using a tungsten complexes.

References

- [1] D.H. Kwan, I. Constantinescu, R. Chapanian, M.A. Higgins, M.P. Kötzler, E. Samain, A.B. Boraston, J.N. Kizhakkedathu, S.G. Withers, Toward Efficient Enzymes for the Generation of Universal Blood through Structure-Guided Directed Evolution, *Journal of the American Chemical Society*, 137 (2015) 5695-5705.
- [2] H. Cui, L. Zhang, L. Eltoukhy, Q. Jiang, S.K. Korkunç, K.-E. Jaeger, U. Schwaneberg, M.D. Davari, Enzyme Hydration Determines Resistance in Organic Cosolvents, *ACS Catalysis*, 10 (2020) 14847-14856.
- [3] S. Singh, R. Anand, Tunnel Architectures in Enzyme Systems that Transport Gaseous Substrates, *ACS Omega*, 6 (2021) 33274-33283.
- [4] J. Fernández-Lucas, New Insights on Enzyme Stabilization for Industrial Biocatalysis, *ACS Sustainable Chemistry & Engineering*, 9 (2021) 15073-15074.
- [5] N. Sofeo, J.H. Hart, B. Butler, D.J. Oliver, M.D. Yandea-Nelson, B.J. Nikolau, Altering the Substrate Specificity of Acetyl-CoA Synthetase by Rational Mutagenesis of the Carboxylate Binding Pocket, *ACS Synthetic Biology*, 8 (2019) 1325-1336.
- [6] T. Joshi, B. Graham, L. Spiccia, Macrocyclic Metal Complexes for Metalloenzyme Mimicry and Sensor Development, *Accounts of Chemical Research*, 48 (2015) 2366-2379.
- [7] X. Li, C. Fu, L. Luo, J. Ge, Design of enzyme-metal hybrid catalysts for organic synthesis, *Cell Reports Physical Science*, 3 (2022) 100742.
- [8] L. Hamilton Gregory, J. Kang Eun, M. Mba, F.D. Toste, A Powerful Chiral Counterion Strategy for Asymmetric Transition Metal Catalysis, *Science*, 317 (2007) 496-499.
- [9] J. Xie, Y. Zheng, J.Y. Ying, Protein-Directed Synthesis of Highly Fluorescent Gold Nanoclusters, *Journal of the American Chemical Society*, 131 (2009) 888-889.
- [10] J.T. Payne, P.H. Butkovich, Y. Gu, K.N. Kunze, H.J. Park, D.-S. Wang, J.C. Lewis, Enantioselective Desymmetrization of Methylenedianilines via Enzyme-Catalyzed Remote Halogenation, *Journal of the American Chemical Society*, 140 (2018) 546-549.
- [11] M. Kwiatkowska, J. Błaszczuk, L. Sieroń, P. Kielbasiński, Enzymatic Approach to the Synthesis of Enantiomerically Pure Hydroxy Derivatives of 1,3,5-Triaza-7-phosphaadamantane, *The Journal of Organic Chemistry*, 86 (2021) 8556-8562.

- [12] D.W. Cho, J.A. Latham, H.J. Park, U.C. Yoon, P. Langan, D. Dunaway-Mariano, P.S. Mariano, Regioselectivity of Enzymatic and Photochemical Single Electron Transfer Promoted Carbon–Carbon Bond Fragmentation Reactions of Tetrameric Lignin Model Compounds, *The Journal of Organic Chemistry*, 76 (2011) 2840-2852.
- [13] A.J.E. Borg, K. Beerens, M. Pfeiffer, T. Desmet, B. Nidetzky, Stereo-electronic control of reaction selectivity in short-chain dehydrogenases: Decarboxylation, epimerization, and dehydration, *Current Opinion in Chemical Biology*, 61 (2021) 43-52.
- [14] E. Rubio, A. Fernandez-Mayorales, A.M. Klivanov, Effect of the solvent on enzyme regioselectivity, *Journal of the American Chemical Society*, 113 (1991) 695-696.
- [15] H. Lechner, N. Ferruz, B. Höcker, Strategies for designing non-natural enzymes and binders, *Current Opinion in Chemical Biology*, 47 (2018) 67-76.
- [16] J.D. Tyzack, N. Furnham, I. Sillitoe, C.M. Orengo, J.M. Thornton, Understanding enzyme function evolution from a computational perspective, *Current Opinion in Structural Biology*, 47 (2017) 131-139.
- [17] A.J. Valentine, L.J. Taylor, A.M. Geer, C.D. Huke, K.E. Wood, W. Tovey, W. Lewis, S.P. Argent, A.M. Teale, J. McMaster, D.L. Kays, Structural and Electronic Studies of Substituted m-Terphenyl Group 12 Complexes, *Organometallics*, 41 (2022) 1426-1433.
- [18] M. Farzan, S.M. Elahi, H. Salehi, M.R. Abolhassani, An investigation of electronic and optical properties of InN nanosheet by first principle study, *Optics Communications*, 395 (2017) 293-300.
- [19] Y. Tian, S. Zhu, Y. Di, H. Liu, H. Yao, Y. Zhang, S. Guan, HOMO-controlled donor-acceptor contained polyimide for nonvolatile resistive memory device, *Dyes and Pigments*, 186 (2021) 109020.
- [20] A. Shimizu, Y. Ishizaki, S. Horiuchi, T. Hirose, K. Matsuda, H. Sato, J.-i. Yoshida, HOMO–LUMO Energy-Gap Tuning of π -Conjugated Zwitterions Composed of Electron-Donating Anion and Electron-Accepting Cation, *The Journal of Organic Chemistry*, 86 (2021) 770-781.
- [21] L.H. Nguyen, A Computational Study of the Electronic Properties of Heterocirculenes: Oxiflowers and Sulflowers, *ACS Omega*, 6 (2021) 30085-30092.

- [22] C.J. Yoo, W.J. Dong, J.Y. Park, J.W. Lim, S. Kim, K.S. Choi, F.O. Odongo Ngome, S.-Y. Choi, J.-L. Lee, Compositional and Geometrical Effects of Bimetallic Cu–Sn Catalysts on Selective Electrochemical CO₂ Reduction to CO, *ACS Applied Energy Materials*, 3 (2020) 4466-4473.
- [23] T. Chen, L. Ye, T.W.B. Lo, Designing the electronic and geometric structures of single-atom and nanocluster catalysts, *Journal of Materials Chemistry A*, 9 (2021) 18773-18784.
- [24] T. Chen, Q. Xue, K.C. Leung, B.T.W. Lo, Recent Advances of Precise Cu Nanoclusters in Microporous Materials, *Chemistry – An Asian Journal*, 15 (2020) 1819-1828.
- [25] X. Li, J. Wu, C. He, Q. Meng, C. Duan, Asymmetric Catalysis within the Chiral Confined Space of Metal-Organic Architectures, *Small*, 15 (2019) e1804770.
- [26] T. Buntara, S. Noel, P.H. Phua, I. Melian-Cabrera, J.G. de Vries, H.J. Heeres, Caprolactam from renewable resources: catalytic conversion of 5-hydroxymethylfurfural into caprolactone, *Angewandte Chemie International Edition in English*, 50 (2011) 7083-7087.
- [27] M. Ito, A. Osaku, A. Shiibashi, T. Ikariya, An Efficient Oxidative Lactonization of 1,4-Diols Catalyzed by Cp*Ru(PN) Complexes, *Organic Letters*, 9 (2007) 1821-1824.
- [28] J.W.H. W. A. Lazier, W. J. Amend., Hexametallene glycol, *Organic Syntheses*, 19 (1939) 48.
- [29] P. Werle, M. Morawietz, S. Lundmark, K. Sørensen, E. Karvinen, J. Lehtonen, Alcohols, Polyhydric, **Ullmann's Encyclopedia of Industrial Chemistry**, 2008.
- [30] M.T. Nunez, V.S. Martin, Efficient oxidation of phenyl groups to carboxylic acids with ruthenium tetroxide. A simple synthesis of (R)-gamma-caprolactone, the pheromone of *Trogoderma granarium*, *The Journal of Organic Chemistry*, 55 (1990) 1928-1932.
- [31] W.W.N. Thomas H. Parliment, Irving S. Fagerson, Delta-Caprolactone in Heated Milk Fat, *Journal of Dairy Science*, 48 (1965) 615-616.
- [32] H. Köpnick, M. Schmidt, W. Brüggling, J. Rüter, W. Kaminsky, Polyesters, **Ullmann's Encyclopedia of Industrial Chemistry**, 2000.
- [33] K. Miltenberger, Hydroxycarboxylic Acids, Aliphatic, **Ullmann's Encyclopedia of Industrial Chemistry**, 2000.
- [34] K. Sato, M. Aoki, R. Noyori, A "Green" Route to Adipic Acid: Direct Oxidation of Cyclohexenes with 30 Percent Hydrogen Peroxide, *Science*, 281 (1998) 1646-1647.

- [35] M.T. Musser, Adipic acid, Wiley-VCH Verlag GmbH & Co. KGaA2000.
- [36] S. Paterson, Alcohol Oxidation Reaction, Effects and Applications, **Nova Science Publishers**, Inc., New York, 2018.
- [37] S.E.C. Ned A. Porter, Karen A. Mills, Mechanisms of Free Radical Oxidation of Unsaturated Lipids, *Lipids*, 30 (1995) 277-290.
- [38] J. Liu, A. Guethmundsson, J.E. Backvall, Efficient Aerobic Oxidation of Organic Molecules by Multistep Electron Transfer, *Angewandte Chemie International Edition in English*, 60 (2021) 15686-15704.
- [39] M.N. Kopylovich, A.P.C. Ribeiro, E.C.B.A. Alegria, N.M.R. Martins, L.M.D.R.S. Martins, A.J.L. Pombeiro, Catalytic Oxidation of Alcohols (2015) 91-174.
- [40] V. Thaore, D. Chadwick, N. Shah, Sustainable production of chemical intermediates for nylon manufacture: A techno-economic analysis for renewable production of caprolactone, *Chemical Engineering Research and Design*, 135 (2018) 140-152.
- [41] V.S.T. Srinivasamurthy, D. Böttcher, J. Engel, S. Kara, U.T. Bornscheuer, A whole-cell process for the production of ϵ -caprolactone in aqueous media, *Process Biochemistry*, 88 (2020) 22-30.
- [42] A. Talebi, S. Labbaf, F. Karimzadeh, A conductive film of chitosan-polycaprolactone-polypyrrole with potential in heart patch application, *Polymer Testing*, 75 (2019) 254-261.
- [43] A. Shahin-Shamsabadi, A. Hashemi, M. Tahriri, F. Bastami, M. Salehi, F. Mashhadi Abbas, Mechanical, material, and biological study of a PCL/bioactive glass bone scaffold: Importance of viscoelasticity, *Materials Science and Engineering: C*, 90 (2018) 280-288.
- [44] L.R. Jaidev, S. Kumar, K. Chatterjee, Multi-biofunctional polymer graphene composite for bone tissue regeneration that elutes copper ions to impart angiogenic, osteogenic and bactericidal properties, *Colloids and Surfaces B: Biointerfaces*, 159 (2017) 293-302.
- [45] B. Nayak, G.M. Balachander, S. Manjunath, A. Rangarajan, K. Chatterjee, Tissue mimetic 3D scaffold for breast tumor-derived organoid culture toward personalized chemotherapy, *Colloids and Surfaces B: Biointerfaces*, 180 (2019) 334-343.

- [46] L.R. Mugwagwa, A.F.A. Chimphango, Enhancing the functional properties of acetylated hemicellulose films for active food packaging using acetylated nanocellulose reinforcement and polycaprolactone coating, *Food Packaging and Shelf Life*, 24 (2020) 100481.
- [47] W. Lin, Y. Ni, J. Pang, Size effect-inspired fabrication of konjac glucomannan /polycaprolactone fiber films for antibacterial food packaging, *International Journal of Biological Macromolecules*, 149 (2020) 853-860.
- [48] S. Khalid, L. Yu, M. Feng, L. Meng, Y. Bai, A. Ali, H. Liu, L. Chen, Development and characterization of biodegradable antimicrobial packaging films based on polycaprolactone, starch and pomegranate rind hybrids, *Food Packaging and Shelf Life*, 18 (2018) 71-79.
- [49] S. Alix, A. Mahieu, C. Terrie, J. Soulestin, E. Gerault, M.G.J. Feuilleley, R. Gattin, V. Edon, T. Ait-Younes, N. Leblanc, Active pseudo-multilayered films from polycaprolactone and starch based matrix for food-packaging applications, *European Polymer Journal*, 49 (2013) 1234-1242.
- [50] E. Sogut, A.C. Seydim, The effects of chitosan- and polycaprolactone-based bilayer films incorporated with grape seed extract and nanocellulose on the quality of chicken breast fillets, *LWT*, 101 (2019) 799-805.
- [51] E. Yan, J. Jiang, X. Yang, L. Fan, Y. Wang, Q. An, Z. Zhang, B. Lu, D. Wang, D. Zhang, pH-sensitive core-shell electrospun nanofibers based on polyvinyl alcohol/polycaprolactone as a potential drug delivery system for the chemotherapy against cervical cancer, *Journal of Drug Delivery Science and Technology*, 55 (2020) 101455.
- [52] L. Youssouf, A. Bhaw-Luximon, N. Diotel, A. Catan, P. Giraud, F. Gimié, D. Koshel, S. Casale, S. Bénard, V. Meneyrol, L. Lallemand, O. Meilhac, C. Lefebvre D'Hellencourt, D. Jhurry, J. Couprie, Enhanced effects of curcumin encapsulated in polycaprolactone-grafted oligocarrageenan nanomicelles, a novel nanoparticle drug delivery system, *Carbohydrate Polymers*, 217 (2019) 35-45.
- [53] M. Handa, A. Sharma, R.K. Verma, R. Shukla, Polycaprolactone based nano-carrier for co-administration of moxifloxacin and rutin and its In-vitro evaluation for sepsis, *Journal of Drug Delivery Science and Technology*, 54 (2019) 101286.

- [54] I. Kanungo, N. Chellappa, N.N. Fathima, Microfabrication of gelatin–polycaprolactone composites for customized drug delivery, *Materials Science and Engineering: C*, 49 (2015) 597-603.
- [55] X. Tang, J. Wei, N. Ding, Y. Sun, X. Zeng, L. Hu, S. Liu, T. Lei, L. Lin, Chemoselective hydrogenation of biomass derived 5-hydroxymethylfurfural to diols: Key intermediates for sustainable chemicals, materials and fuels, *Renewable and Sustainable Energy Reviews*, 77 (2017) 287-296.
- [56] L. Hu, L. Lin, Z. Wu, S. Zhou, S. Liu, Recent advances in catalytic transformation of biomass-derived 5-hydroxymethylfurfural into the innovative fuels and chemicals, *Renewable and Sustainable Energy Reviews*, 74 (2017) 230-257.
- [57] L.-H. Tang, F. Wu, H. Lin, A.-Q. Jia, Q.-F. Zhang, Synthesis, structure and catalytic alcohol oxidation by ruthenium(III) supported by Schiff base and triphenylphosphine ligands, *Inorganica Chimica Acta*, 477 (2018) 212-218.
- [58] J.M. Gichumbi, H.B. Friedrich, B. Omondi, Synthesis and characterization of some new half-sandwich ruthenium(II) complexes with bidentate N,N'-ligands and their application in alcohol oxidation, *Inorganica Chimica Acta*, 456 (2017) 55-63.
- [59] V.V. Costa, M.J. Jacinto, L.M. Rossi, R. Landers, E.V. Gusevskaya, Aerobic oxidation of monoterpenic alcohols catalyzed by ruthenium hydroxide supported on silica-coated magnetic nanoparticles, *Journal of Catalysis*, 282 (2011) 209-214.
- [60] R. Cang, B. Lu, X. Li, R. Niu, J. Zhao, Q. Cai, Iron-chloride ionic liquid immobilized on SBA-15 for solvent-free oxidation of benzyl alcohol to benzaldehyde with H₂O₂, *Chemical Engineering Science*, 137 (2015) 268-275.
- [61] H. Amanollahi, G. Moussavi, S. Giannakis, VUV/Fe(II)/H₂O₂ as a novel integrated process for advanced oxidation of methyl tert-butyl ether (MTBE) in water at neutral pH: Process intensification and mechanistic aspects, *Water Research*, 166 (2019) 115061.
- [62] P. Zhou, J. Zhang, Z. Xiong, Y. Liu, X. Huo, X. Cheng, W. Li, F. Cheng, Y. Zhang, C60 Fullerol promoted Fe(III)/H₂O₂ Fenton oxidation: Role of photosensitive Fe(III)-Fullerol complex, *Applied Catalysis B: Environmental*, 265 (2020) 118264.
- [63] I. Karthikeyan, S.K. Alamsetti, G. Sekar, Isolation and Characterization of a Trinuclear Cobalt Complex Containing Trigonal-Prismatic Cobalt in Secondary Alcohol Aerobic Oxidation, *Organometallics*, 33 (2014) 1665-1671.

- [64] L. Chen, J. Ding, J. Jia, R. Ran, C. Zhang, X. Song, Cobalt-Doped MnO₂ Nanofibers for Enhanced Propane Oxidation, *ACS Applied Nano Materials*, 2 (2019) 4417-4426.
- [65] Y. Li, D. Nakashima, Y. Ichihashi, S. Nishiyama, S. Tsuruya, Promotion Effect of Alkali Metal Added to Impregnated Cobalt Catalysts in the Gas-Phase Catalytic Oxidation of Benzyl Alcohol, *Industrial & Engineering Chemistry Research*, 43 (2004) 6021-6026.
- [66] M. Ghosh, Y.L.K. Nikhil, B.B. Dhar, S. Sen Gupta, Mechanism of Alcohol Oxidation by FeV(O) at Room Temperature, *Inorganic Chemistry*, 54 (2015) 11792-11798.
- [67] S.D. McCann, S.S. Stahl, Mechanism of Copper/Azodicarboxylate-Catalyzed Aerobic Alcohol Oxidation: Evidence for Uncooperative Catalysis, *Journal of the American Chemical Society*, 138 (2016) 199-206.
- [68] C. Aliende, M. Pérez-Manrique, F.A. Jalón, B.R. Manzano, A.M. Rodríguez, G. Espino, Arene Ruthenium Complexes as Versatile Catalysts in Water in both Transfer Hydrogenation of Ketones and Oxidation of Alcohols. Selective Deuterium Labeling of rac-1-Phenylethanol, *Organometallics*, 31 (2012) 6106-6123.
- [69] T. Naota, H. Takaya, S.-I. Murahashi, Ruthenium-Catalyzed Reactions for Organic Synthesis, *Chemical Reviews*, 98 (1998) 2599-2660.
- [70] M.L.S. Almeida, M. Beller, G.-Z. Wang, J.-E. Bäckvall, Ruthenium(II)-Catalyzed Oppenauer-Type Oxidation of Secondary Alcohols, *Chemistry – A European Journal*, 2 (1996) 1533-1536.
- [71] J.D. Blakemore, R.H. Crabtree, G.W. Brudvig, Molecular Catalysts for Water Oxidation, *Chemical Reviews*, 115 (2015) 12974-13005.
- [72] T. Buntara, S. Noel, P.H. Phua, I. Melián-Cabrera, J.G. de Vries, H.J. Heeres, Caprolactam from Renewable Resources: Catalytic Conversion of 5-Hydroxymethylfurfural into Caprolactone, *Angewandte Chemie International Edition*, 50 (2011) 7083-7087.
- [73] M.C. Warner, J.-E. Bäckvall, Mechanistic Aspects on Cyclopentadienylruthenium Complexes in Catalytic Racemization of Alcohols, *Accounts of Chemical Research*, 46 (2013) 2545-2555.

- [74] C. Hou, Z. Zhang, C. Zhao, Z. Ke, DFT Study of Acceptorless Alcohol Dehydrogenation Mediated by Ruthenium Pincer Complexes: Ligand Tautomerization Governing Metal Ligand Cooperation, *Inorganic Chemistry*, 55 (2016) 6539-6551.
- [75] C. Shan, X. Luo, X. Qi, S. Liu, Y. Li, Y. Lan, Mechanism of Ruthenium-Catalyzed Direct Arylation of C–H Bonds in Aromatic Amides: A Computational Study, *Organometallics*, 35 (2016) 1440-1445.
- [76] S. Manzini, J.A. Fernández-Salas, S.P. Nolan, From a Decomposition Product to an Efficient and Versatile Catalyst: The $[\text{Ru}(\eta^5\text{-indenyl})(\text{PPh}_3)_2\text{Cl}]$ Story, *Accounts of Chemical Research*, 47 (2014) 3089-3101.
- [77] J.S.M. Samec, J.-E. Bäckvall, P.G. Andersson, P. Brandt, Mechanistic aspects of transition metal-catalyzed hydrogen transfer reactions, *Chemical Society Reviews*, 35 (2006) 237-248.
- [78] N.V. Belkova, L.M. Epstein, E.S. Shubina, Dihydrogen Bonding, Proton Transfer and Beyond: What We Can Learn from Kinetics and Thermodynamics, *European Journal of Inorganic Chemistry*, 2010 (2010) 3555-3565.
- [79] A.R. Higuera-Padilla, A.A. Batista, L. Colina-Vegas, W. Villarreal, L.A. Colnago, Synthesis of the $[(\eta^6\text{-}p\text{-cymene})\text{Ru}(\text{dppb})\text{Cl}]\text{PF}_6$ complex and catalytic activity in the transfer hydrogenation of ketones, *Journal of Coordination Chemistry*, 70 (2017) 3541-3551.
- [80] C. Yuan, L. Zhu, C. Chen, X. Chen, Y. Yang, Y. Lan, Y. Zhao, Ruthenium(II)-enabled para-selective C–H difluoromethylation of anilides and their derivatives, *Nature Communications*, 9 (2018) 1189.
- [81] B. Wang, J. Jiang, H. Yu, Y. Fu, Mechanistic insights into the ruthenium-catalyzed site-selective oxidation of alcohols, *Organic Chemistry Frontiers*, 5 (2018) 2473-2478.
- [82] D. Benitez, E. Tkatchouk, A.Z. Gonzalez, W.A. Goddard, F.D. Toste, On the Impact of Steric and Electronic Properties of Ligands on Gold(I)-Catalyzed Cycloaddition Reactions, *Organic Letters*, 11 (2009) 4798-4801.
- [83] H. Wang, X.-K. Gu, X. Zheng, H. Pan, J. Zhu, S. Chen, L. Cao, W.-X. Li, J. Lu, Disentangling the size-dependent geometric and electronic effects of palladium nanocatalysts beyond selectivity, *Science Advances*, 5 (2019) eaat6413.

- [84] W.P.D. Kaminsky, A. Lenk, V. Scholz, H.W.R. and, A. Herzog, Fluorinated Half-Sandwich Complexes as Catalysts in Syndiospecific Styrene Polymerization, *Macromolecules*, 30 (1997) 7647-7650.
- [85] S. Pal, S. Kusumoto, K. Nozaki, Dehydrogenation of Dimethylamine–Borane Catalyzed by Half-Sandwich Ir and Rh Complexes: Mechanism and the Role of Cp* Noninnocence, *Organometallics*, 37 (2018) 906-914.
- [86] Z.-J. Yao, P. Li, K. Li, W. Deng, Synthesis, structure and catalytic polymerization activity of half-sandwich cyclometallated iridium complexes, *Applied Organometallic Chemistry*, 32 (2018) e4239.
- [87] S. Gonell, E.A. Assaf, K.D. Duffee, C.K. Schauer, A.J.M. Miller, Kinetics of the Trans Effect in Ruthenium Complexes Provide Insight into the Factors That Control Activity and Stability in CO₂ Electroreduction, *Journal of the American Chemical Society*, 142 (2020) 8980-8999.
- [88] M. Navarro, C. Segarra, T. Pfister, M. Albrecht, Structural, Electronic, and Catalytic Modulation of Chelating Pyridylideneamide Ruthenium(II) Complexes, *Organometallics*, 39 (2020) 2383-2391.
- [89] M.L.S. Almeida, M. Beller, G.-Z. Wang, J.-E. Backvall, Ruthenium(II)-Catalyzed Oppenauer-Type Oxidation of Secondary Alcohols, *Chemistry-A European Journal*, 2 (1996) 1533-1536.
- [90] M. Ito, A. Shiibashi, T. Ikariya, Regioselective lactonization of unsymmetrical 1,4-diols: an efficient access to lactone lignans, *Chemical Communications*, 47 (2011) 2134-2136.
- [91] H. Zimmermann, R. Walzl, Ethylene, **Ullmann's Encyclopedia of Industrial Chemistry**, 2009.
- [92] R.J. Tedeschi, Acetylene, in: R.A. Meyers (Ed.) *Encyclopedia of Physical Science and Technology* (3rd Edition), **Academic Press**, New York (2003) 55-89.
- [93] E.L. Joachim Grub, Butadiene, Wiley-VCH Verlag GmbH & Co. KGaA2011.
- [94] S. Mostafalou, H. Bahadar, Cyclohexene, in: P. Wexler (Ed.) *Encyclopedia of Toxicology* (3rd Edition), **Academic Press**, Oxford (2014) 1109-1110.
- [95] F. Lefebvre, Y. Bouhoute, K.C. Szeto, N. Merle, A.d. Mallmann, R. Gauvin, M. Taoufik, Olefin Metathesis by Group VI (Mo, W) Metal Compounds, **Alkenes**, 2018.

- [96] Y.C. Par Jean-Louis Herisson, Catalyse de transformation des oléfines par les complexes du tungstène. II. Télomérisation des oléfines cycliques en présence d'oléfines acycliques, Par Jean-Louis Hérisson, *Yves Chauvin*, 141 (1970) 161-176.
- [97] S. Lwin, Y. Li, A.I. Frenkel, I.E. Wachs, Nature of WO_x Sites on SiO_2 and Their Molecular Structure–Reactivity/Selectivity Relationships for Propylene Metathesis, *ACS Catalysis*, 6 (2016) 3061-3071.
- [98] C.S. Wannere, A. Paul, R. Herges, K.N. Houk, H.F. Schaefer, 3rd, P. von Rague Schleyer, The existence of secondary orbital interactions, *Journal of Computational Chemistry*, 28 (2007) 344-361.
- [99] V.P. Haribal, Y. Chen, L. Neal, F. Li, Intensification of Ethylene Production from Naphtha via a Redox Oxy-Cracking Scheme: Process Simulations and Analysis, *Engineering*, 4 (2018) 714-721.
- [100] D.C. Longstaff, Naphtha Cracking Kinetics and Process Chemistry on Y and ZSM5 Type Catalysts, *Energy & Fuels*, 33 (2019) 2445-2452.
- [101] D.C. Longstaff, Development of a Comprehensive Naphtha Catalytic Cracking Kinetic Model, *Energy & Fuels*, 26 (2012) 801-809.
- [102] M.H.M. Ahmed, O. Muraza, S. Nakaoka, A.K. Jamil, A. Mayoral, V. Sebastian, Z.H. Yamani, T. Masuda, Stability Assessment of Regenerated Hierarchical ZSM-48 Zeolite Designed by Post-Synthesis Treatment for Catalytic Cracking of Light Naphtha, *Energy & Fuels*, 31 (2017) 14097-14103.
- [103] V.R. Jensen, K.J. Borge, M. Ystenes, Ziegler-Natta Ethylene Insertion Reaction for a Five-Coordinate Titanium Chloride Complex Bridged to an Aluminum Hydride Cocatalyst, *Journal of the American Chemical Society*, 117 (1995) 4109-4117.
- [104] L. Wu, D.T. Lynch, S.E. Wanke, Kinetics of Gas-Phase Ethylene Polymerization with Morphology-Controlled $MgCl_2$ -Supported $TiCl_4$ Catalyst, *Macromolecules*, 32 (1999) 7990-7998.
- [105] E. Groppo, K. Seenivasan, E. Gallo, A. Sommazzi, C. Lamberti, S. Bordiga, Activation and In Situ Ethylene Polymerization on Silica-Supported Ziegler–Natta Catalysts, *ACS Catalysis*, 5 (2015) 5586-5595.
- [106] M. Seth, T. Ziegler, Theoretical Study of the Copolymerization of Ethylene and Propylene by a Heterogeneous Ziegler–Natta Catalyst, *Macromolecules*, 37 (2004) 9191-9200.

- [107] M. Seth, T. Ziegler, Polymerization Properties of a Heterogeneous Ziegler–Natta Catalyst Modified by a Base: A Theoretical Study, *Macromolecules*, 36 (2003) 6613-6623.
- [108] I.T. Trotus, T. Zimmermann, N. Duyckaerts, J. Geboers, F. Schuth, Butadiene from acetylene-ethylene cross-metathesis, *Chemical communications (Cambridge)*, 51 (2015) 7124-7127.
- [109] D.P. Debecker, M. Stoyanova, U. Rodemerck, F. Colbeau-Justin, C. Boissère, A. Chaumonnot, A. Bonduelle, C. Sanchez, Aerosol route to nanostructured WO₃-SiO₂-Al₂O₃ metathesis catalysts: Toward higher propene yield, *Applied Catalysis A: General*, 470 (2014) 458-466.
- [110] J. Chauvin, K. Thomas, G. Clet, M. Houalla, Comparative Influence of Surface Tungstate Species and Bulk Amorphous WO₃ Particles on the Acidity and Catalytic Activity of Tungsten Oxide Supported on Silica, *The Journal of Physical Chemistry C*, 119 (2015) 12345-12355.
- [111] C. van Schalkwyk, H.C.M. Vosloo, J.M. Botha, An investigation into the activity of the in situ ruthenium(III) chloride catalytic system for the metathesis of 1-octene, *Journal of Molecular Catalysis A: Chemical*, 190 (2002) 185-195.
- [112] K.W. Chan, D. Mance, O.V. Safonova, C. Coperet, Well-Defined Silica-Supported Tungsten(IV)-Oxo Complex: Olefin Metathesis Activity, Initiation, and Role of Bronsted Acid Sites, *Journal of the American Chemical Society*, 141 (2019) 18286-18292.
- [113] J. Handzlik, K. Kurlito, M. Gierada, Computational Insights into Active Site Formation during Alkene Metathesis over a MoO_x/SiO₂ Catalyst: The Role of Surface Silanols, *ACS Catalysis*, 11 (2021) 13575-13590.
- [114] X. Chen, J. Liu, H. Yan, X. Zhou, S. Yao, Y. Wang, W. Liang, Z. Guo, Y. Liu, X. Feng, X. Jin, C. Yang, Insight into the Effect of Lewis Acid of W/Al-MCM-41 Catalyst on Metathesis of 1-Butene and Ethylene, *Applied Catalysis A: General*, 604 (2020) 117772.
- [115] I.-T. Trotus, T. Zimmermann, N. Duyckaerts, J. Geboers, F. Schüth, Butadiene from acetylene–ethylene cross-metathesis, *Chemical Communications*, 51 (2015) 7124-7127.

- [116] K.W. Chan, D. Mance, O.V. Safonova, C. Copéret, Well-Defined Silica-Supported Tungsten(IV)–Oxo Complex: Olefin Metathesis Activity, Initiation, and Role of Brønsted Acid Sites, *Journal of the American Chemical Society*, 141 (2019) 18286-18292.
- [117] D.K. Gupta, A.N. Sahay, D.S. Pandey, N.K. Jha, P. Sharma, G. Espinosa, A. Cabrera, M.C. Puerta, P. Valerga, Synthesis, characterization, reactivity and structure of some mono and binuclear (η^6 -*p*-cymene)ruthenium(II) complexes, *Journal of Organometallic Chemistry*, 568 (1998) 13-20.
- [118] E. Solari, S. Gauthier, R. Scopelliti, K. Severin, Multifaceted Chemistry of [(Cymene)RuCl₂]₂ and PCy₃, *Organometallics*, 28 (2009) 4519-4526.
- [119] E. Hodson, S.J. Simpson, Synthesis and characterisation of [(η^6 -cymene)Ru(L)X₂] compounds: single crystal X-ray structure of [(η^6 -cymene)Ru(P{OPh}₃)Cl₂] at 203 K, *Polyhedron*, 23 (2004) 2695-2707.
- [120] H. Cao, L.-H. Cai, C.-X. Wang, X.-H. Zhu, Z.-M. Li, X.-F. Hou, Ligand effect in racemization and dynamic kinetic resolution of alcohols: Mechanism on cymene ruthenium complexes, *Journal of Organometallic Chemistry*, 775 (2015) 60-66.
- [121] J.G. Matecki, M. Jaworska, R. Kruszynski, Synthesis, molecular, crystal and electronic structure of [(C₆H₆)RuCl₂(picoline)], *Polyhedron*, 25 (2006) 2519-2524.
- [122] A. Rodríguez-Bárzano, J.D.A. Fonseca, A.J. Blacker, P.C. McGowan, Ruthenium Halide Complexes as N-Alkylation Catalysts, *European Journal of Inorganic Chemistry*, 2014 (2014) 1974-1983.
- [123] P. Chuklin, V. Chalermpanaphan, T. Nhukeaw, S. Saithong, K. Chainok, S. Phongpaichit, A. Ratanaphan, N. Leesakul, Synthesis, X-ray structure of organometallic ruthenium (II) *p*-cymene complexes based on P- and N- donor ligands and their in vitro antibacterial and anticancer studies, *Journal of Organometallic Chemistry*, 846 (2017) 242-250.
- [124] Y.T. Lai, T.C. Chen, Y.K. Lan, B.S. Chen, J.H. You, C.M. Yang, N.C. Lai, J.H. Wu, C.S. Chen, Pt/SBA-15 as a Highly Efficient Catalyst for Catalytic Toluene Oxidation, *ACS Catalysis*, 4 (2014) 3824-3836.

- [125] K. Aghapoor, M.M. Amini, K. Jadidi, F. Mohsenzadeh, H.R. Darabi, H. Sayahi, M.R. Jalali, Synthesis and stability of L-tryptophan adsorbed on Ti/MCM-41 as a catalyst for the regioselective aminolysis of styrene oxide, *Solid State Sciences*, 49 (2015) 10-17.
- [126] L. Zhang, D.H. Nguyen, G. Raffa, X. Trivelli, F. Capet, S. Desset, S. Paul, F. Dumeignil, R.M. Gauvin, Catalytic Conversion of Alcohols into Carboxylic Acid Salts in Water: Scope, Recycling, and Mechanistic Insights, *ChemSusChem*, 9 (2016) 1413-1423.
- [127] A. Sølvhøj, R. Madsen, Dehydrogenative Coupling of Primary Alcohols To Form Esters Catalyzed by a Ruthenium N-Heterocyclic Carbene Complex, *Organometallics*, 30 (2011) 6044-6048.
- [128] J. Klein, J. Beerhues, D. Schweinfurth, M. van der Meer, M. Gazvoda, G.K. Lahiri, J. Košmrlj, B. Sarkar, Versatile Coordination of Azocarboxamides: Redox-Triggered Change of the Chelating Binding Pocket in Ruthenium Complexes, *Chemistry – A European Journal*, 24 (2018) 18020-18031.
- [129] Y. Fang, Z. Xiao, A. Kirchon, J. Li, F. Jin, T. Togo, L. Zhang, C. Zhu, H.-C. Zhou, Bimolecular proximity of a ruthenium complex and methylene blue within an anionic porous coordination cage for enhancing photocatalytic activity, *Chemical Science*, 10 (2019) 3529-3534.
- [130] S. Mostrou, T. Sipőcz, A. Nagl, B. Földi, F. Darvas, K. Föttinger, J.A. van Bokhoven, Catalytic oxidation of aqueous bioethanol: an efficient upgrade from batch to flow, *Reaction Chemistry & Engineering*, 3 (2018) 781-789.
- [131] D.T. Ngo, T. Sooknoi, D.E. Resasco, Improving stability of cyclopentanone aldol condensation MgO-based catalysts by surface hydrophobization with organosilanes, *Applied Catalysis B: Environmental*, 237 (2018) 835-843.
- [132] M.H. Chisholm, K. Choojun, J.C. Gallucci, P.M. Wambua, Chemistry of magnesium alkyls supported by 1,5,9-trimesityldipyrromethene and 2-[(2,6-diisopropylphenyl)amino]-4-[(2,6-diisopropylphenyl)imino]pent-2-ene. A comparative study, *Chemical Science*, 3 (2012) 3445-3457.
- [133] M. Pompeo, J.L. Farmer, R.D. Froese, M.G. Organ, Room-temperature amination of deactivated aniline and aryl halide partners with carbonate base using a Pd-PEPSSI-IPentCl-o-picoline catalyst, *Angewandte Chemie International edition in English*, 53 (2014) 3223-3226.

- [134] E.I. Ross-Medgaarden, I.E. Wachs, Structural Determination of Bulk and Surface Tungsten Oxides with UV-vis Diffuse Reflectance Spectroscopy and Raman Spectroscopy, *The Journal of Physical Chemistry C*, 111 (2007) 15089-15099.
- [135] A. Kuzmin, J. Purans, X-ray absorption spectroscopy study of the local environment around tungsten and molybdenum ions in tungsten-phosphate and molybdenum-phosphate glasses, *Proc.SPIE*, 1997.
- [136] J.G. Howell, Y.-P. Li, A.T. Bell, Propene Metathesis over Supported Tungsten Oxide Catalysts: A Study of Active Site Formation, *ACS Catalysis*, 6 (2016) 7728-7738.
- [137] D.S. Kim, M. Ostromecki, I.E. Wachs, Surface structures of supported tungsten oxide catalysts under dehydrated conditions, *Journal of Molecular Catalysis A: Chemical*, 106 (1996) 93-102.
- [138] M.F. Daniel, B. Desbat, J.C. Lassegues, B. Gerand, M. Figlarz, Infrared and Raman study of WO_3 tungsten trioxides and $WO_3 \cdot xH_2O$ tungsten trioxide hydrates, *Journal of Solid State Chemistry*, 67 (1987) 235-247.
- [139] L.R. Pizzio, C.V. Cáceres, M.N. Blanco, Tungsten-alumina based catalysts. I. Genesis by impregnation with different tungsten solutions, *Catalysis Letters*, 33 (1995) 175-192.
- [140] Y. Bouhoute, D. Grekov, K.C. Szeto, N. Merle, A. De Mallmann, F. Lefebvre, G. Raffa, I. Del Rosal, L. Maron, R.M. Gauvin, L. Delevoye, M. Taoufik, Accessing Realistic Models for the WO_3 - SiO_2 Industrial Catalyst through the Design of Organometallic Precursors, *ACS Catalysis*, 6 (2015) 1-18.
- [141] P. Jiang, Y. Xiao, W. Liu, X. Yu, Hydrogen reduction characteristics of WO_3 based on density functional theory, *Results in Physics*, 12 (2019) 896-902.
- [142] T.R. Wilken, W.R. Morcom, C.A. Wert, J.B. Woodhouse, Reduction of tungsten oxide to tungsten metal, *Metallurgical Transactions B*, 7 (1976) 589-597.
- [143] H. Lischka, E. Ventura, M. Dallos, The Diels-Alder reaction of ethene and 1,3-butadiene: an extended multireference ab initio investigation, *Chemphyschem*, 5 (2004) 1365-1371.
- [144] C.-X. Cui, Y.-J. Liu, A thorough understanding of the Diels-Alder reaction of 1,3-butadiene and ethylene, *Journal of Physical Organic Chemistry*, 27 (2014) 652-660.

- [145] T.R. Karpova, E.A. Buluchevskiy, M.A. Moiseenko, A.V. Lavrenov, A.B. Arbuzov, Direct conversion of ethylene to propylene over NiO/WO₃/Al₂O₃ catalysts, *21st Century: Chemistry to Life*, **2019**.
- [146] Z. Xu, J.P. Chada, L. Xu, D. Zhao, D.C. Rosenfeld, J.L. Rogers, I. Hermans, M. Mavrikakis, G.W. Huber, Ethylene Dimerization and Oligomerization to 1-Butene and Higher Olefins with Chromium-Promoted Cobalt on Carbon Catalyst, *ACS Catalysis*, **8** (2018) 2488-2497.
- [147] Y. Wang, Q. Chen, W. Yang, Z. Xie, W. Xu, D. Huang, Effect of support nature on WO₃/SiO₂ structure and butene-1 metathesis, *Applied Catalysis A: General*, **250** (2003) 25-37.
- [148] R. Gao, X. Yang, W. Dai, Y. Le, H. Li, K. Fan, High-activity, single-site mesoporous WO₃-MCF materials for the catalytic epoxidation of cycloocta-1,5-diene with aqueous hydrogen peroxide, *Journal of Catalysis*, **256** (2008) 259-267.
- [149] B. Hu, H. Liu, K. Tao, C. Xiong, S. Zhou, Highly Active Doped Mesoporous KIT-6 Catalysts for Metathesis of 1-Butene and Ethene to Propene: The Influence of Neighboring Environment of W Species, *The Journal of Physical Chemistry C*, **117** (2013) 26385-26395.
- [150] F. Adam, A. Iqbal, The liquid phase oxidation of styrene with tungsten modified silica as a catalyst, *Chemical Engineering Journal*, **171** (2011) 1379-1386.
- [151] X. Yang, W. Dai, R. Gao, K. Fan, Characterization and catalytic behavior of highly active tungsten-doped SBA-15 catalyst in the synthesis of glutaraldehyde using an anhydrous approach, *Journal of Catalysis*, **249** (2007) 278-288.
- [152] M. Izadyar, A. Jamsaz, Cyclic Nanostructures of Tungsten Oxide (WO₃)_n (n = 2-6) as NO_x Gas Sensor: A Theoretical Study, *International Journal of Analytical Chemistry*, **2014** (2014) 240197.
- [153] L. Sai, L. Tang, X. Huang, G. Chen, J. Zhao, J. Wang, Lowest-energy structures of (WO₃)_n (2 ≤ n ≤ 12) clusters from first-principles global search, *Chemical Physics Letters*, **544** (2012) 7-12.
- [154] D.M. David Jeba Singh, T. Pradeep, K. Thirumoorthy, K. Balasubramanian, Closed-Cage Tungsten Oxide Clusters in the Gas Phase, *The Journal of Physical Chemistry A*, **114** (2010) 5445-5452.

- [155] X. Huang, H.-J. Zhai, J. Li, L.-S. Wang, On the Structure and Chemical Bonding of Tri-Tungsten Oxide Clusters $W_3O_n^-$ and W_3O_n ($n = 7-10$): W_3O_8 As A Potential Molecular Model for O-Deficient Defect Sites in Tungsten Oxides, *The Journal of Physical Chemistry A*, 110 (2006) 85-92.
- [156] S. Maksasithorn, D.P. Debecker, P. Prasertthdam, J. Panpranot, K. Suriye, S.K.N. Ayudhya, NaOH modified WO_3/SiO_2 catalysts for propylene production from 2-butene and ethylene metathesis, *Chinese Journal of Catalysis*, 35 (2014) 232-241.
- [157] M. Ide, M. El-Roz, E. De Canck, A. Vicente, T. Planckaert, T. Bogaerts, I. Van Driessche, F. Lynen, V. Van Speybroeck, F. Thybault-Starzyk, P. Van Der Voort, Quantification of silanol sites for the most common mesoporous ordered silicas and organosilicas: total versus accessible silanols, *Physical Chemistry Chemical Physics*, 15 (2013) 642-650.
- [158] T. Kentri, A. Trimpalis, A. Misa, E. Kordouli, T. Ramantani, S. Boghosian, Rethinking the molecular structures of $W(VI)O_x$ sites dispersed on titania: distinct mono-oxo configurations at 430 degrees C and temperature-dependent transformations, *Dalton Transaction*, 51 (2022) 7455-7475.
- [159] E.L. Lee, I.E. Wachs, In Situ Spectroscopic Investigation of the Molecular and Electronic Structures of SiO_2 Supported Surface Metal Oxides, *The Journal of Physical Chemistry C*, 111 (2007) 14410-14425.
- [160] A. Tribalis, G.D. Panagiotou, G. Tsilomelekis, A.G. Kalampounias, K. Bourikas, C. Kordulis, S. Boghosian, A. Lycourghiotis, Temperature-Dependent Evolution of the Molecular Configuration of Oxo-Tungsten(VI) Species Deposited on the Surface of Titania, *The Journal of Physical Chemistry C*, 118 (2014) 11319-11332.
- [161] A. Spamer, T.I. Dube, D.J. Moodley, C. van Schalkwyk, J.M. Botha, Application of a WO_3/SiO_2 catalyst in an industrial environment: part II, *Applied Catalysis A: General*, 255 (2003) 133-142.

APPENDICES

APPENDIX A

Geometrical Effect on Single-Site Ruthenium Catalyst

A1. Crystallographic details of the new (*p*-cymene)RuCl₂(L_{N3}) compound

For the new (*p*-cymene)RuCl₂(L_{N3}) complex, the reaction was performed in dichloromethane at room temperature. This complex is air-stable under ambient conditions, and its structure is confirmed by NMR spectra, as shown in **Figures A1-A2**. These complexes are soluble in common organic solvents, such as acetone, DMF, CH₂Cl₂, and methanol. However, they are insoluble in water.

The crystallographic details and molecular structure of a new (*p*-cymene)RuCl₂(L_{N3}) complex are shown in **Table A1** and **Figure A3**, respectively. The selected bond lengths and angles are summarized in **Table A2**. It can be seen that this complex has a pseudo-tetrahedral geometry with vertex distances of 2.408(10), 2.418(9), 2.129(3), and 1.669 Å for Ru-Cl(1), Ru-Cl(2), Ru-N, and Ru-(centroid of the *p*-cymene ring), respectively. While, the bond length of Ru-C (in *p*-cymene) is in the range of 2.174(6)-2.204(0) Å, which is similar to those reported in the literature [117-123]. In this complex, the Ru-N is slightly shorter than those of (*p*-cymene)RuCl₂(L_{N1}) (2.17 Å) [120]. This could attribute to the higher electron density of 4-*tert*-butylpyridine (L_{N3}) as compared to pyridine (L_{N1}). Accordingly, a stronger overlapping interaction between Ru and alkyl-substituted ligands could be expected. In a supportive manner, the previously reported complexes with a donating group on pyridine ligand (*i.e.*, L_{N2} and L_{N5}) also show a shorter Ru-N bond (~2.13 Å) (**Table A2, entry 3, Appendix A**) [121, 122].

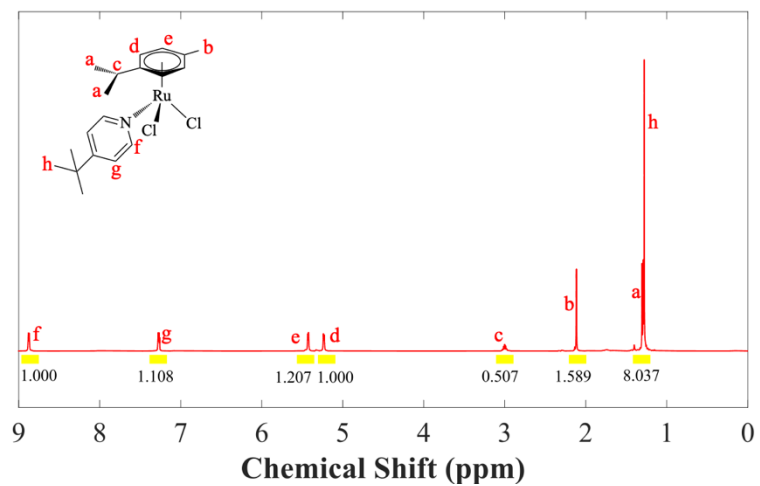


Figure A1 ^1H 500 MHz NMR spectrum of $(p\text{-cymene})\text{RuCl}_2(\text{L}_{\text{N}_3})$ in $\text{chloroform-}d_1$

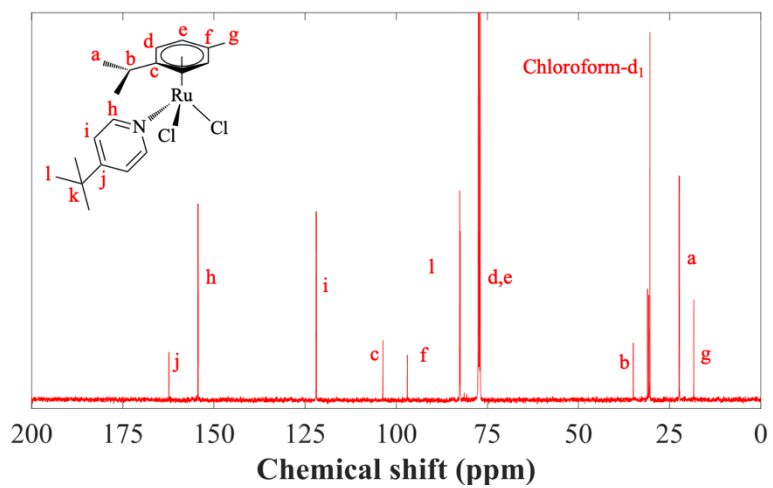


Figure A2 ^{13}C 500 MHz NMR spectrum of $(p\text{-cymene})\text{RuCl}_2(\text{L}_{\text{N}_3})$ in $\text{chloroform-}d_1$

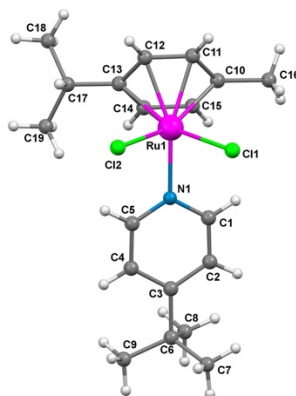


Figure A3 ORTEP representation (50% probability ellipsoid) of complex $(p\text{-cymene})\text{RuCl}_2(\text{L}_{\text{N}3})$ (minor disorder part of the methyl group at C6 are omitted for clarity)

Table A1 Crystallographic detail of $(p\text{-cymene})\text{RuCl}_2(\text{L}_{\text{N}3})$

Compound complex	$(p\text{-cymene})\text{RuCl}_2(4\text{-tert-butylpyridine})$
Formula	$\text{C}_{19}\text{H}_{27}\text{RuNCl}_2$
Formula weight	441.38
Temperature	296(2) K
Wavelength	0.71073 Å
Crystal system	Monoclinic
Space group	$C2/c$
Unit cell dimensions	a = 22.7883(10) Å b = 14.3449(6) Å β = 111.2710(10)° c = 12.9580(6) Å
Volume	3947.3 Å ³
Density (calculated)	1.485 Mg m ⁻³
Absorption coefficient	1.064 mm ⁻¹
F(000)	1808
Crystal size	0.400 x 0.120 x 0.120 mm ³
Theta range for data collection	5-50° 3.103 to 24.997°
Index ranges	-27<=h<=27, -16<=k<=17, -15<=l<=15
Reflections collected	47536
Independent reflections	3772 [R(int) = 0.0849]
Completeness to theta max = 24.997°	99.9%
Refinement method	Full-matrix least-squares on F ²
Data/restraints/parameters	3772 / 102 / 245
Goodness-of-fit on F ²	1.040
Final R indices	R1 = 0.0353, wR2 = 0.0758
R indices (all data)	R1 = 0.0519, wR2 = 0.0830
Largest diff. peak and hole	0.888 and -0.735 e.Å ⁻³
CCDC Number	1970821

Table A2 Selected bond distances (Å) and bond angles (°) for the Ru complexes

Entry	Atom	(p-cymene)RuCl ₂ (L)							
		L _{P1} ¹	L _{P2} ²	L _{P4} ³	L _{P5} ⁴	L _{N1} ⁵	L _{N2} ⁶	L _{N3}	L _{N5} ⁷
Distances (Å)									
1	Ru-Cl(1)	2.402(3)	2.3992(8)	2.4151(5)	2.4039(9)	2.4515(5)	2.423(2)	2.4082(10)	2.414(2)
2	Ru-Cl(2)	2.379(4)	2.4022(8)	2.4154(6)	2.415(1)	2.4382(5)	2.426(2)	2.4178(9)	2.409(2)
3	Ru-L	2.425(2)	2.2642(8)	2.3438(6)	2.3500(8)	2.172(1)	2.133(6)	2.1290(3)	2.124(8)
4	Ru-(centroid of p-cymene)	1.705	1.701	1.708	1.694	1.686	1.677	1.6690	1.658
5	Ru-C(10)	2.225	2.223	2.213	2.203	2.220	2.214	2.201(4)	2.184
6	Ru-C(11)	2.212	2.203	2.176	2.161	2.212	2.183	2.187(4)	2.166
7	Ru-C(12)	2.219	2.178	2.213	2.178	2.229	2.178	2.174(4)	2.192
8	Ru-C(13)	2.218	2.199	2.247	2.205	2.246	2.225	2.197(4)	2.193
9	Ru-C(14)	2.225	2.242	2.245	2.235	2.215	2.179	2.174(3)	2.168
10	Ru-C(15)	2.195	2.247	2.216	2.226	2.189	2.182	2.177(3)	2.153
11	Average Ru-Cl	2.391	2.401	2.415	2.409	2.445	2.425	2.413	2.412
Angles (°)									
12	Cl(1)-Ru-Cl(2)	88.0(1)	87.45(2)	88.40(2)	88.78(3)	87.45(1)	88.87(6)	87.94(4)	88.73(7)
13	Cl(1)-Ru-L	87.5(1)	85.02(2)	90.27(2)	82.45(3)	85.88(4)	84.8(2)	84.36(8)	87.0(2)
14	Cl(2)-Ru-L	87.4(1)	87.91(3)	87.10(2)	87.85(3)	86.85(4)	85.5(2)	87.52(8)	85.86(2)
15	C(1)-N-C(5)	-	-	-	-	118.0(2)	118.3(6)	116.60(3)	115.1(6)
16	X(1)-P-X(2)	106.4(5)	102.0(1)	100.81(9)	103.2(2)	-	-	-	-
17	X(1)-P-X(3)	101.0(5)	104.7(1)	106.29(9)	105.1(2)	-	-	-	-
18	X(2)-P-X(3)	101.8(4)	98.7(1)	99.56(9)	105.4(2)	-	-	-	-
19	Cl(1)-Ru-(centroid p-cymene)	124.36	126.86	124.67	124.76	128.90	127.26	127.80(6)	125.76
20	Cl(2)-Ru-(centroid p-cymene)	123.84	123.97	125.86	127.13	128.78	128.96	127.37(7)	128.55
21	L(1)-Ru-(centroid p-cymene)	132.31	131.61	128.20	131.56	128.94	128.16	127.68(9)	127.53

L represents coordinated P, or N

X represents ligand substituent C or O

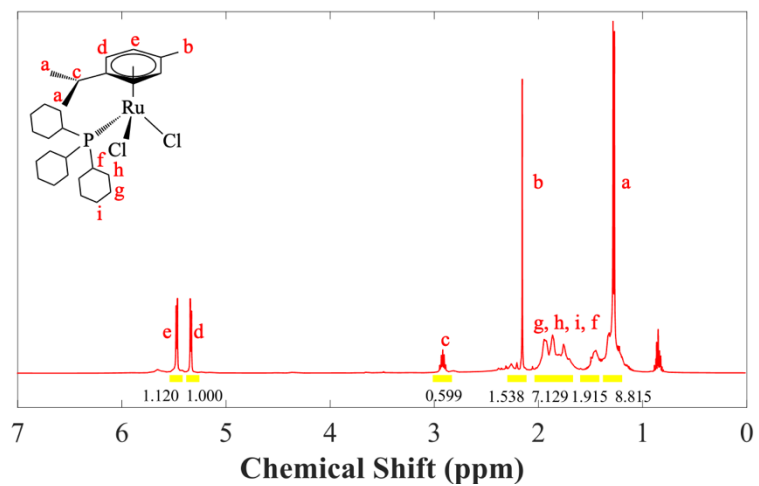


Figure A4 ^1H 500 MHz NMR spectrum of $(p\text{-cymene})\text{RuCl}_2(\text{L}_{\text{P}1})$ in chloroform- d_1

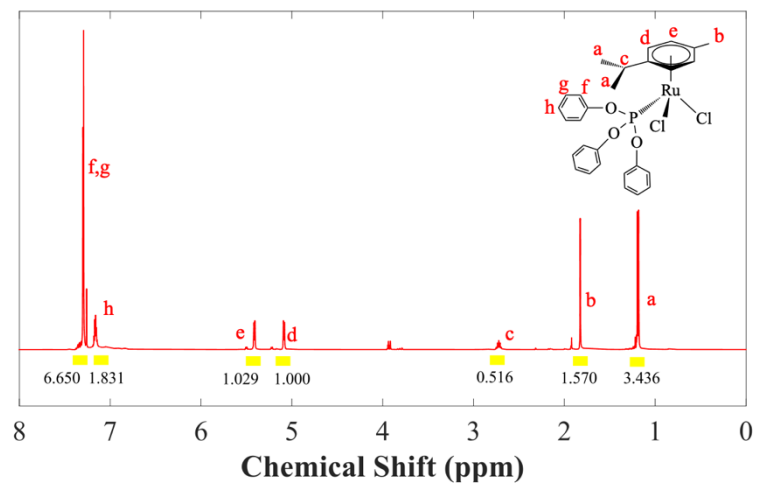


Figure A5 ^1H 500 MHz NMR spectrum of $(p\text{-cymene})\text{RuCl}_2(\text{L}_{\text{P}2})$ in chloroform- d_1

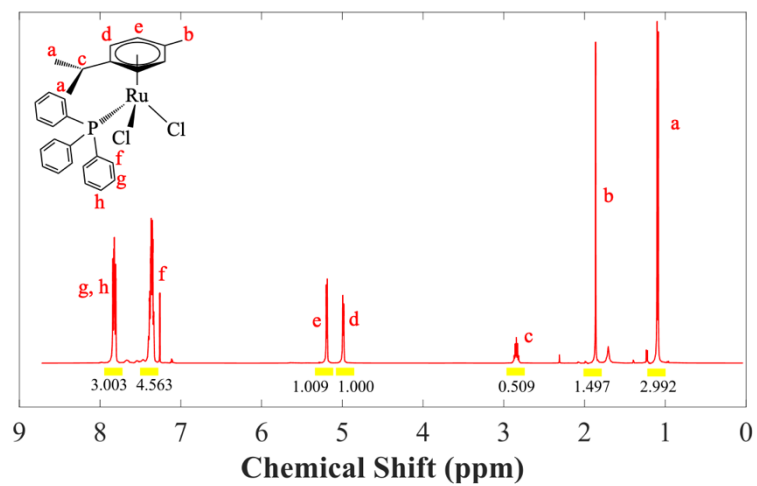


Figure A6 ^1H 500 MHz NMR spectrum of $(p\text{-cymene})\text{RuCl}_2(\text{L}_{\text{P4}})$ in chloroform- d_1

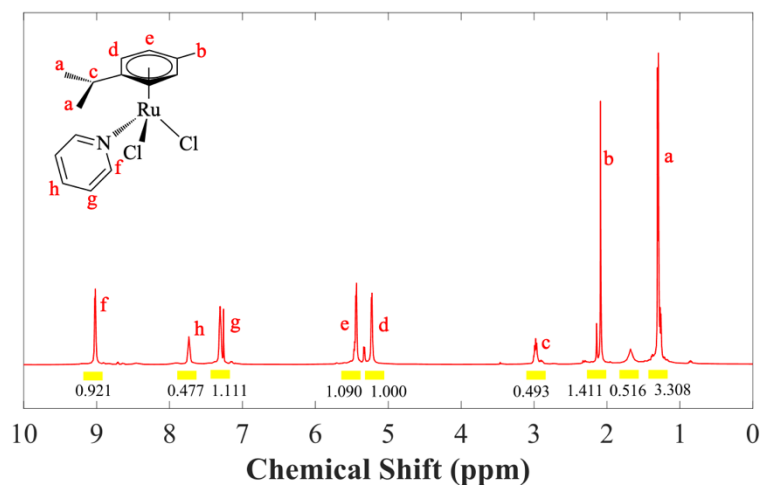


Figure A7 ^1H 500 MHz NMR spectrum of $(p\text{-cymene})\text{RuCl}_2(\text{L}_{\text{N1}})$ in chloroform- d_1

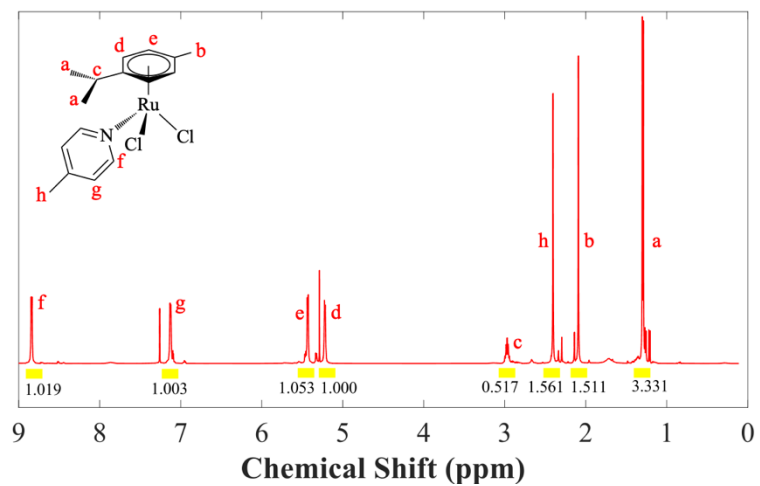


Figure A8 ^1H 500 MHz NMR spectrum of $(p\text{-cymene})\text{RuCl}_2(\text{L}_{\text{N}2})$ in chloroform- d_1

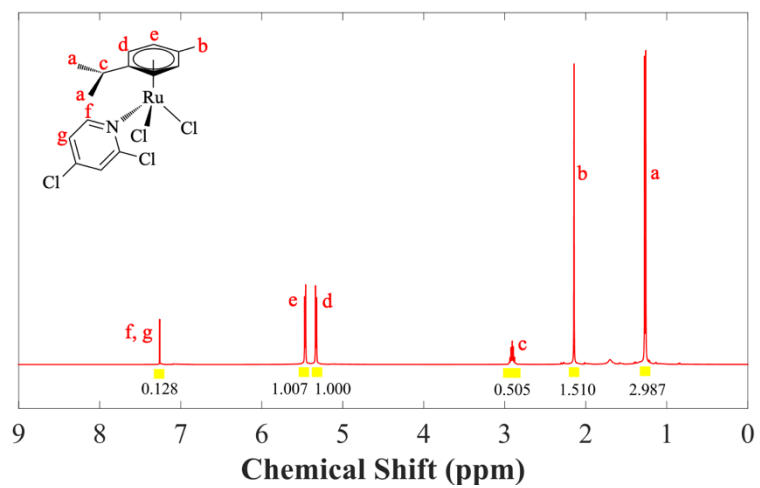


Figure A9 ^1H 500 MHz NMR spectrum of $(p\text{-cymene})\text{RuCl}_2(\text{L}_{\text{N}4})$ in chloroform- d_1

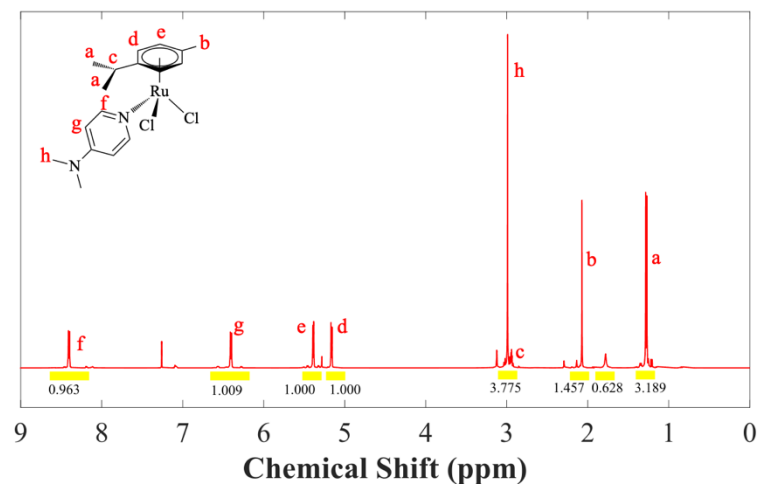


Figure A10 ^1H 500 MHz NMR spectrum of $(p\text{-cymene})\text{RuCl}_2(\text{L}_{\text{N}5})$ in CDCl_3

A2. The oxidation of 1,6-hexanediol over Ru complex catalysts

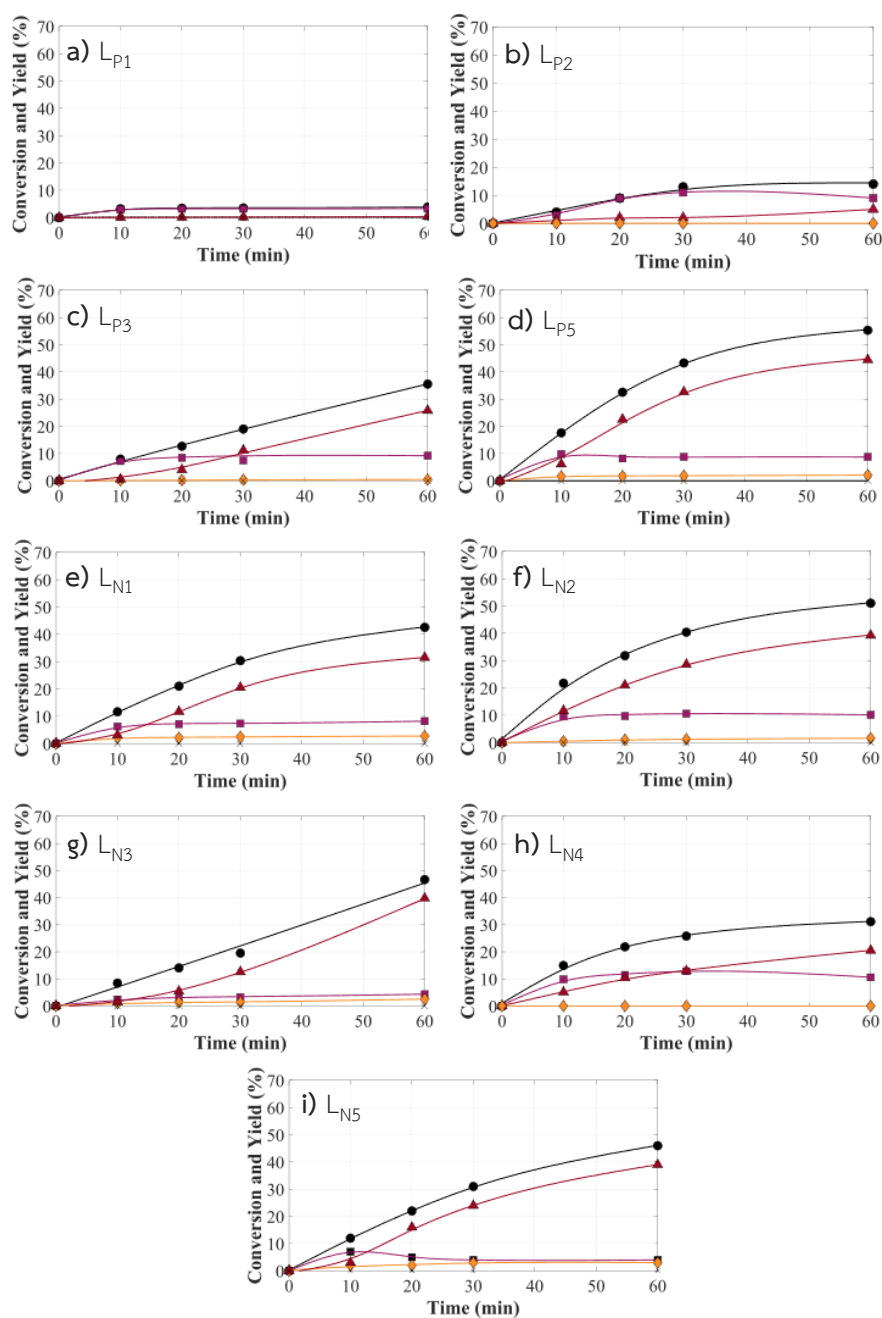


Figure A11 1,6-HD oxidation time profile using (*p*-cymene)RuCl₂L catalysts where a) L_{P1}, b) L_{P2}, c) L_{P3}, d) L_{P5}, e) L_{N1}, f) L_{N2} g) L_{N3}, h) L_{N4}, i) L_{N5} and j) [(*p*-cymene)RuCl₂]₂ catalyst (conversion (●), 6-hydroxyhexa-1-nal (■), 1,6-hexanedial (◇), ε-CL (▲), and adipic acid (×)) (0.025 mmol Ru complex, 1 mmol 1,6-HD, under N₂ atmosphere, 110 °C, 30 mL toluene, 0.2 mmol K₂CO₃, 8 mmol MIBK)

Table A3 6-Hydroxyhexan-1-al and ϵ -caprolactone selectivity at the similar conversion extrapolated from the reaction profile using (*p*-cymene)RuCl₂(L) catalysts

Entry	Ligands	Bases	Conversion (%)	Selectivity (%)	
				6-Hydroxyhexan-1-al	ϵ -CL
1	L _{P3}	K ₂ CO ₃	28	36	64
2	L _{P4}	K ₂ CO ₃	28	36	64
3	L _{P5}	K ₂ CO ₃	28	36	64
4	L _{N1}	K ₂ CO ₃	28	29	68
5	L _{N2}	K ₂ CO ₃	28	36	64
6	L _{N3}	K ₂ CO ₃	28	21	61
7	L _{N4}	K ₂ CO ₃	28	39	61
8	L _{N5}	K ₂ CO ₃	28	21	68
9	L _{P3}	KOH	28	33	64
10	L _{P3}	<i>t</i> -BuOK	25	28	72

*(0.025 mmol Ru complex, 1 mmol 1,6-HD, under N₂ atmosphere, 110 °C, 30 mL toluene,

0.2 mmol base, 8 mmol MIBK).

A3. Deactivation test for Ru complexes during the oxidation

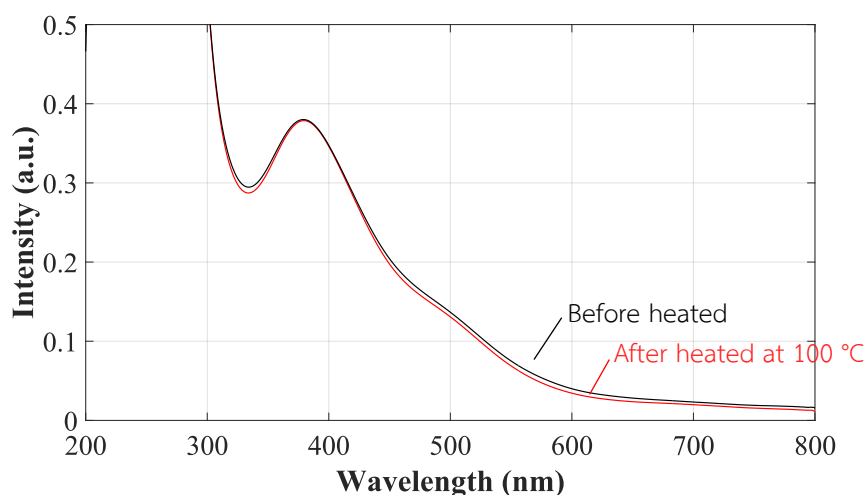


Figure A12 UV-VIS spectra of (*p*-cymene) $\text{RuCl}_2(\text{L}_{\text{P}4})$ a) before (–) and after (–) heated at 110 °C in the presence of K_2CO_3 in toluene

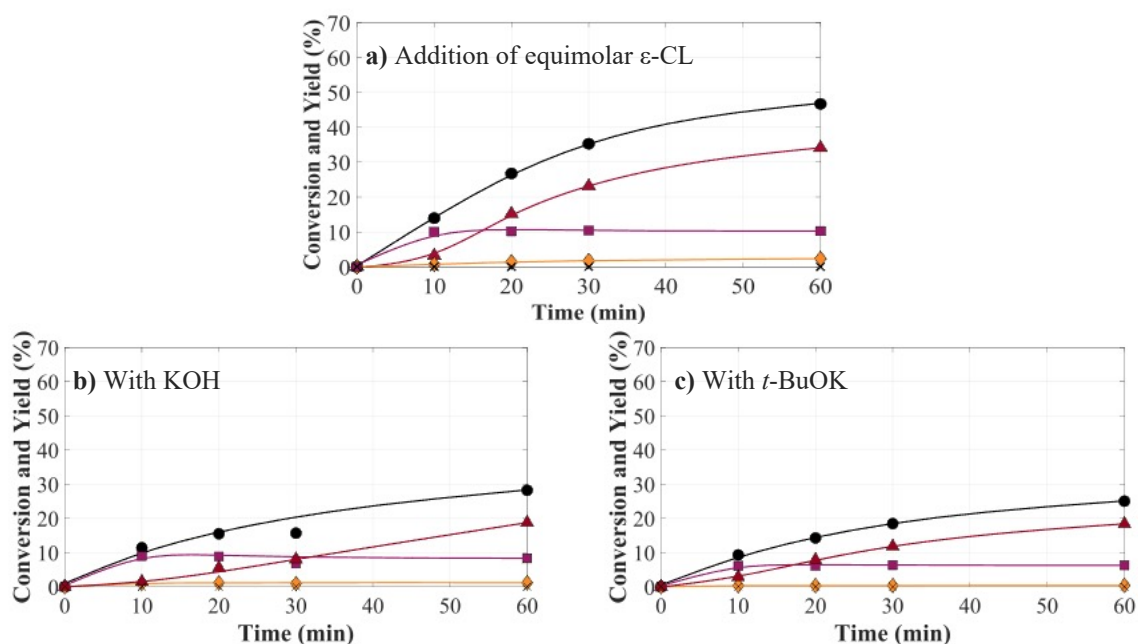


Figure A13 1,6-HD oxidation time profile using (*p*-cymene) $\text{RuCl}_2(\text{L}_{\text{P}4})$ catalyst with a) the addition of equimolar $\epsilon\text{-CL}$, b) KOH and c) *t*- BuOK (conversion (●), 6-hydroxyhexan-1-ol (■), 1,6-hexanedial (◇), $\epsilon\text{-CL}$ (▲), and adipic acid (×)) (0.025 mmol Ru complex, 1 mmol 1,6-HD, under N_2 atmosphere, 110 °C, 30 mL toluene, 0.2 mmol K_2CO_3 , 8 mmol MIBK)

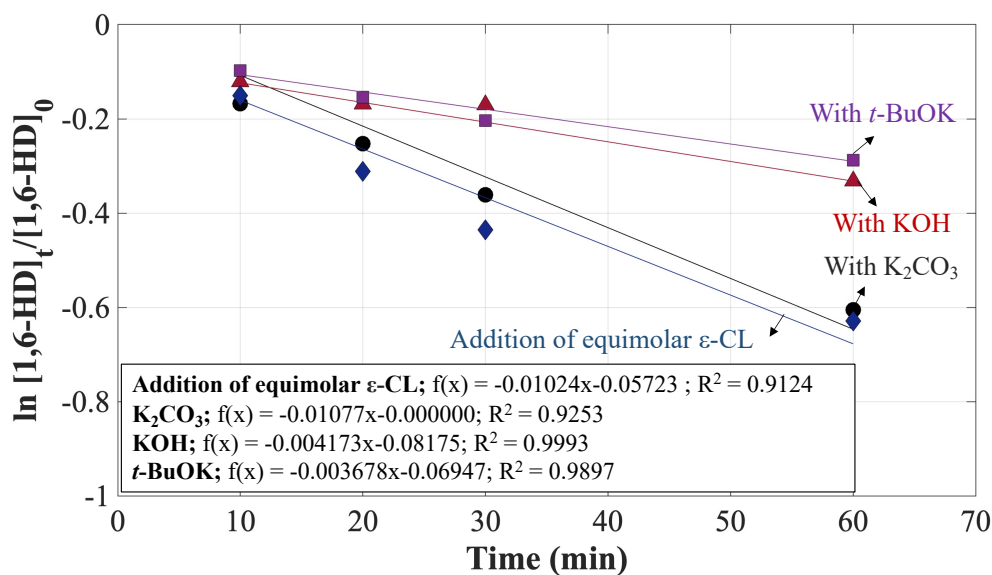


Figure A14 Kinetics plot of 1,6-HD oxidation using (*p*-cymene) $\text{RuCl}_2(\text{L}_{\text{P}4})$ catalyst with the addition of equimolar $\epsilon\text{-CL}$ (\blacklozenge), K_2CO_3 (\bullet), KOH (\blacktriangle), and *t*-BuOK (\blacksquare) (0.025 mmol Ru complex, 1 mmol 1,6-HD, under N_2 atmosphere, 110 °C, 30 mL toluene, 0.2 mmol base, 8 mmol MIBK)

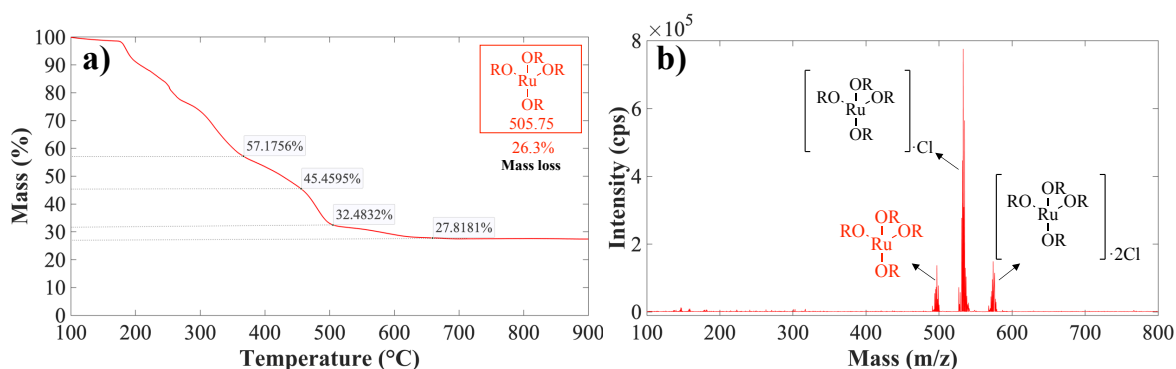


Figure A15 TGA curve under air-zero (a) and mass spectra (b) attained by QTOF mass spectrometry electrospray analysis of $\text{Ru}(\text{MIBC})_4$.

In addition to ^{13}C CPMAS NMR (Figure 4.8), the TGA curve of the brown solids precipitated after mixing (*p*-cymene) $\text{RuCl}_2(\text{L}_{\text{P}4})$ and MIBC (in excess) showed a mass loss of ~72% of the decomposable organic fraction at 600 °C (Figure A15a). This can be attributed to four alkyl groups of MIBC, bearing approximately 28% of RuO_2 (134 g/mol) from the $\text{Ru}(\text{MIBC})_4$ (506 g/mol). A slightly higher mass (~28%) compared to the theoretical value (~26%, $134 \times 100 / 506$) indicates a trace of Cl remained in the solid precipitate. This can be evidenced by QTOF mass spectra (Figure 15b), showing that

M+35/37 ($\text{Ru}(\text{MIBC})_4\cdot\text{Cl}$, $m/z\sim 541/543$) and M+70/74 ($\text{Ru}(\text{MIBC})_4\cdot 2\text{Cl}$, $m/z\sim 576/578$) are largely pronounced.

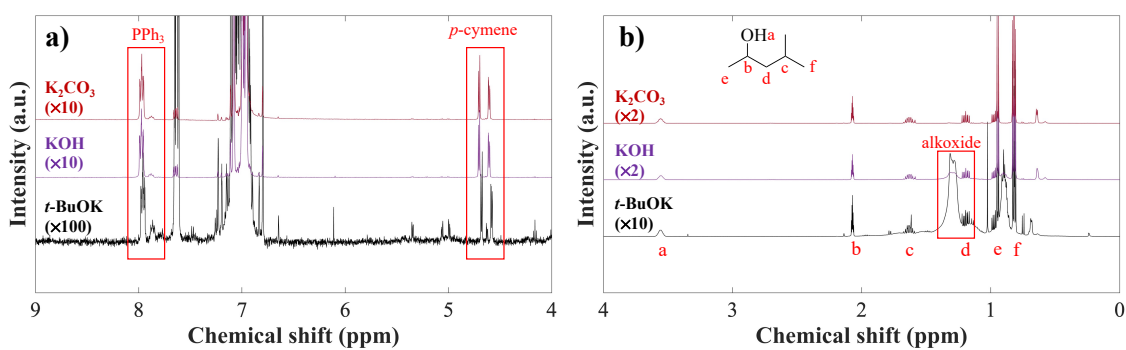


Figure A16 500 MHz ^1H NMR spectra of the reaction of (p -cymene) $\text{RuCl}_2(\text{L}_{\text{P}4})$ with 34 mmol MIBC at 110 $^\circ\text{C}$ for 5 min in toluene- d_8 after left overnight; a) 0-10 ppm and b) zoom 0-4 p

APPENDIX B

Geometrical Effect on Tungsten Oxide Catalysts

B1. The formation of WO₃ species over siliceous support

Table B1 Energy gap derived from UV-VIS DRS spectra

Entry	Sample	Energy gap (eV)
1	2%WO ₃ /SiO ₂	4.51 and 5.18
2	3%WO ₃ /SiO ₂	4.52 and 5.17
3	5%WO ₃ /SiO ₂	4.52 and 5.18
4	7%WO ₃ /SiO ₂	2.75 and 5.24
5	5%WO ₃ /NaY	2.75 and 5.24
6	5%WO ₃ /NaX	4.51 and 5.14
7	5%WO ₃ /MCM-41	4.52 and 5.21
8	5%WO ₃ /SBA-15	4.55 and 5.12

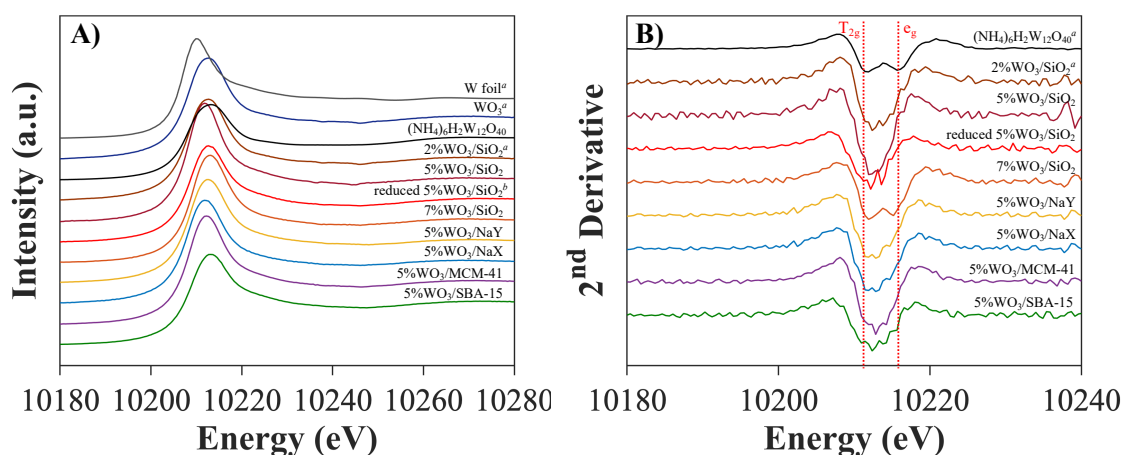


Figure B1 A) normalized and B) 2nd derivative W L₃-edge *in situ* TR-XANES spectra of all catalysts and W standard at 500°C under air-zero (^aEstimated at room temperature and ^bunder H₂ gas)

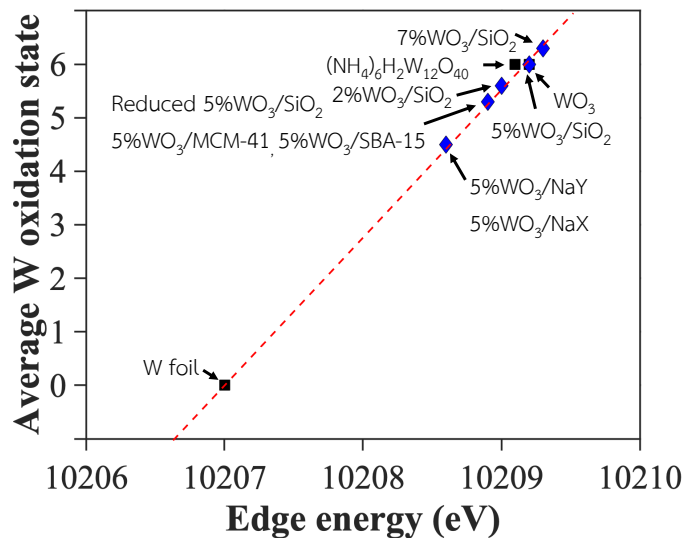


Figure B2 Average oxidation state determination from W L₃-edge energy of W standard

Table B2 W L₃-edge energy and average W oxidation state of all samples at 500°C under air-zero 30 mL·min⁻¹

Entry	Sample	Edge energy (eV)	Average oxidation state
1	5%WO ₃ /SiO ₂	10209.2	6.0
2	reduced 5%WO ₃ /SiO ₂ ^b	10208.9	5.3
3	2%WO ₃ /SiO ₂ ^a	10209.0	5.6
4	7%WO ₃ /SiO ₂	10209.3	6.3
5	5%WO ₃ /NaY	10208.6	4.5
6	5%WO ₃ /NaX	10208.6	4.5
7	5%WO ₃ /MCM-41	10208.9	5.3
8	5%WO ₃ /SBA-15	10208.9	5.3
9	WO ₃ ^a	10209.1	6.0
10	(NH ₄) ₆ H ₂ W ₁₂ O ₄₀ ·4H ₂ O ^a	10209.2	6.0
11	W foil ^a	10207.0	0.0

^aEstimated at room temperature and ^bunder H₂ gas

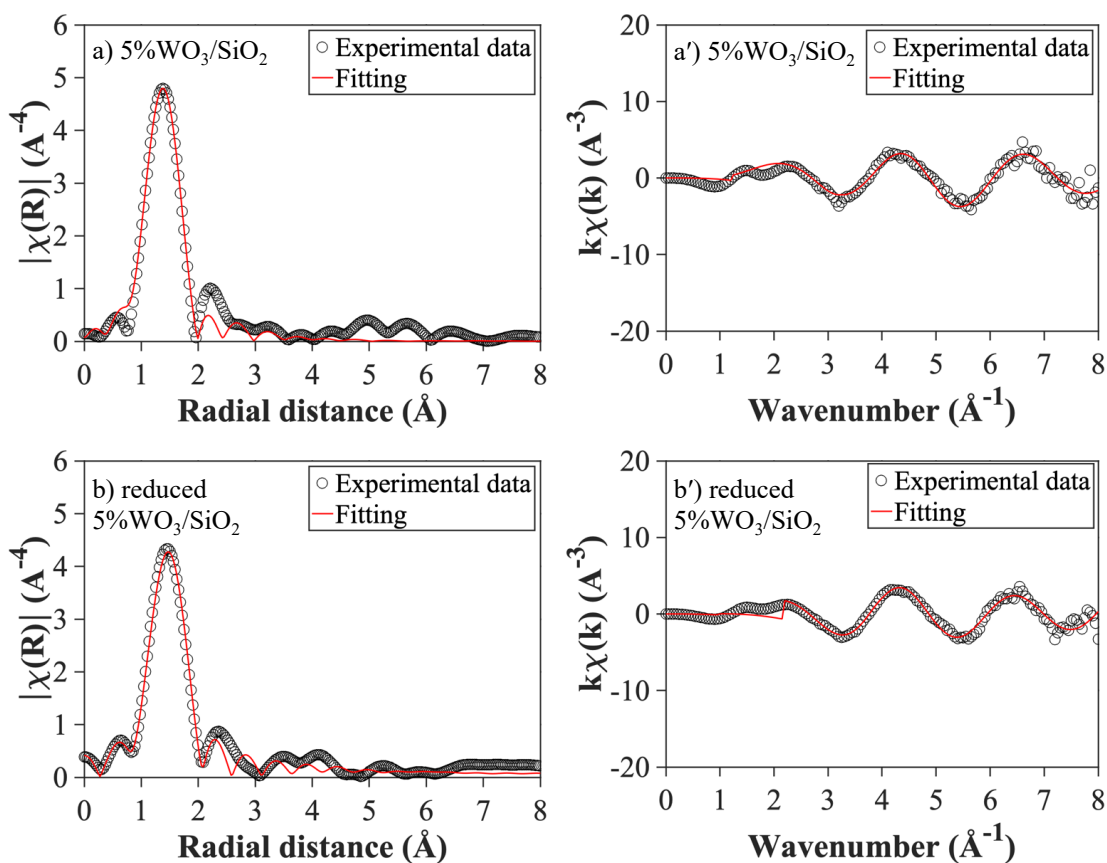


Figure B3 W L₃-edge *in situ* TR-EXAFS Fitting of a, a') 5%WO₃/SiO₂ and b, b') reduced 5%WO₃/SiO₂ at 500°C.

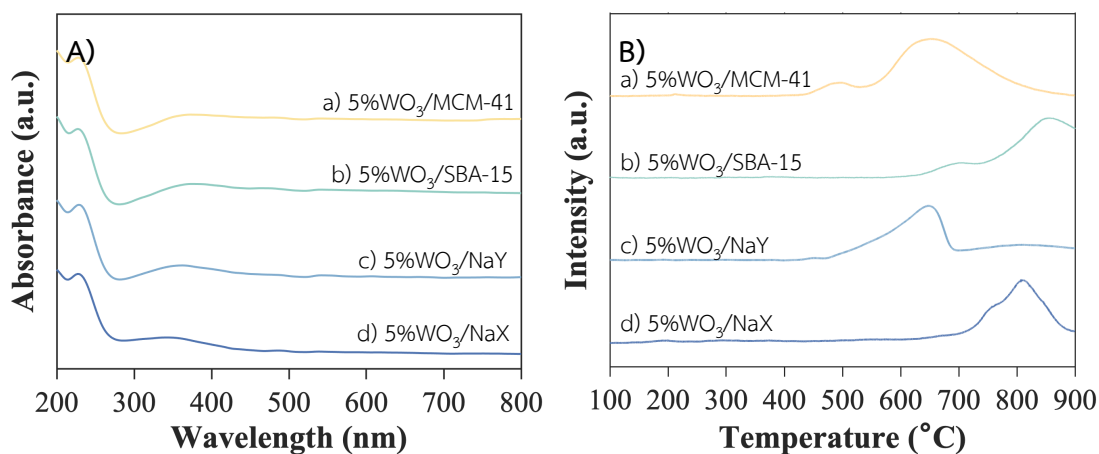


Figure B4 UV-VIS DRS spectra (A) and H₂-TPR profile (B) of WO₃ over confined silica support

B2. Acid properties of WO₃ supported catalysts

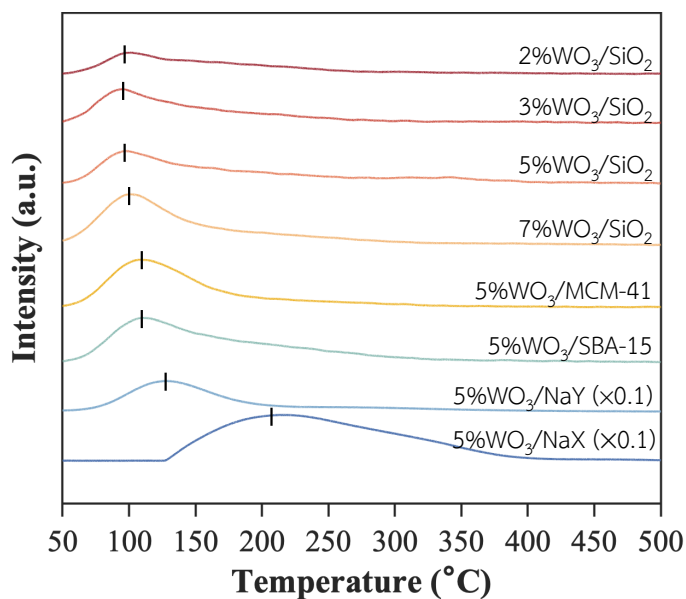


Figure B5 NH₃-TPD of WO₃ supported on various supports

B3. Thermogravimetric analysis of ethylene treated WO₃ supported zeolite catalysts

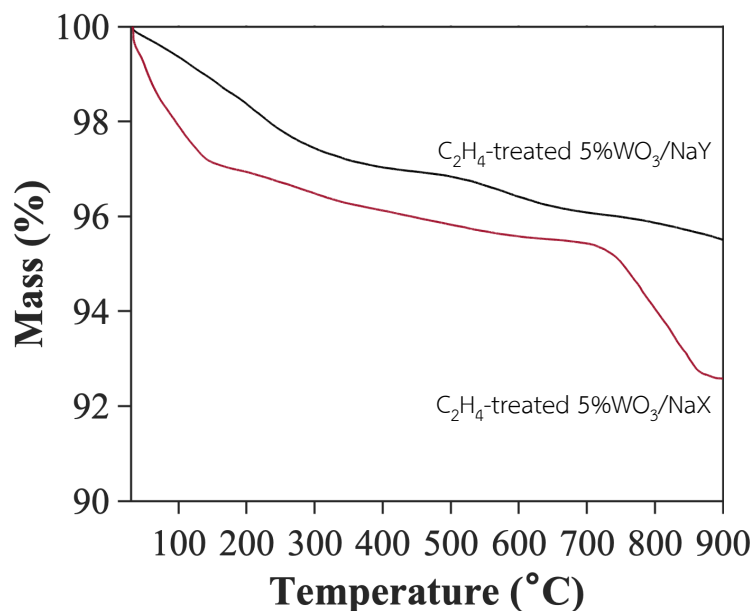


Figure B6 TGA curve of ethylene treated 5%WO₃/NaY, and 5%WO₃/NaX under air-zero (30 mL.min⁻¹)

B4. The reaction time profile of WO_3 supported confined siliceous supports

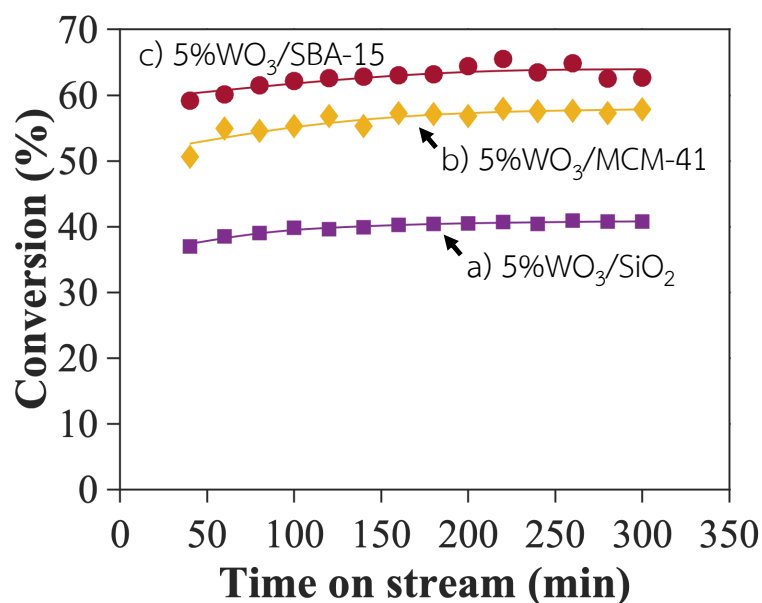


Figure B7 Acetylene removal with time on stream over a) 5% WO_3 /SiO₂, b) 5% WO_3 /MCM-41 and c) 5% WO_3 /SBA-15. (Feed flow rate 20 mL·min⁻¹ (acetylene/ethylene = 1/99 wt.%), N₂ flow rate 35 mL·min⁻¹, 450°C, activation in ethylene at 600°C for 2 h)

B5. The dispersion and coordination of WO_3 over siliceous support

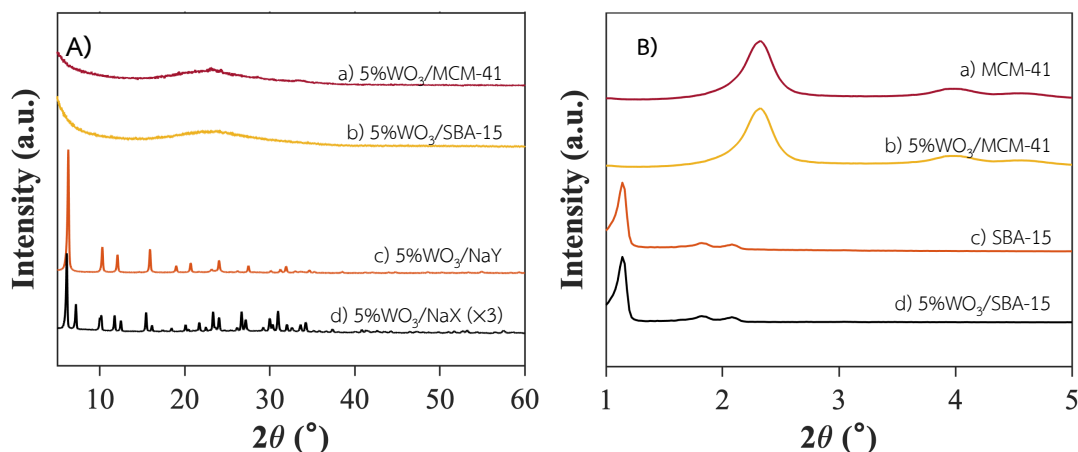


Figure B8 XRD diffraction patterns of WO_3 over confined supports a) wide angle and b) low angle

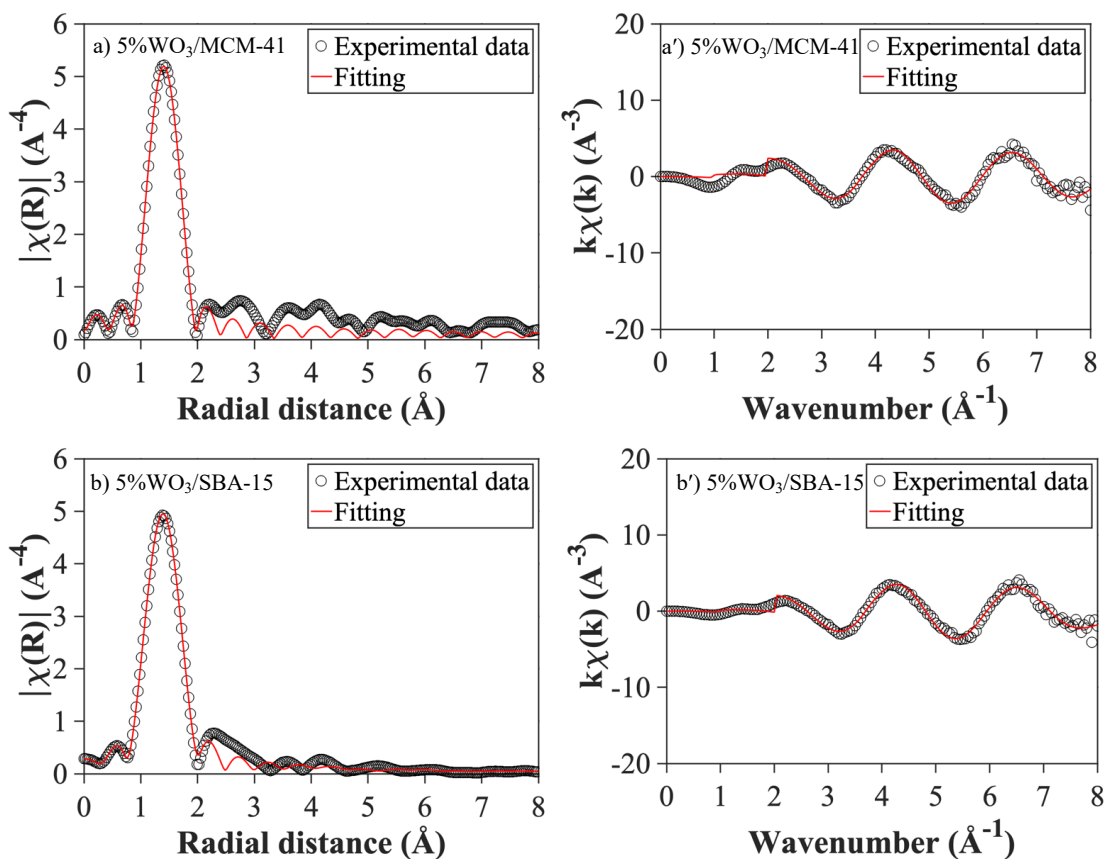


Figure B9 W L₃-edge *in-situ* TR-EXAFS Fitting of a, a') 5%WO₃/MCM-41 and b, b') 5%WO₃/SBA-15 at 500°C

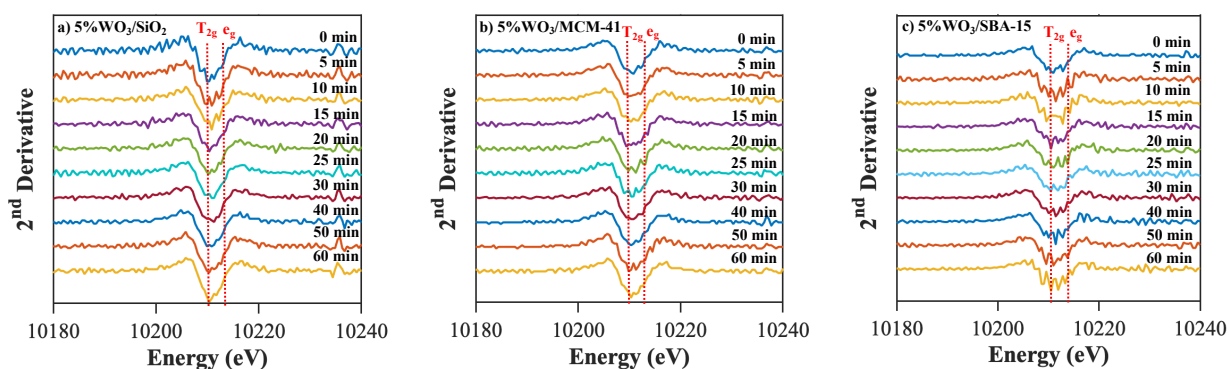


Figure B10 The 2nd derivative of W L₃-edge *in situ* TR-XANES spectra of a) 5%WO₃/SiO₂, b) 5%WO₃/MCM-41, and c) 5%WO₃/SBA-15 with 1-hexene activation at 600°C

B6. Thermogravimetric analysis of ethylene treated WO_3 supported confined siliceous catalysts

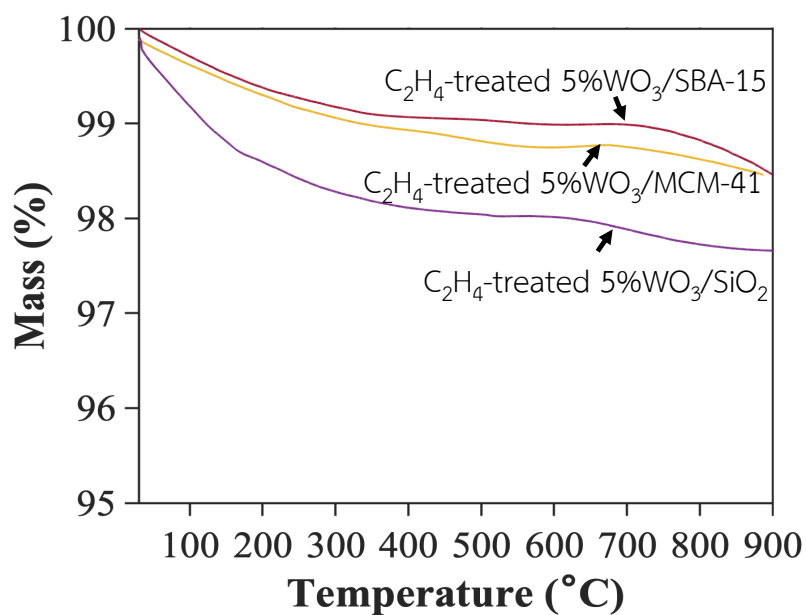


Figure B11 TGA curve of ethylene treated 5%WO₃/SiO₂, 5%WO₃/MCM-41 and 5%WO₃/SBA-15 under air-zero (30 mL·min⁻¹)

APPENDIX C

Calculations

C1. Conversion and yield

The conversion and yield of each product were calculated from GC peak area. It was corrected by response factor determining from area of a standard in which a known amount of product standard was divided by feed by this following equation.

$$\text{Response factor (RF)} = \frac{\text{Area of Product standard}}{\text{Area of Feed}}$$

Subsequently, the corrected area was normalized by response factor and used to calculate the conversion and yield.

$$\text{Corrected area (CR)} = \frac{\text{Area of Chemical A}}{\text{RF}}$$

$$\text{Conversion (\%)} = \frac{\text{Area of feed}_0 - \text{Area of feed}_t}{\text{Area of feed}_0} \times 100$$

$$\text{Yield (\%)} = \frac{\text{RF} \times \text{Area of product A}_t}{\text{Area of acetylene}_0} \times 100$$

$$\text{Selectivity (\%)} = \frac{\text{Yield of product A (\%)}}{\text{Conversion (\%)}} \times 100$$

$$\text{TOF (h}^{-1}\text{)} = \frac{\text{mol of converted feed}}{\text{mol of active site} \times \text{time (h)}}$$

$$\text{W/F (g.h.mol}^{-1}\text{)} = \frac{\text{catalyst weight (g)}}{\text{mol of feed/time (h)}}$$

Author Biography

Name Praty Promchana
Date of Birth 22 April 1991
Address 88/3 No.2 Huisai, Maerim, Chiang mai
Education (2016) Master of Science in Petrochemistry and Hydrocarbon,
King Mongkut's Institute of Technology Ladkrabang
(2014) Bachelor of Science in Chemistry (First honor),
Chiangmai Rajabhat University

Academic Publications

1. **Selective acetylene removal from ethylene-rich feed by cross-metathesis over supported WO_3 catalysts**, Praty Promchana, Kittisak Choojun, Wanwisa Limphirat, Yingyot Poo-arporn, Tawan Sooknoi, *Applied Catalysis A: General*, 2023, 650, 118972
2. **Experimental insights into catalytic oxidation of 1,6-hexanediol to ϵ -caprolactone over (*p*-cymene) $\text{RuCl}_2(\text{L})$ complexes in non-polar media**, Praty Promchana, Kittisak Choojun, Nararak Leesakul, Saowanit Saithong, Kittipong Chainok and Tawan Sooknoi, *Reaction Chemistry & Engineering*, 2022, 12, 2562-2572.
3. **Role of Surface Silanols and Confinements of Siliceous MFI Supports on Stability of Active Ga Species for Ethane Dehydrogenation**, Kittipong Prakobtham, Kittisak Choojun, Praty Promchana, Suchinda Sattayaporn, Tawan Sooknoi, *Applied Catalysis A: General*, 2022, 638, 118625.
4. **Higher alcohol production from ethanol over occluded $[\text{Mg}_4(\text{OH})_4]^{4+}$ clusters in MgO/KNaX** , Nattapol Yotkkham, Kittisak Choojun, Praty Promchana, Xiaolei Fan, Tawan Sooknoi, *Applied Catalysis A: General*, 2022, 632, 118502.

5. **Direct conversion of carboxylic acid to olefins over Pt-loaded, oxygen-deficient alkali hexatitanate catalysts with ketonization-hydrogenation-dehydration activity**, Pratyia Promchana, Adisak Boonchun, Jiraroj T-Thienprasert, Tawan Sooknoi, Tosapol Maluangnont, *Catalysis Today*, 2021, 375, 418–428.
6. **Effect of cobalt complex precursors on reactivity of cationic cobalt catalysts: Cyclohexane dehydrogenation**, Kittisak Choojun, Arucha Worathanaseth, Satu Kuhatasanadeekul, Teeraporn Kurato, Supanut Ketaniruj, Ploynisa Phichitsurathaworn, Pratyia Promchana, Kittipong Prakobtham, Natthida Numwong, Yingyot Poo-arporn, Tawan Sooknoi, *Catalysis Communications*, 2019, 125, 108-113.
7. **Local structure of stoichiometric and oxygen-deficient $A_2Ti_6O_{13}$ (A = Li, Na, and K) studied by X-ray absorption spectroscopy and first-principles calculations**, Jarin Kanchanawarin, Wanwisa Limphirat, Pratyia Promchana, Tawan Sooknoi, Tosapol Maluangnont, Kodchakorn Simalaotao, Adisak Boonchun, Pakpoom Reunchan, Sukit Limpijumngong, and Jiraroj T-Thienprasert, *Journal of Applied Physics* 124 (2018) 155101.